INSTITUT DE SCIENCE ET D'INGÉNIERIE SUPRAMOLÉCULAIRE

UNIVERSITÉ LOUIS PASTEUR

THÈSE DE DOCTORAT

« SELF-ASSEMBLY OF FUNCTIONAL MOLECULES AT SURFACES »

Présentée par : *GIUSEPPINA PACE*

Unité de Recherche : *UMR N° 7006 Nanochemistry Laboratory (ISIS-ULP)*

Directeur de Thèse : *Professeur SAMORÍ PAOLO*

Table of content

Chapter 5: MIXED SELF-ASSEMBLED MONOLAYERS

Chapter 6: ADSORPTION OF MOLECULAR GRID S ON HOPG SUBSTRATE

Abstract

This work is aimed at establishing a correlation between molecule-substrate and molecule-molecule interactions in view of the future implementation of nano-electronic devices based on unctional molecules.

In particular, we studied the self-assembly behaviour of organic thiols functionalized molecules holding potential to act as switches on solid substrates. We focused on the isomerization of azobenzene based Self-Assembled Monolayers (SAMs) on gold substrates. A fine tuning of interchain interactions within the SAM made it possible to obtain high yield of isomerization.

We also devised a new method to isolate individual functional molecules in a host SAM. In the final chapter we present our studies on the self-assembly properties of grid-like supramolecular architectures.

Sub-molecularly resolved Scanning Tunneling Microscopy studies offered direct insights into structural and dynamic properties of the monolayers.

CHAPTER 1

INTRODUCTION TO THE THESIS

1.1 Molecular electronics

Nowadays electronic devices are developed making use of "conventional" inorganic semiconductors. These semiconductor-based devices are built exploiting the "top-down approach", [i] but when reaching the nanometer-scale the lithographic and etching methodologies used to pattern a substrate becomes more challenging. Presently we are reaching the limit of this miniaturization dictated by both physics laws and the production costs. This limit can be overcome by taking advantage of the wide opportunities offered by molecular electronics [ii]. Pioneers in the field of molecular electronics are Aviram and Ratner[1] who first proposed donor-acceptor (D-σ-A) molecules as unimolecular rectifiers i.e., molecular based *p-n* junctions.

Benefiting from the development in molecular engineering of organic molecules, various electroactive systems can be designed to generate specific functions. Such versatility,

[i] Two main approaches are used in nanotechnology: one is a "bottom-up" approach where materials and devices are built from molecular components which assemble using principles of molecular recognition; the other being a "top-down" approach large entities are downscaled using nanofabrication tools which unfortunately do not offer a control down to the atomic level. Importantly, nanotechnology encompasses many disciplines, including colloidal science, chemistry, applied physics, materials science, and even mechanical and electrical engineering.

[ii] The first distinguishing concepts in nanotechnology was in "There's Plenty of Room at the Bottom," a talk given by physicist Richard Feynman at an American Physical Society meeting at Caltech on December 29, 1959. In the course of this, he noted, scaling issues would arise from the changing magnitude of various physical phenomena: gravity would become less important, surface tension and Van der Waals attraction would become more important, etc.

together with the molecular scale size, is the major advantage of molecular electronics which relies on the "bottom-up" approach to build devices from single atoms building blocks with a very high accuracy.

As already mentioned, improvements in computer science require the reduction of the circuit feature size and the increase of the integration density of the actual semiconductor based electronics. However, presently the electronic principles exploited in operating devices are based on the bulk properties of semiconductors and, when reaching dimensions comparable to the exciton Bohr radius, quantum mechanical effects come into play. This leads to sensible variation in the principles governing the electronic processes which brings to severe changes in the device behaviour. Since the shrinking of the device's size implies to take into account the quantum phenomena then, it is not surprising if molecules are proposed as well defined quantum systems to be implemented in future electronic devices. The beauty of molecules relies in the chance they offer to span above different tuneable optical, electronic and magnetic properties.

A molecule suitable for data storage should posses the following properties:

1- *multi-stability*. The molecular system should be able to convert between two or more physicochemical distinct states; such state have to be completely controlled by external trigger, e.g. an electromagnetic field; therefore the lifetime of each state should be has long as possible to render the switching possible only by the external input, i.e. thermodinamic relaxation between the different states at room temperature should be accompanied by a high activation barrier making possible to convert the system on by the external stimuli, i.e. activation energy;

2- *chemical stability*. This is required to extend the processability of the system in different environement and to promote the use of different techniques;

3- *addressability to the nanoscale regime*. As the interest in molecular electronics is dictated by the new possibility to shrink to the nanoscale the currently commercialized electronic devices, it is of paramount importance to be able to address and characterize the single switching molecule. Therefore, new techniques need to be developed to characterize these systems down to the nanoscale. Recent progress in nanotechnology and nanoscience has facilitated both experimental and theoretical study of molecular electronics. In particular,

the development of the Scanning Tunneling Microscope (STM) and later the atomic force microscope (AFM) has facilitated manipulation of single-molecule and the detection of its electronic properties.

Very interesting operational molecules for future application in molecular electronics have been synthesized and thoroughly characterized in solution. Because of their capability to act at the molecular scale as machines those molecules are defined as molecular switches and molecular motors. Examples include rotors[2-4] (see an example in Fig. 1.1), nanocars and nanowalkers,[5-7] various kinds of electrical switches and leads, and ratchets.

A *molecular switch* can be defined as a molecule able to be activated and deactivated by physical or chemical external stimuli, e.g. reversible ion coordination, light absorption, pH variation, voltage application etc...[8] Different external stimuli may determine in a controlled fashion the molecule switching. These include: application of electric or magnetic field, ion complexation, pH variation, light induced isomerization, light induced photochromism. A wide number of molecules possessing good switching properties in solution have been reported in the literature.[9-11]

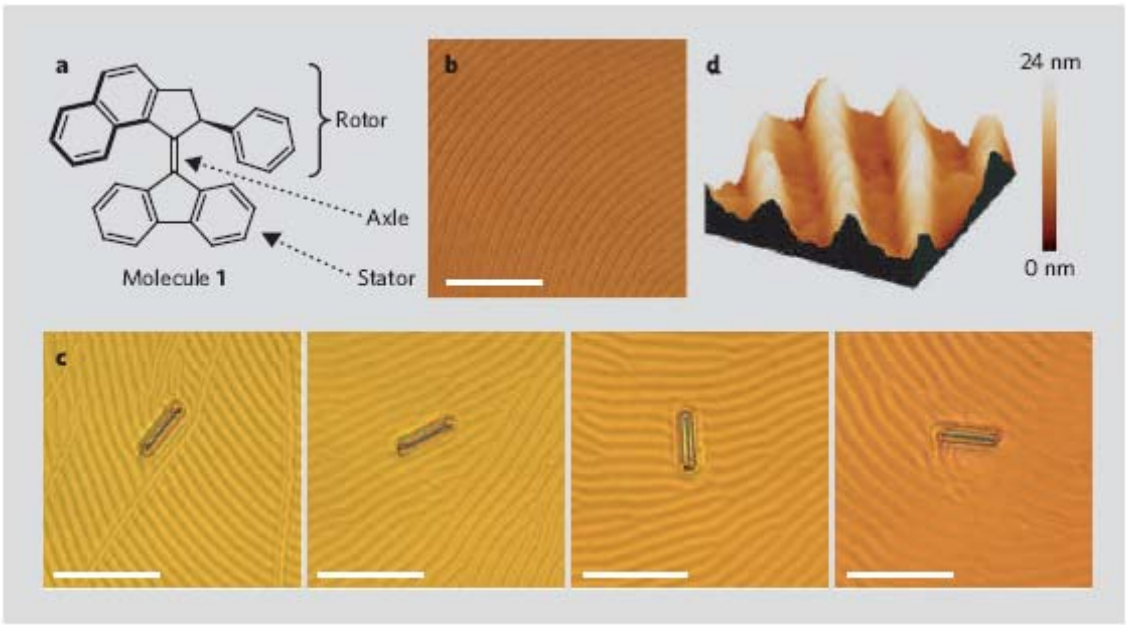

Figure 1.1: Features of a light-driven motion induced by a molecular motor (Molecule1, bonds in bold point out of the page). **b-** Polygonal texture of a liquid-crystal film doped with molecule 1. **c-** Glass rod rotating on the liquid crystal during irradiation with ultraviolet light (scale bar 50μm).**d-** AFM image showing the surface structure of the liquid-crystal film (scale bar 15μm^2).[12]

1.1.2 Current research in Molecular Electronics and motivation of this thesis work

Unfortunately, in spite of the great number of switching molecules fully characterized in solution, only a few of them have been found to keep their interesting solutions properties once integrated in electronic circuit.[13, 14] The binding and the electrical connection of those functional molecules remains a major problem to solve before the full exploitation of such molecular systems in electronics. Different approaches have been developed to characterize the electronic behaviour of switching and motor molecules when they are bridging between electrodes separated by nanogaps (Fig. 1.2).[15-17] This include: break junctions[18, 19], conductive AFM and STM,[20-22] nanopores,[23] nanobeads.[16, 23-27]. Given the difficult understanding of the electrical characteristics of nanoscale molecular junctions, the development of theoretical methods to describe the electron transport properties are truly important. Therefore, challenges in the field include device optimization and the thorough theoretical description.

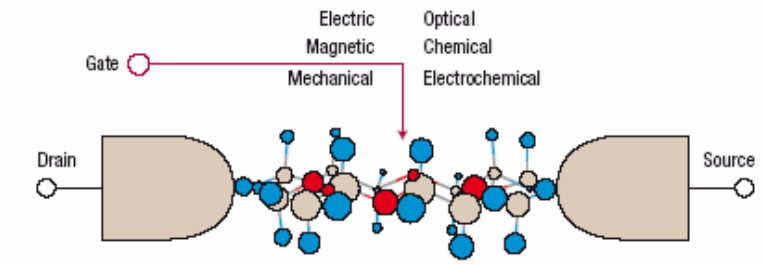

Figure 1.2: Ideal configuration of a molecular junction. The molecule is connected with two electrodes. Electron transport through the molecule may be controlled by external electrical, magnetic, optical, mechanical, chemical or electrochemical stimulus, leading to various potential device applications.[16]

Alongside, it is also important to develop methodologies able to "write" and "read" those functional molecules in their different states and at the nanoscale dimension. One of the recent improvements in the field of molecular electronics is the development of the organic integrated circuits which includes complementary metal oxide semiconductor (CMOS) field effect transistors[13, 28], organic field effect transistor (OFET)[29, 30] and organic cross junction[22, 31]. The latter consists of nanowire crossbar arrays that sandwich assemblies of functional molecules. These devices combine the top-down approach for scaling up to a few

tens of nanometers the size of the top and down electrodes, with the bottom-up design of assemblies of switching molecules that can fully operate in the device configuration.

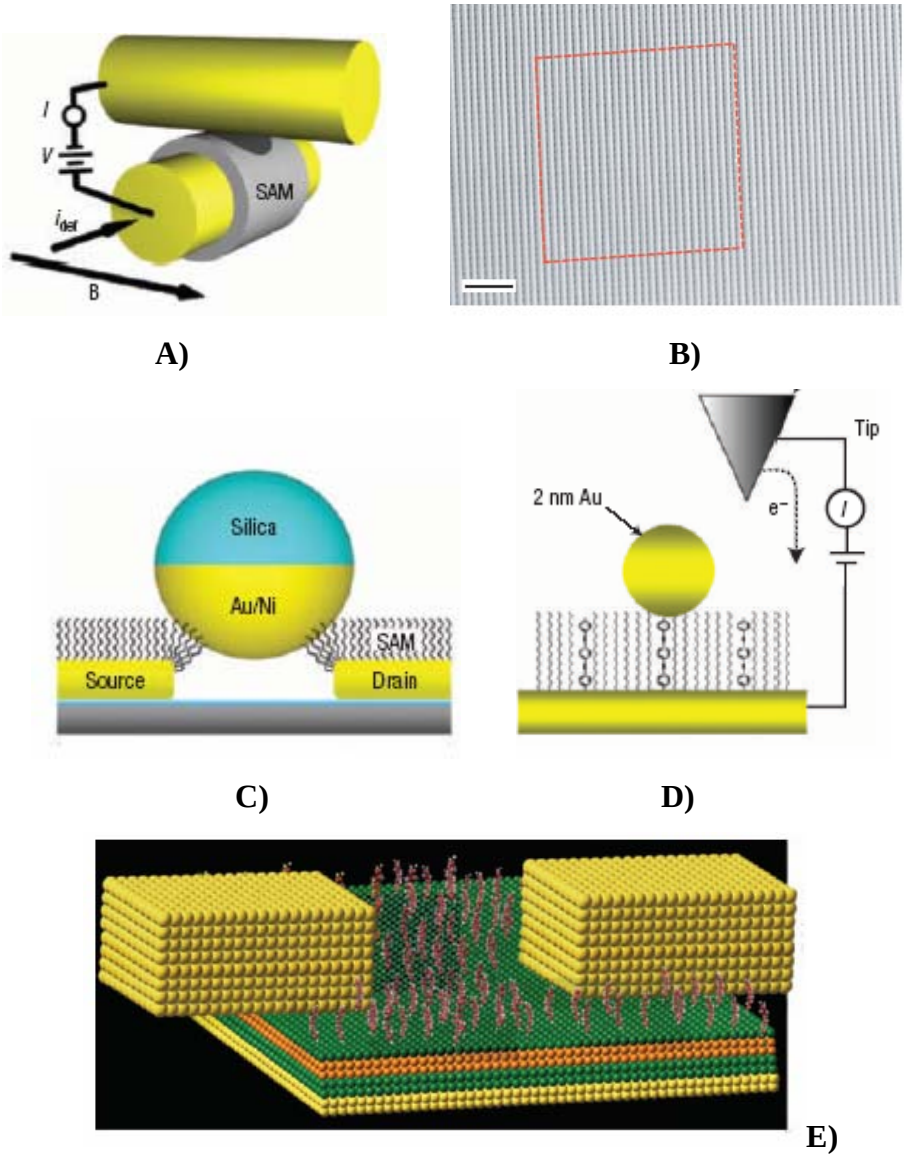

A) **B)** **C)** **D)** **E)**

Figure 1.3: A) Schematic representation of a crossed-wire tunneling junction.[16] **B)** Scanning Electron Microscopy micrograph of a nanowire crossbar memory operating device built by Heath and coworkers. In their work the authors present a 160-kbit molecular electronic pattern based on SAMs formed by a bistable rotaxane.[13, 32] **C)** Schematic illustration of a magnetic bead junction. **D)** Schematic drawing of a metal bead junction. **E)** Representation of an organic thin-film field effect transistor (OFET).[33]

One of the major challenges in molecular electronics is to preserve the well defined solution switching properties of those molecules also when they are adsorbed on solid substrates either as single molecules or assembled in ordered arrays on the solid surface. In fact, the new packing environment defined in the solid device might introduce some important constrains that hinder the switching behavior.

At a first glance on the molecular-device set-up schematized in Fig. 1.3, it clearly appears that the prime strategy employed to bind switching molecules between two electrodes is the formation of Self-Assembled Monolayers (SAMs). Indeed, SAMs of organothiols on gold substrate are well known for their long time stability under inert conditions, for their high reproducibility and long range bi-dimensional order (up to several tens of nanometers).[34, 35]

This evidence justifies the choice to focus our attention on molecular switches that are able to form ordered assemblies chemisorbed on gold substrate. Despite the many advantages offered by SAMs of thiols derivatives chemisorbed on gold, it is important to retain the peculiar switching function in the new assembly environment. A careful design of those molecules at the supramolecular level is required, which implies the fine optimization of the molecule-substrate and molecule-molecule interactions. The latter includes both nearest neighbor interaction and sterical hindrance that might generate before and after switching process.

In view of the above, we carried out a thorough study of a new azobenzene derivative which has been tailored to preserve its isomerization properties when forming SAMs on gold substrate (see Chapter 4). Interestingly we found that cooperative processes dictated by the rigid nature of the molecules forming tightly packed 2D crystalline assemblies might induce high yields of isomerization also in the molecular assembly at solid substrate. These molecules are therefore ideal candidate to be employed as multi-stable organic layer in a cross wired junctions.

Besides the implementation of mono-component SAMs of switching molecules in cross wired junctions, it is also interesting to study the switching properties of single molecules to further shrink the feature size of electronic devices.

In order to achieve the spatial confinement of a single switching molecule on a solid substrate, many previous works were based on the study of switching molecules embedded mainly at defects sites of a guest SAMs matrix (Fig. 1.4)[36]. Even if this approach brought to some interesting results, we believe that it is not possible to reach a full control above the

switching properties.[26, 37-40] In fact, molecules bound at defects sites can easily diffuse, rearrange they conformation, desorb and readsob at different binding sites. It is therefore difficult to unambiguously attribute the detected switching behavior to the intrinsic nature of the molecules rather than to artifacts originated from those phenomena. In view of the above, we decided to develop new strategies based on the generation of multi-component SAMs where the functional molecules can form an ordered array of spatially distributed molecular functionality (see chapter 5).

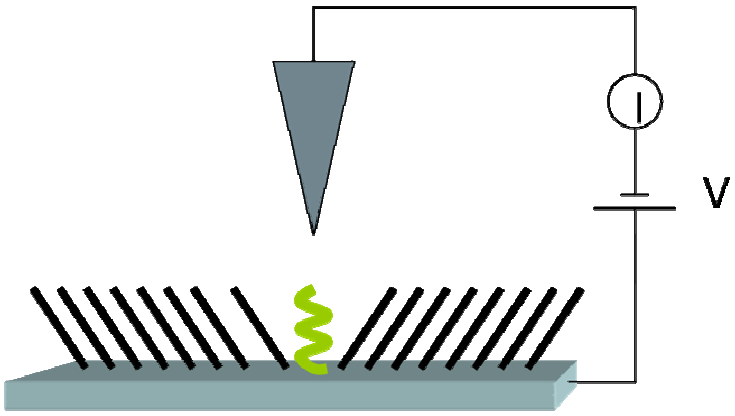

Figure 1.4: Schematic representation of a switching molecule embedded at a defect site of a guest SAM matrix detected electronically by a conductive AFM-tip or a STM-tip.

Complex functional architectures like crossed wired array of "ion bits" can also be developed from the bottom-up approach, taking advantage of the highest level of sophistication that can be achieved by supramolecular chemistry. Thanks to their intrinsic ability to position metal ions in regular network, grid-type supramolecular transition metal assembly can mimic binary coded matrix and crossbar architectures which are typically employed in conventional information storage and processing technology.[41] These systems own the unique property to not require the expensive micro- or nano-fabrication of the bit unit as the spontaneous supramolecular assembly is performing the "job".

A metal ion coordinated by non-covalent bonds can be considered as an "ion quantum dot". In solid physics a quantum dot is defined as a crystal, mainly based on semiconductor compound (e.g. CdSe, PbS), with a diameter on the order of the compound's Exciton Bohr Radius. This reduced size, typically on the order of 2-10 nanometers, infers to the system quantitized electrical and optical properties which differ from those of the bulk material. A [*n*x*n*] metal grid contains n^2 "ion dots", while the inorganic quantum dots define a dots

formed by 10-50 atoms. Furthermore the ligand represents a natural spacer between the "ion dots" that results in their spatial controlled confinement also in ambient conditions. The electronic and optical properties of an inorganic quantum dot are driven mainly from their size and geometry. By tailoring the geometrical arrangement of the ligands and varying the metal ion and/or specific functionality on the organic ligand, those properties can be finely tuned by the synthetic chemist much easily than in the case of inorganic quantum dots. Therefore, the versatile design of metal supramolecular complexes foster the development of novel kind of multistate digital information storage and processing. From solution studies interesting switching properties of those compounds have been already detected.[42] A preliminary study on grid-type supramolecular architectures is presented in Chapter 6.

A first step toward the exploitation of the intrinsic properties of switching molecules is represented by the possibility to address them individually. Some of those properties have been characterized by the nano-junction approaches where one functional molecule was placed in between two electrodes (see above in the paragraph). However those techniques suffer from the drawback of a restricted access to local structural information, although such properties intimately relate to the assembly feature of these molecules on solid substrate. From this point of view Scanning tunneling microscopy (STM) is a useful and unique tool which combine the nanoscale investigation of the electrical and structural properties of these systems. STM can be considered a local probe able to "read" and "write", on the atomic scale, the information stored at the molecule site and/or group.

1.2 Self-Assembled Monolayers (SAMs)

The spontaneous self-assembly of surfactants on solid substrates has been the subject of many research studies in surface science. This field has grown rapidly since the discovery of the possibility to modify chemical and physical properties of surfaces through the self-assembled system. These studies span from the basic understanding of the assembly mechanisms to their application especially in molecular sensors and molecular electronics. Different techniques have been developed to form assembly of functional molecules on surfaces (drop casting, spin coating, chemical evaporation and spray deposition to indicate to name a few). Ordered assembly in ambient condition can be obtained by the spontaneous organization of amphiphilic molecules at a variety of interfaces (liquid-liquid, air-liquid, solid-liquid and solid-air). One of the most useful techniques employed to assemble

amphiphilic molecules is the Langmuir-Blodgett technique (LB), in which surfactants are organized at the air water interface. Once the amphiphilic molecules reach a compact assembly on the water surface, the as formed monolayer is transferred to a solid substrate. The LB films suffers both from chemical and mechanical stability therefore more structurally stable films have been developed by choosing head functional group able to specifically interact with the target solid substrate and by designing molecular backbone which can promote a dense packing through strong intermolecular interactions. Therefore, in view of a practical application chemisorbed systems are more attractive, in view of their greater stability.

Different molecule-substrate chemical interactions have been explored to foster the binding of molecules on the substrate. This particular kind of film has been defined as Self-Assembled Monolayers (SAMs) which mainly identify molecular ordered patterning on solid substrates featuring a strong affinity between a specific molecular group and the substrate. The high degree of lateral order within the SAMs is achieved by stable lateral intermolecular interactions like van der Waals interactions between alkyl chains. The strength and the stability of these films hold on the molecule-substrate interactions as well as on the intermolecular interactions.

Different types of strong molecule-substrate interactions have been exploited,[34, 43, 44] including covalent and strong electrostatic interactions as in the case of:

- carboxylic acids adsorbed on metal oxides (AlO, AgO, CuO, Al_2O_3) and semicondutors;
- alkanethiol on Cu, Pt, Pd, Hg, Ag, Au;
- trialkyl-, trichloro- or trialkoxysilanes on hydroxylated surfaces like: silicon oxides, aluminum oxides, quartz, glass, mica, zinc selenide (ZnSe), germanium oxide.

Well characterized systems are those formed from thiols derivatives chemisorbed on transition metal surfaces, like Ag and Au. SAMs formed on Ag surfaces are more tightly packed than those formed on gold, thus the alkyl chain are less tilted with respect to the surface normal. The gold substrate is mostly inert to oxidation therefore SAMs can be easily prepared in ambient conditions. The formation of a SAM creates an insulating barrier reducing or avoiding diffusion of impurity through the surface.

The versatility offered by synthetic chemistry allows addition of functional groups at different positions along the molecular backbone. In particular replacement of the terminal functional group may be used to tailor the surface different chemical and physical properties,

e.g. a methyl group replaced by a hydroxyl group can vary the surface properties from hydrophobic to hydrophilic. Variation of the chemical group responsible for the binding to the substrate controls the strength of the interactions, therefore the stability of the assembly. The molecular structure as well as the chemical contact with the substrate has been found to play a fundamental role in the control of the conductive properties in a molecule/metal or molecule/semiconductor junction.[17]

SAMs have been characterized by different techniques providing coherent and complementary information. This includes the SAMs structure characterizations of SAMs with spectroscopic techniques like X-ray Photoelectron and Diffraction Spectroscopy (XPS and XDS), Ellipsometry, Fourier Transform Infrared Spectroscopy (FTIR); imaging techniques as Scanning Probe Microscopy (Scanning Force Microscopy, SFM, and Scanning Tunneling Microscopy, STM); electrochemistry; contact angle goniometry, etc... Among them STM has the advantage of providing direct an sub-molecularly resolved evidence of the molecular packing on surfaces.

At room temperature a dense monolayer can be formed if the interchain interactions, like van der Waals interactions are optimized to favor a parallel stack of the molecular backbone, where all the chains are in the *trans*-conformation. For *n*-alkanethiols a dense packing is achieved if $n \geq 10$. The film structural properties are determined by the solution concentration, solvent, chain length, temperature, immersion time in the incubating solution, and thermal treatment done during or after the substrate incubation.[45-50]

The forces involved in the determination of the alkanethiols SAMs can be summarized as follows: binding group substrates interactions namely the Au-S interaction; dispersion forces between alkyl chains; chain end-group interactions. The structure of a SAMs is a delicate balance of all these interactions.

The exposure of the gold substrate to a thiols solution, even for a few seconds, brings to the formation of a gold-sulfur bond. The assembly process continues with the organization of close packed molecular structure on the gold substrate, achieved by diffusion and conformational reorganization of the molecular backbone. The crystalline structure of the organic monolayer is slightly different from the well characterized bulk crystalline structure. The strong interaction with the gold substrate is responsible for such a difference.

The strong Au-S bond is defined as a highly polarized covalent bond, where the negative charge is mainly located on the S atom (25% of the negative charge of the Au-S

bond) giving to the bond a polar character ($X(CH_2)S^-—Au^+$). The bond energy is calculated to be 184 kJ/mol, and in their work Scoles and co-workers measured a chemisorption energy of 148kJ/mol.[51-53]

Ab-initio calculations showed that the more stable S-Au binding site is the interstitial sites of the Au(111) surface where the sulfur is coordinated with three gold atoms. The energy difference between the interstitial adsorption sites (three-fold-hollow sites) and the top-atom absorption sites has been calculated to be ~25 kJ/mol, i.e. one order of magnitude higher than the thermal energy at 298K.[34]

However, recent studies demonstrated that it is also possible to adsorb the *n*-alkanethiols on top-atom sites. An interesting work has been published recently by Dhanak and co-workers who state that the actual monolayer structure is determined by a strong reconstruction of the gold surface.[54] According to their experimental evidence the authors propose a new structure where the gold atoms are expelled from the gold surface and form a new upper-gold atoms layer where each atom is sited at three-fold hollow sites of the underlying Au(111) surface. The thiolated molecules are bound on top of each gold atom of this upper-gold atoms layer.

Diffraction studies and STM studies showed a long range order of the molecular domain ($\approx 10^2$-10^3 Å wide). The 2D crystalline domains borders represent defects sites in the overall assembly (Fig. 1.5). Domain boundaries form either because of the mismatch of binding site registry or/and different chain tilting or rotation. In Fig. 1.5 and Fig. 1.6 a schematic interpretation of these defects is reported.

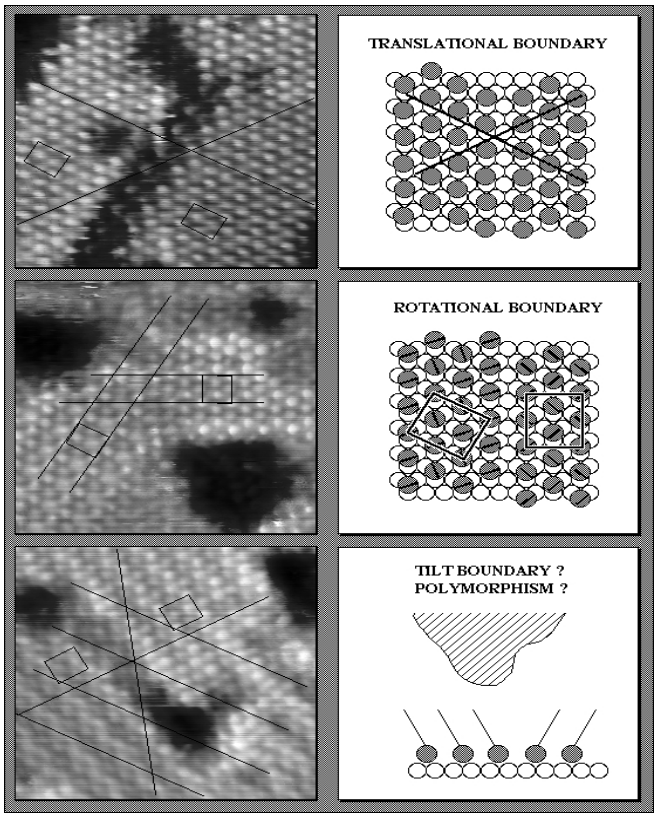

Fig. 1.5: STM image of SAM of octanethiol on Au(111) (60x60 $Å^2$)**.** Per each image representing a domain border defect a schematic interpretation of the nature of this defect picture is reported on the right. A three-fold binding site has been chosen to anchor the molecules (gray circles) to the Au(111) (white circles). The diagonal segments in the gray circles indicate the all *trans* alkyl chain projection on the gold substrate. (http://www.cstl.nist.gov/div836/836.04/SAMS/structure.htm)

When imaged with local probes SAMs reveal a typical pattern with "holes". Such holes are monoatomic deep gold vacancies having a width of a few nanometers and depth of ~0.24nm. These holes originate from the strong reconstruction induced by the thiols binding on the gold surface. As the assembly involve a dynamic exchange between molecule in solution and on the substrate and in view of the founding of dispersed gold in the incubating solution it is thought that such dynamic equilibrium determines the desorption of the gold from the substrate originating therefore the formation of the gold vacancies clusters.[55] Upon adsorption and chemisorption of the thiols interatomic interactions among Au atoms on the surface are weakened. The reduced surface binding strength allows the gold atoms to diffuse, reorganize and also desorb. About 2 Au atoms per unit cell are released and the gold

vacancies coalesce into islands. Defects are also represented by step edges originated by the presence of gold terraces, molecular domains boundaries, molecular conformational disorder and molecular vacancies in the 2D molecular crystal (Fig.6).

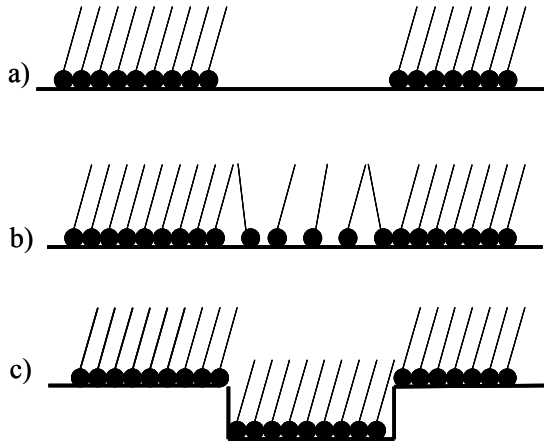

Figure 1.6: Schematic representation of defects in a SAM: **a)** Molecular vacancies ("Pin-holes"); **b)** Conformational defects of molecules in the SAM; **c)** Cluster of gold vacancies of monatomic depth ("Pits o Holes").

In Fig. 7 is also shown the typical $(\sqrt{3} \times \sqrt{3})R30°$ hexagonal packing of the alkanethiols. Alkanethiols on Au(111) usually form a typical $(\sqrt{3}\times\sqrt{3})R30°$ structure, these lattice parameter define a commensurate unit cell with respect the underlying gold .

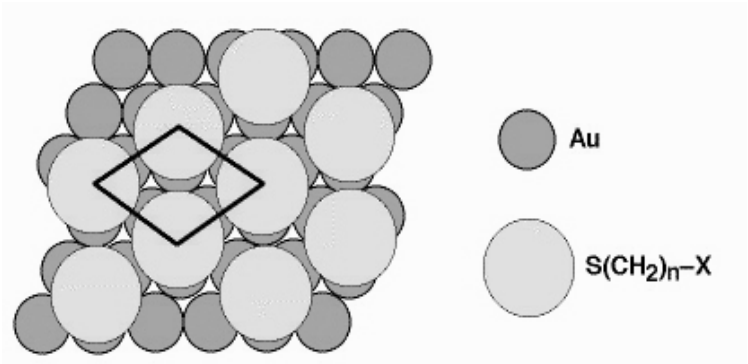

Figure 1.7: $(\sqrt{3}\times\sqrt{3})R30°$ structure of the bidimensional lattice of an alkanethiol SAM on Au(111) substrate. The binding sites are the three-fold hollow sites.

The unit cell definition derives from the unit cell parameters of the gold surface, the alkanethiol unit cell real parameters are therefore $(2.89\sqrt{3} \times 2.89\sqrt{3})R30°$ where the value 30° indicate the mismatch of the molecular direction growth with respect to the surface lattice

directions growth. The distance between sulphur Au-S binding sites is therefore 4.99Å. In a densely packed monolayer alkyl chain adopt an all *trans* conformation and the molecular axis are tilted at ca. 30° with respect to the substrate plane.

Thermal treatments performed during or after the assembly formation favour the healing of defects in the SAM. After annealing bigger molecular domains are found and the gold vacancies coalesce or diffuse at terrace borders and disappear reducing their total density on the surface. Also conformational rearrangements of the molecular backbone in induced by the thermal annealing, improving the settlements of lateral interactions. The thermal annealing of decanthiol in neat ethanol decreases the defects density, while simultaneously induces the desorption of weakly bound *n*-decanthiolates.[56]

1. SAM formation: a many steps process

During the assembly process many equilibrium processes between molecules bound at the surface and in solution are kinetically limited. While *n*-alkanethiolates SAMs are stable surface structures, the adsorption process is highly dynamic and molecules can continue to exchange with other thiol species in solution or in the vapour phase, with many exchange events occurring especially at structural defects sites. An important factor to be considered is that molecules in solution are solvated, therefore enthalpy and entropy of solvation can limit the dynamic of adsorption. The growth process of a SAM is complex and follows different steps.[46]

It has been possible to distinguish four steps bringing to the formation of a SAM.

Ist Step: molecules are free to diffuse above the gold substrate and weakly interacting with it. At this stage molecules are highly mobile and are not possible to get molecular resolution on this diffusive state (liquid-like state).

IInd Step: nucleation of small islands of molecules oriented with their main axis parallel to the surface plane. This is a first condensation state. UHV-STM measurements showed the formation of a bi-dimensional crystal defined as the striped phase (Fig. 1.8 and Fig. 1.9).[57-59]

The period between the stripes has the same width as twice the length of the single molecular extended chain. In this phase molecules are only physisorbed to the substrate and this phase is also referred as the bi-dimensional liquid phase. The low surface coverage of the striped phase is typical for short time incubation in low concentrated thiol solutions.

Islands of gold vacancies also form during this stage; these appear as mono-atomic deep holes in the gold surface. The stripes phase has also been observed in SAMs evaporated in vacuum conditions or after a thermal annealing bringing to the low desorption of molecule from the more dense c(4√3×2√3)R30° structure. The periodicity of the stripes phase can be described as a function of the Au(111) lattice parameter as a px√3 periodic structure where p, the stripes period is a linear function of the alkyl chain length (Fig. 1.8). A value of p=1.9 it is usually found for those stripes phases.

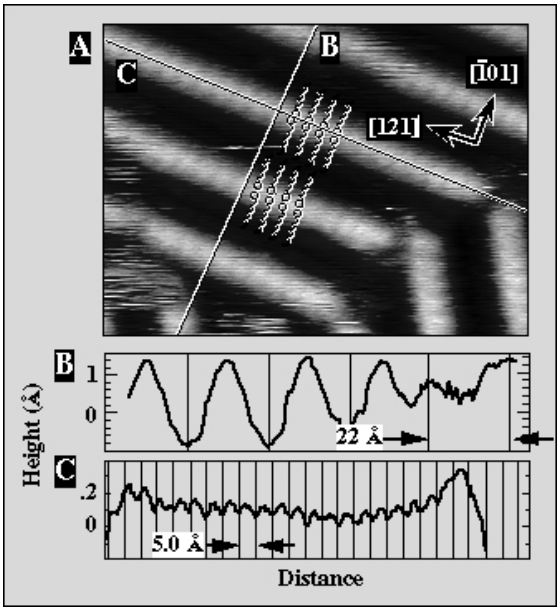

Figure 1.8: Constant current mode STM image of the stripes phase formed by mercaptohexanol evaporated on Au(111) (A). (B), (C) are the line profiles. The period is consistent with a head to head and, tail to tail arrangement of the molecules as depicted in (A). (http://www.cstl.nist.gov/div836/836.04/SAMS/structure.htm)

The cooperative nature of the stripes phase formation explains the observed deviation from a simple Langmuir kinetic observed during the solution growth.

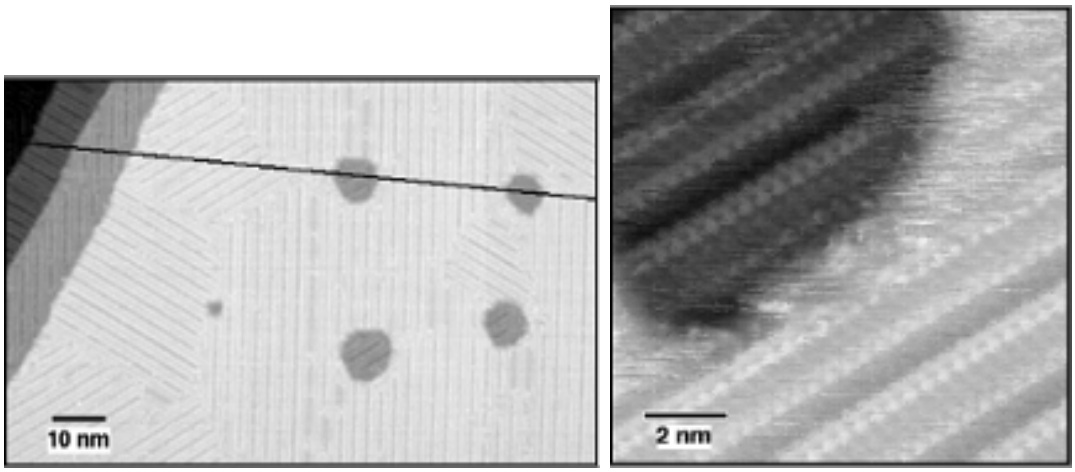

A) **B)**

Figure 1.9: STM image of the low density phase (striped phase) formed by the butanethiol self-assembled on gold. The holes depth is equivalent to the monoatomic terrace height. B) High resolution image showing that an ordered assembly is also formed in the holes. (http://www.cstl.nist.gov/div836/836.04/SAMS/structure.htm)

IIIrd step: The striped phase is quickly replaced by the more dense ($\sqrt{3}\times\sqrt{3}$)R30° structure, where the molecular axis are at 30° from the surface normal. By means of STM imaging it has been observed that for n=10 the nucleation of the new phase starts when the stripes phase cover the 70% of the surface. It is possible that a critical surface concentration defines the beginning of the nucleation of the high density phase. The ($\sqrt{3}\times\sqrt{3}$)R30° structure is typical of SAMs formed by incubating the gold surface in high concentrated solutions.

IV^{rt} step: self-healing of the monolayer defects including: back-filling of molecular vacancies, rearrangement of the chain conformation to improve the lateral packing; reduction of domain boundaries through the enlargement and coalescence of domains. The chain conformational reorganization to form an all-*trans* alkyl backbone is an important process especially for long alkyl chain as for SAMs of C_{22}. The annealing of the *gauche* defects might be the rate determining step in those SAMs (it can be up to 100-300 times longer than the initial molecular absorption).[60]

The different growth phases of a mercaptohexanol SAMs are showed by the UHV-STM images reported in Fig. 1.10.

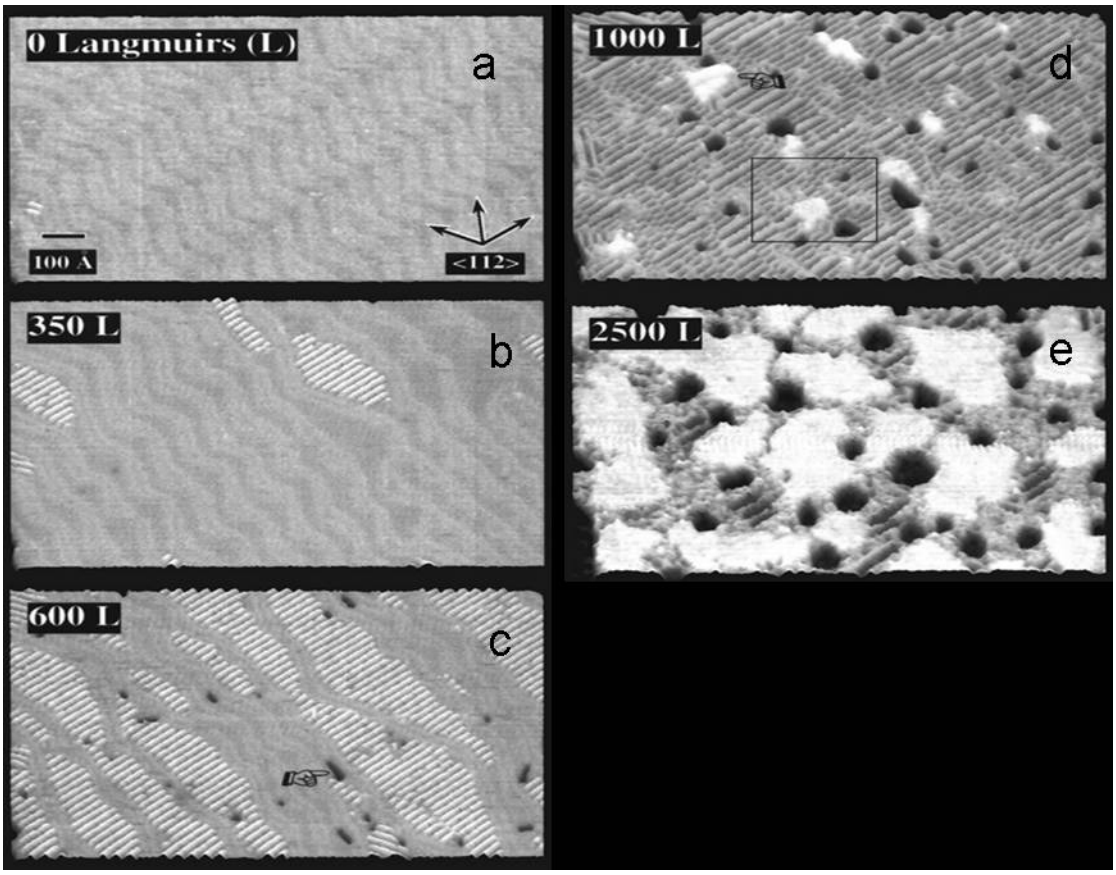

Figure 1.10: Constant Current STM showing the time evolution of the reconstructed Au(111) **(a)** upon the phase evaporation of mercaptohexanol. **(b)-(c)** Nucleation and growth of the stripes phase. The complexity of the surface forces playing role in this growth process is evident from its strong reorganization upon molecular absorption. **(c)** Higher thiols surface concentration brings to the nucleation and growth of holes. **(d)-(e)** the higher density phase nucleates and grow. In each picture is reported the amount of molecules evaporated in terms of Langmuir monolayers.[61]

During the SAMs relaxation superstructures of the ($\sqrt{3}\times\sqrt{3}$)R30°lattice have also been observed. These superstructures have been interpreted in term of a variation of the alkyl chain orientation, or as derived from the formation of disulfides or originated from different adsorption sites.

The typical superstructure so far reported is the c(4×2) (or c($4\sqrt{3}\times2\sqrt{3}$)R30°). The unit cell contain four molecules, the one placed at the unit cell corner are arranged with a conformation different from the one's sitting inside the unit cell. Molecules at the unit cell

corners extend the alkyl chain outside the monolayer through a vibrational mode of twisting, therefore appearing as brighter in STM images.

The formation of a superlattice reconstruction the c(4√3×2√3)R30°, and of mono-atomic deep holes, the presence of the striped phase, all those factors show that the processes involved in the SAMs formation are rather complex.

References

[1] A. Aviram, M. A. Ratner, *Chem. Phys. Lett.* **1974**, *29*, 277.

[2] B. L. Feringa, R. A. van Delden, N. Koumura, E. M. Geertsema, *Chemical Reviews* **2000**, *100*, 1789.

[3] J. J. D. de Jong, L. N. Lucas, R. M. Kellogg, J. H. van Esch, B. L. Feringa, *Science* **2004**, *304*, 278.

[4] G. S. Kottas, L. I. Clarke, D. Horinek, J. Michl, *Chemical Reviews* **2005**, *105*, 1281.

[5] R. Otero, F. Hummelink, F. Sato, S. B. Legoas, P. Thostrup, E. Laegsgaard, I. Stensgaard, D. S. Galvao, F. Besenbacher, *Nature Materials* **2004**, *3*, 779.

[6] F. Chiaravalloti, L. Gross, K.-H. Rieder, S. M. Stojkovic, A. Gourdon, C. Joachim, F. Moresco, *Nature* **2007**, *6*, 30.

[7] J. K. Gimzewski, C. Joachim, *Science* **1999**, *283*.

[8] A. Troisi, M. A. Ratner, *Nano Letters* **2004**, *4*, 591.

[9] B. L. Feringa, Ed., *Wiley-VCH, Weinheim* **2001**.

[10] B. L. Feringa, *Nature* **2000**, *408*, 151.

[11] V. Balzani, A. Credi, F. M. Raymo, J. F. Stoddart, *Angewandte Chemie-International Edition* **2000**, *39*, 3349.

[12] R. Eelkema, M. M. Pollard, J. Vicario, N. Katsonis, B. S. Ramon, C. W. M. Bastiaansen, D. J. Broer, B. L. Feringa, *Nature* **2006**, *440*, 163.

[13] C. P. Collier, E. W. Wong, M. Belohradsky, F. M. Raymo, J. F. Stoddart, P. J. Kuekes, R. S. Williams, J. R. Heath, *Science* **1999**, *285*, 391.

[14] J. R. Heath, J. F. Stoddart, R. S. Williams, *Science* **2004**, *303*, 1136.

[15] D. K. James, J. M. Tour, *Chemistry of Materials* **2004**, *16*, 4423.

[16] N. J. Tao, *Nature Nanotechnology* **2006**, *1*, 173.

[17] R. L. McCreery, *Chemistry of Materials* **2004**, *16*, 4477.

[18] M. Mayor, H. B. Weber, *Angewandte Chemie-International Edition* **2004**, *43*, 2882.

[19] M. Mayor, H. B. Weber, J. Reichert, M. Elbing, C. von Hanisch, D. Beckmann, M. Fischer, *Angewandte Chemie-International Edition* **2003**, *42*, 5834.

[20] J. Chen, M. A. Reed, C. L. Asplund, A. M. Cassell, M. L. Myrick, A. M. Rawlett, J. M. Tour, P. G. Van Patten, *Applied Physics Letters* **1999**, *75*, 624.

[21] L. Venkataraman, J. E. Klare, C. Nuckolls, M. S. Hybertsen, M. L. Steigerwald, *Nature* **2006**, *442*, 904.

[22] B. Q. Xu, N. J. J. Tao, *Science* **2003**, *301*, 1221.

[23] J. Chen, M. A. Reed, A. M. Rawlett, J. M. Tour, *Science* **1999**, *286*, 1550.

[24] J. L. He, B. Chen, A. K. Flatt, J. J. Stephenson, C. D. Doyle, J. M. Tour, *Nature Materials* **2006**, *5*, 63.

[25] M. A. Reed, C. Zhou, C. J. Muller, T. P. Burgin, J. M. Tour, *Science* **1997**, *278*, 252.

[26] Z. J. Donhauser, B. A. Mantooth, K. F. Kelly, L. A. Bumm, J. D. Monnell, J. J. Stapleton, D. W. Price, A. M. Rawlett, D. L. Allara, J. M. Tour, P. S. Weiss, *Science* **2001**, *292*, 2303.

[27] D. P. Long, J. L. Lazorcik, B. A. Mantooth, M. H. Moore, M. A. Ratner, A. Troisi, Y. Yao, J. W. Ciszek, J. M. Tour, R. Shashidhar, *Nature Materials* **2006**, *5*, 901.

[28] L. Wang, M.-H. Yoon, G. Lu, Y. Yang, A. Facchetti, T. J. Marks, *Nature* **2006**, *5*, 893.

[29] C. Li, J. Ly, B. Lei, W. Fan, D. Zhang, J. Han, M. Meyyappan, M. Thompson, C. Zhou, *P. Phys. Chem. B* **2004**, *108*, 9646.

[30] J. H. Schön, S. Berg, C. Kloc, B. Batlogg, *Science* **2000**, *287*, 1022.

[31] J. H. Schon, H. Meng, Z. N. Bao, *Science* **2001**, *294*, 2138.

[32] J. E. Green, J. W. Choi, A. Boukai, Y. Bunimovich, E. Johnston-Halperin, E. DeIonno, Y. Luo, B. A. Sheriff, K. Xu, Y. S. Shin, H. R. Tseng, J. F. Stoddart, J. R. Heath, *Nature* **2007**, *445*, 414.

[33] E. Stern, J. F. Klemic, D. A. Routenberg, P. N. Wyrembak, D. B. Turner-Evans, A. D. Hamilton, D. A. LaVan, T. M. Fahmy, M. A. Reed, *Nature* **2007**, *445*, 519.

[34] A. Ulman, *Chem. Rev.* **1996**, *96*, 1533.

[35] G. Poirier, *Chem. Rev.* **1997**, *97*, 1117.

[36] A. M. Moore, A. A. Dameron, B. A. Mantooth, R. K. Smith, D. J. Fuchs, J. W. Ciszek, F. Maya, Y. X. Yao, J. M. Tour, P. S. Weiss, *Journal of the American Chemical Society* **2006**, *128*, 1959.

[37] R. A. Wassel, R. R. Fuierer, N. J. Kim, C. B. Gorman, *Nano Letters* **2003**, *3*, 1617.

[38] G. K. Ramachandran, T. J. Hopson, A. M. Rawlett, L. A. Nagahara, A. Primak, S. M. Lindsay, *Science* **2003**, *300*, 1413.

[39] A. S. Blum, J. G. Kushmerick, D. P. Long, C. H. Patterson, J. C. Yang, J. C. Henderson, Y. X. Yao, J. M. Tour, R. Shashidhar, B. R. Ratna, *Nature Materials* **2005**, *4*, 167.

[40] N. Katsonis, T. Kudernac, M. Walko, S. J. van der Molen, B. J. van Wees, B. L. Feringa, *Advanced Materials* **2006**, *18*, 1397.

[41] J. M. Lehn, *Science* **2002**, *295*, 2400.

[42] T. Murata, Y. Morita, K. Fukui, K. Sato, D. Shiomi, T. Takui, M. Maesato, H. Yamochi, G. Saito, K. Nakasuji, *Angewandte Chemie-International Edition* **2004**, *43*, 6343.

[43] F. Schreiber, *Progress in Surface Science* **2000**, *65*, 151.

[44] J. C. Love, L. A. Estroff, J. K. Kriebel, R. G. Nuzzo, G. M. Whitesides, *Chem. Rev.* **2005**, *105* 1103.

[45] M. R. Anderson, M. N. Evaniak, M. Zhang, *Langmuir* **1996**, *12*, 2327.

[46] N. Camillone, *Langmuir* **2004**, *20*, 1199.

[47] N. Camillone, T. Y. B. Leung, G. Scoles, *Surface Science* **1997**, *373*, 333.

[48] F. Bensebaa, C. Bakoyannis, T. H. Ellis, *Mikrochimica Acta* **1997**, 621.

[49] F. Bensebaa, R. Voicu, L. Huron, T. H. Ellis, E. Kruus, *Langmuir* **1997**, *13*, 5335.

[50] A. Kudelski, P. Krysinski, *Journal of Electroanalytical Chemistry* **1998**, *443*, 5.

[51] F. T. Arce, M. E. Vela, R. C. Salvarezza, A. J. Arvia, *Electrochimica Acta* **1998**, *44*, 1053.

[52] F. T. Arce, M. E. Vela, R. C. Salvarezza, A. J. Arvia, *Journal of Chemical Physics* **1998**, *109*, 5703.

[53] H. Rieley, N. J. Price, R. G. White, R. I. R. Blyth, A. W. Robinson, *Surface Science* **1995**, *331-333*, 189.

[54] M. Yu, N. Bovet, C. J. Satterley, S. Bengio, K. R. J. Lovelock, P. K. Milligan, R. G. Jones, D. P. Woodruff, V. Dhanak, *Physical Review Letters* **2006**, *97*.

[55] A. Badia, R. B. Lennox, L. Reven, *Accounts of Chemical Research* **2000**, *33*, 475.

[56] L. A. Bumm, J. J. Arnold, L. F. Charles, T. D. Dunbar, D. L. Allara, P. S. Weiss, *Journal of the American Chemical Society* **1999**, *121*, 8017.

[57] G. E. Poirier, *Langmuir* **1999**, *15*, 3018.

[58] K. D. Truong, P. A. Rowntree, *J. Phys. Chem.* **1996**, *100*, 19917.

[59] R. Staub, M. Toerker, T. Fritz, T. Schmitz-Hubsch, F. Sellam, K. Leo, *Langmuir* **1998**, *14*, 6693.

[60] S. Xu, S. J. N. Cruchon-Dupeyrat, J. C. Garno, G. Y. Liu, G. K. Jennings, T. H. Yong, P. E. Laibinis, *Journal of Chemical Physics* **1998**, *108*, 5002.

[61] G. E. Poirier, E. D. Pylant, *Science* **1996**, *272*, 1145.

CHAPTER 2

EXPERIMENTAL TECHNIQUES

In this chapter we will provide a few details on the basic principle for each technique employed to perform the experimental work showed in this thesis.
Theoretical basis on Scanning Tunneling Microscopy (STM) will be given in session 2.1 together with a short overview on the nature of the STM image contrast on molecules adsorbed on conductive substrates. A few concepts on the Cyclic Voltammetry measurement performed during this thesis work will be provided in session 2.2.
Fourier Transform Infrared Reflection Absorption Spectroscopy is described in session 2.3 where also a general treatment of the measured absorption spectra is given. The absorbance of a thin film on a metal is also discussed.

2.1 Scanning Tunneling Microscopy (STM)

The development of the scanning tunneling microscope (STM) by Binnig and Rohrer[1][i] in the early 1980 opened a new field in surface science, as it made it possible to perform a real-space investigation of atomically resolved metal and semiconductor surfaces as well as to address studies on individual atomic and molecular adsorbates.[2-5] During the STM measurements a voltage is applied between a conductive surface and a very sharp probe tip scanning few Å above the sample surface (Fig. 2.1).

[i] Nobel Prize in Physics, 1986, G. Binnig, H. Rohrer.

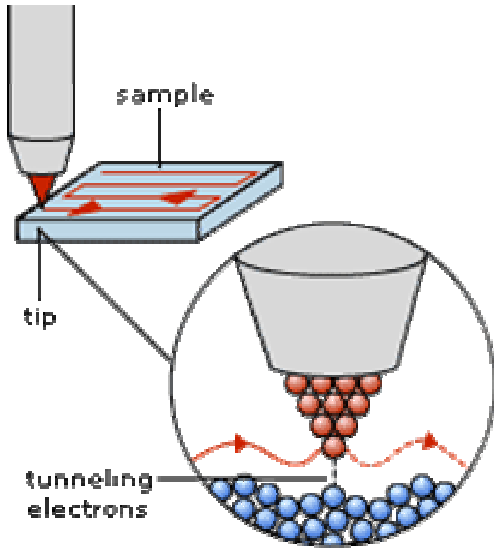

Figure 2.1: Schematic drawing of the STM probe scanning on a sample.

STM imaging relies on the quantum mechanical tunneling effect which enables electrons to cross the vacuum barrier between two electrodes, i.e. the tip and the surface, resulting in a tunneling current, I (Fig. 2.2).

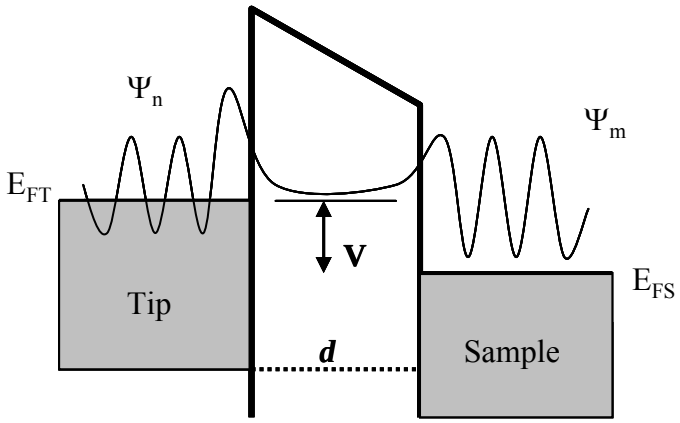

Figure 2.2: Scheme of the tunneling process. Electrons have a non zero probability to be found in the gap, therefore they can tunnel through the barrier.

The tunneling current flowing between the tip and the sample is exponentially dependent on the distance (z) between the two electrodes (Fig. 2.3). In practice for a given voltage, the closer is the tip to the surface the highest is the measured current. The scan through the z (vertical), x and y (horizontal) distances is ensured by a piezoelectric element (piezo). High voltage ramps applied to the piezo drive the x and y movements while the z

direction is controlled by a feedback loop which compares I to a given current set-point value for each position (x, y) and applies an appropriate voltage to the z-piezo which approaches or retracts the tip in order to keep I constant (constant current mode).

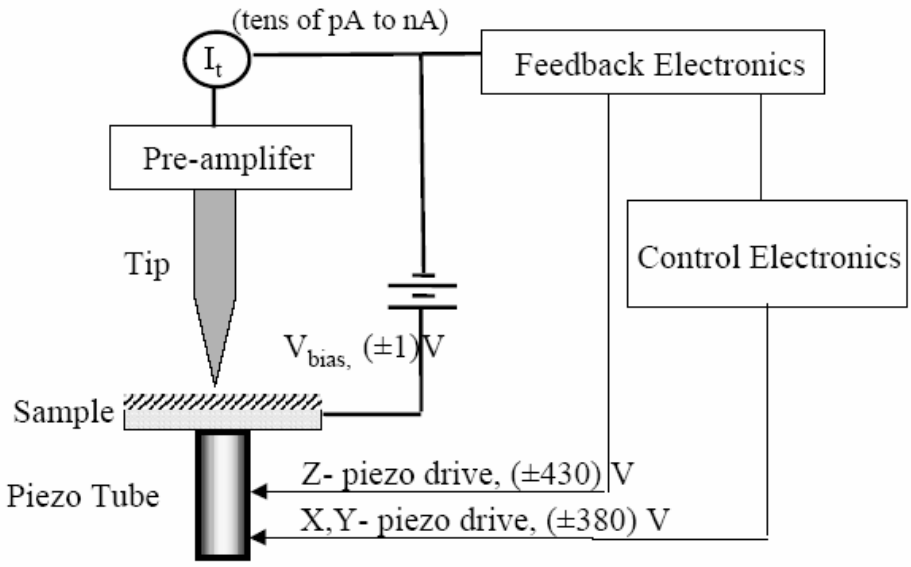

Figure 2.3: Set-up of Scanning Tunneling Microscope (STM).

The voltage and current parameters for the tunneling vary according to the electronic properties of the tip and the sample under study.[6] The output image can be derived from two different signal detected during the measurement: the voltage applied by the feedback loop to the piezoelectric element, which gives the STM topography and, the actual tunneling current originating the current image. The measurement can be carried in constant height mode or in constant current mode (also said constant gap width mode). In the constant height mode, where the feedback-loop is extremely slow, the variation in image contrast will be reflected in the current image. In this mode the tip is scanning without big adjustments of the z-height (constant height). In the constant current mode the feedback loop reacts quickly to the current variation and the image contrast will be seen in the topography channel while the image contrast of the current image will be low (Fig. 2.4).

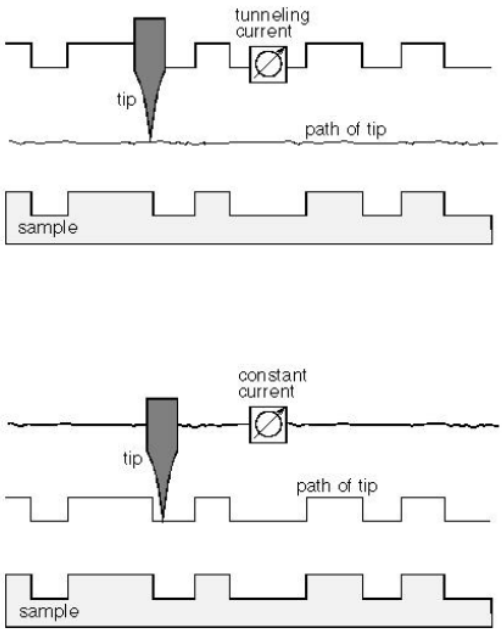

Figure 2.4: Top scheme: constant-height imaging mode; below: constant-current mode for STM.

Different model with different levels of complexity have been proposed to describe the STM measurements.

The quantum mechanical tunneling is based on the wavelike nature of electrons. This property leads to a finite probability for electrons to cross a potential barrier V_0 which is higher than their kinetic energy E. For a rectangular barrier, the barrier transmission coefficient T is exponentially dependent on z and the square root of the effective barrier height ($V_0 - E$):

$$T \propto e^{-2kz} \qquad \text{with} \qquad k = \frac{[2m(V_0 - E)]^{1/2}}{\hbar} \tag{2.1}$$

According to the Bardeen formalism the tunnelling current can be described as a sum of transition probabilities between electronic states of the tip and the sample.[7]

In a first-order perturbative treatment of tunneling for a three-dimensional barrier, the tunneling current I between two independent planar electrodes is evaluated for a weak wave function overlap to:

$$I(V) = \frac{2\pi e}{\hbar} \sum_{\mu,\nu} |M_{\mu\nu}|^2 \delta(E_\mu - (E_\nu + eV)) \times \{ f(E_\mu, T)[1 - f(E_\nu, T)] - f(E_{\nu,} T)[1 - f(E_\mu, T)] \} \tag{2.2}$$

for an applied voltage V between the electrodes and a summation over all eigenfunctions Ψ_μ of the tip and Ψ_υ of the sample having eigenenergies E_μ and E_f with respect to their Fermi levels $E_{F,t}$ and $E_{F,s}$, respectively. The Fermi-Dirac function f(E, T) gives the probability that an electronic state of energy E is occupied at the temperature T and the δ-function accounts for an elastic tunneling process. $M_{\mu\nu}$ is the transition matrix element which evaluates the overlap of the wavefunctions μ and ν in the gap region and which represents the main difficulty of the calculation.

Energy diagrams of the tunneling junction without and with an applied voltage V are depicted in Fig. 2.4.

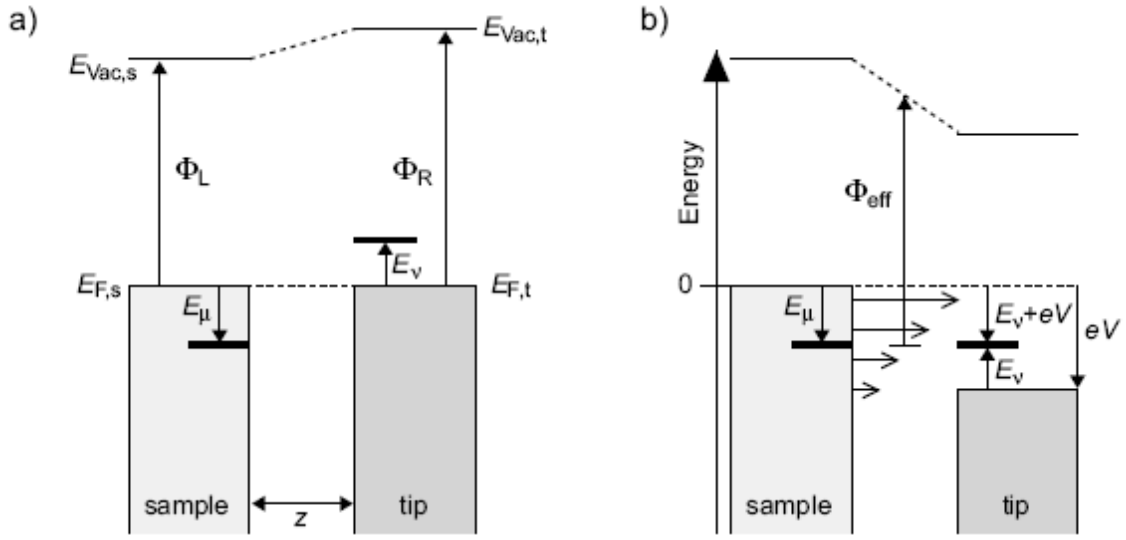

Figure 2.4: Schematic energy diagram of the tunnel junction **a)** without an applied bias voltage **b)** with an applied voltage V between tip and sample.

Tersof and Hamann[8] applied this approach to the calculation of the tunneling current in STM and simplified it by restricting the external conditions to a locally spherical tip having only s-type wavefunctions and to the regime of low temperatures and small voltages V which reduces Eq. 2.2 to:

$$I(V) = \frac{2\pi e^2}{\hbar} V \cdot \sum_{\mu,\nu} \left| M_{\mu\nu} \right|^2 \delta(E_\mu - E_\nu) \cdot \delta(E_\nu - E_F) \qquad (2.4)$$

The application of explicit wave functions for the sample and for an idealized tip with a radius of curvature R at a position $\vec{r_0}$ simplifies Eq. 2.4 to

$$I(V) \propto V \cdot \rho_t(E_F) e^{2kR} \sum_{\mu} \left|\Psi_\mu\left(\vec{r_0}\right)\right|^2 \delta(E_\nu - E_F) \tag{2.5}$$

with $k = \sqrt{2m\Phi_{eff}}/\hbar$ being the inverse decay length for the wave functions in vacuum, Φ_{eff} the effective local potential barrier height and $\rho_t(E)$ the density of states of the tip. Consequently, for constant V the tunneling current I is proportional to the local density of states (LDOS) of the sample $\rho_s(\vec{r},E)$ at the position $\vec{r_0}$:

$$I \propto \rho_s\left(\vec{r_0}, E_F\right) \text{ with } \rho_s\left(\vec{r_0}, E\right) \equiv \sum_{\mu} \left|\Psi_\mu\left(\vec{r_0}\right)\right|^2 \delta(E_\mu - E) \tag{2.6}$$

Eq. 2.6 gives an interpretation of the contrast in STM images for scanning at constant current and small voltage in terms of a contour of constant LDOS of the sample at the Fermi level. The exponential decay of the wave functions in the z-direction normal to the surface yields to $\left|\Psi_\mu\left(\vec{r_0}\right)\right|^2 = e^{-2k(z+R)}$. A substitution into Eq. 2.5 gives:

$$I \propto e^{-2kz} \tag{2.7}$$

describing the exponential dependence of I on the tip-sample distance z.

Fig. 2.5 is a schematic drawing of the $E_{F,s}$ and $E_{F,t}$ repositioning according to the applied voltage and therefore the tunneling current flow direction.

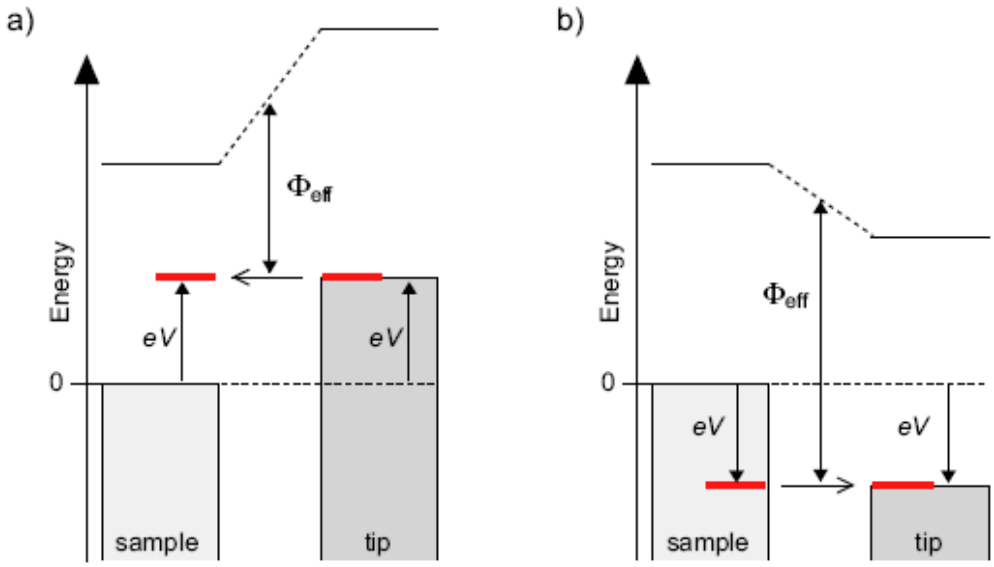

Figure 2.5: Schematic energy diagram revealing the asymmetry of the tunnel junction a) for a negatively polarized tip (positive bias voltage) the electrons tunnel from the occupied sample states into unoccupied states of the tip, b) for a positively polarized tip (negative bias voltage) electrons flow from the sample to the tip.

Very sharp metal tips are usually used in STM imaging and the tip radius of curvature is usually few tens of nm. Nearly 100% of the current in the tunneling junction is transported via the tip apex (Fig. 2.6) allowing the achievement of a lateral resolution of ~ 1Å.

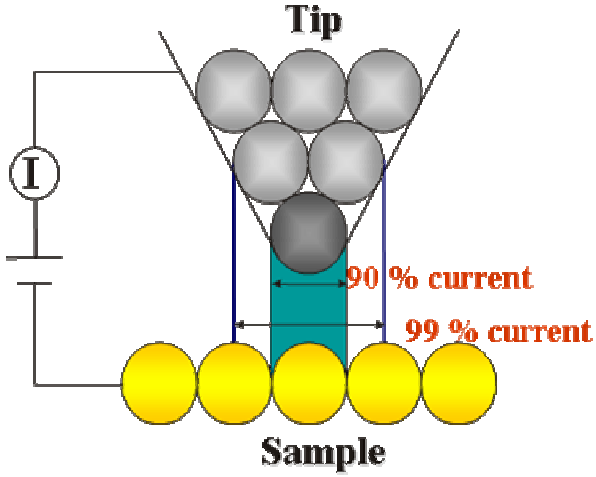

Figure 2.6: Schematic of the STM junction current flow.

Considering the typical metal work functions a value of 4eV is found for the Φ_{eff}, then from equation 2.7, if the z value rise of 1Å the tunneling current vary of one order of

magnitude. This high sensitivity of the tunneling current to the vertical displacement of the scanning tip is responsible for the very high resolution reached by the technique.

2.1.2 Imaging molecules adsorbed on solid substrates

The precise mechanism which renders the adsorbates visible in the STM images remains partially unclear, especially because of difficulties in perfectly describing the transition matrix. Tersoff and Hamann showed that at low bias and constant current the STM imaging provides a map of constant local density of state at the Fermi level. The image contrast of a particular adsorbate depends on the perturbation it induces on this state density, therefore the image contains electronic information of both the symmetry of the molecular orbital and adsorption sites on the substrates. The computed image usually considers the overlap (mixing or hybridization) of metal and molecular states near the Fermi level. To simplify calculation the conductive substrate is reduced to the dimension of a cluster of atoms. As the number of atoms in the cluster increases, the population of metal states near the Fermi energy $E_{F,s}$ also increases and the probability of mixing between molecular and metal states increases too. For low bias voltages only states near to the Fermi level participate to the tunneling.[9] For the regimes of low bias the molecular orbital which participate predominantly to the tip-sample states overlap are the HOMO (Highest Occupied Molecular Orbilats) and LUMO (Lowest Occupied Molecular Orbilats) levels as they are closer to the E_F of the two metal electrodes (tip and substrates).

The contribution of atomic or molecular levels to the LDOS at E_F of the conductive substrate, allows the imaging of adsorbates even if the HOMO and LUMO levels are separated by several eV, as calculated for adsorbed xenon[10] and benzene.[11-13]

It is very important to stress the following point: STM does not provide topographic information of adsorbed molecules in a straightforward manner. The broadening of an adsorbate level located far away from E_F results in an extended tail of this resonance which contributes to the LDOS at E_F and this increases the brightness of the image contrast at the molecule location on the substrate. Depletion of the local density of states at the E_F has also been observed. In the last case molecules appear as depressions in the STM images (darker contrast with respect to the substrate surface image contrast).

The broadening or the depletion of the electron density at the Fermi level strongly depends on the specific adsorption mechanism therefore on the electronic interaction of

adsorbate and sample. An example of depletion of density of states at the Fermi level is the one induced by the adsorption on a metal of helium[9], carbon[14] and carbon monoxide.[15-17]. The STM technique has the ability to map the HOMO and LUMO levels of organic molecules adsorbed on solid substrates although, the contribution of the metal substrate to those orbitals have to be considered. For some organic compound like C60[18] and flat-lying π-conjugated molecules[19, 20] a good match between the calculated and measured images has been obtained.

2.1.3 Origin of the STM image contrast in SAMs

STM provided important information on the assembly mechanisms and structural features of SAMs. Usually positive bias are used to image the SAM sample allowing the electrons to tunnel from the metal tip, through the SAM layer, to reach finally the substrate. In fact, high positive biases determine the reductive desorption of the thiolated molecule (see session 2.2). The electrons flow across two main regions: the gap between the tip and the monolayer interface (air or vacuum) and the isolating molecular layer. The different regions are schematized in Fig. 2.7. Each of them is characterized by a well defined thickness (d_{gap} and d_{SAM}) and conductance (G_{gap} with decay constant α and G_{SAM} with decay constant β).[21]

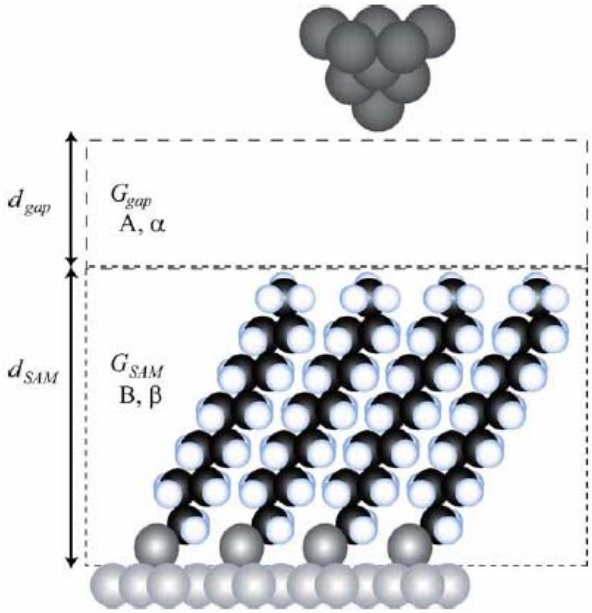

Figure 2.7: Schematic representation of a SAM/STM junction: d_{gap} and d_{SAM} indicates the thickness of the two regions; G_{gap} and G_{SAM} are the conductance of the gap and SAM respectively.

In their previous work Bumm and co-workers found that the conductance of an insulating thin monolayer can be described by a double-layer tunnel junction model, where the conductance ($G_{double\text{-}layer}$) is defined as:

$$G_{double\text{-}layer}=G_{gap}\times G_{SAM} \tag{2.8}$$

where $G_{gap}= Ae^{(-\alpha dgap)}$ and $G_{SAM}= Be^{(-\beta dSAM)}$; the prefactors A and B being the contact conductance, α and β are the decay constant and d_{gap} and d_{SAM} are the thickness of the gap and of the monolayer respectively.[21]

According to the chemical nature of the thiols and its electron transport properties reflected by the β factor, different tunneling characteristic are determined and therefore different images are obtained.[22]

However, even using a preamplifier for measuring picoamperes currents, the thickness of an insulating layer above a conductive substrate should not exceed 20Å. This means that for relatively long chain the tip can penetrate in the monolayer. The resulting interactions forces can perturb the monolayer structure and also induce the molecular desorption from the SAM. Therefore, in order to obtain the molecular resolution on SAMs it is important to operate with high tunneling impedance, corresponding to high distances between the substrate and the tip. On the other hand a length of at least 9 methylene units stabilizes the lateral packing in the SAM.

It is commonly stated that the high resolution contrast obtained above the $(\sqrt{3}\times\sqrt{3})R30°$ is due to the electron density of state located at the Au-S binging sites.[23, 24] However, studies carried out on molecular junction embedding SAMs it has been observed that the tunneling process also involve the backbone molecular orbital.[25] Therefore, for a correct interpretation of the STM image contrast on SAMs the contribution of the molecular orbital to the tunneling process should be considered together with the electron density of states located at the Au-S binding site.[26]

2.2 Electrochemistry: Cyclic Voltammetry on SAMs

This session is not aimed at providing a thorough description of the principles of the cyclic voltammetry (CV) measurements, but it is rather intended to describe its use to study

SAMs chemisorbed on gold substrates. In CV measurements a potential cycle is applied to the working electrode (Fig. 2.8). The working electrode is the electrode sensing the redox processing involving the target sample. During the potential scan sample redox processing might occur at the working electrode if specific potentials corresponding to the reduction or to the oxidation of the sample are reached. The redox process is detected through the current measured by the electrode as showed in figure Fig. 2.8.

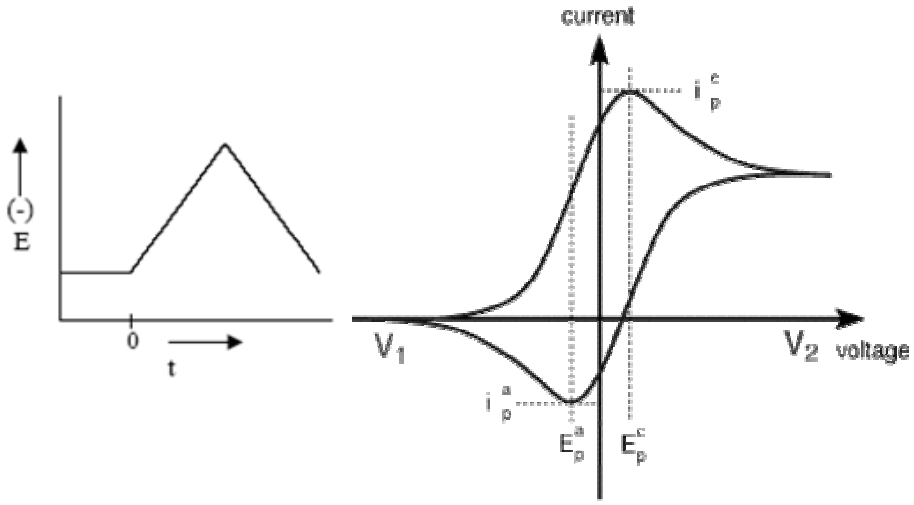

Figure 2.8: Left: cyclic potential ramp run during the CV measurements. Right: scheme of a potential cyclic scan over and electrode immersed in a solution containing a reversible redox couple. I^c is the cathodic current measured for a detected reduction process, at more negative voltages E^c. I^a is the anodic current measured for a detected oxidation process occurring at more positive voltages E^c.

To perform CV on SAMs, a SAM modified gold electrode is immersed into an electrochemical cell with a counter (usually a Pt wire) and a reference electrode (usually an Ag/AgCl reference electrode).

The tightness of the packing of SAMs can be studied by investigating the diffusion capability of a reversible redox-active species (e.g. $K_3[Fe(CN)_6]$ or $Ru(NH_3)_6^{+3/+2}$) through the SAMs. The redox species can permeate the organic SAM when it is loosely packed, leading to the occurrence of a redox process at the gold electrode surface.[27-29] Then, both cathodic and anodic currents arising from reaction (I) are observed in the cyclic voltammogram.

$$Fe^{3+} + e^{-} \leftrightarrow Fe^{2+} \qquad (I)$$

Thick monolayer formed by long n-alkanethiols which allow for the tight packing of the chains, provide up to 99% electrochemical blocking effect (EBE).[30] Pinholes or other defects present in the SAM are favorite sites for the permeation of the redox species to the underlying Au substrate. In films of undecanethiol permeation of the redox species through the monolayer toward the gold surface is prevented and CV curves are essentially flat (black curve in Fig. 2.9). In contrast, measurements on a bare gold electrode clearly show oxidation and reduction peaks (red curve).

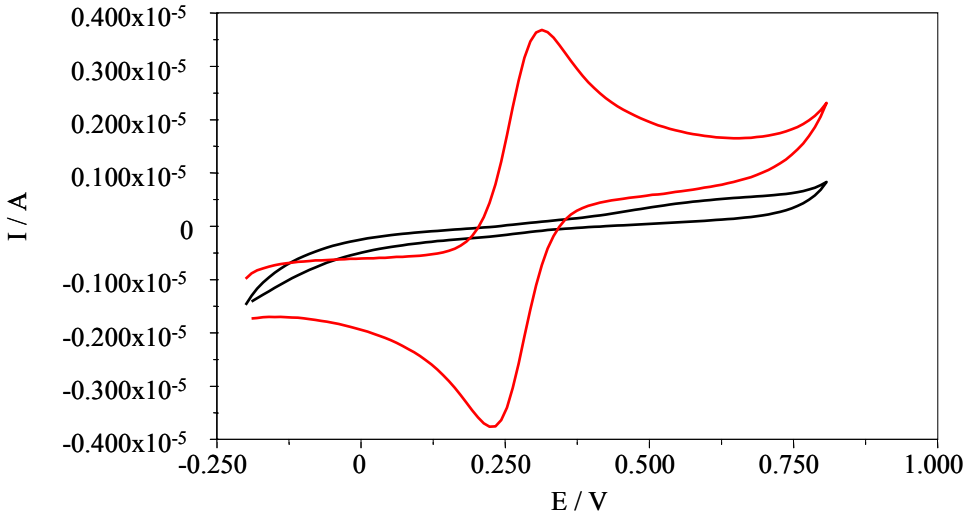

Figure 2.9: Black curve: blocking effect generated by an undencathiol monolayer chemisorbed on gold electrode (working electrode). Red curve: bare electrode. $K_3Fe(CN)_6$ 1mM , KCl 1M, scan rate=50mV/s; the counter electrode is a Pt wire and an Ag/AgCl electrode has been used as reference electrode.

By cycling the potential applied to the gold electrode, the desorption (reductive, negative potential E_c) and possibly re-adsorption (oxidative, positive potential, E_a) behavior, which occurs according to reaction (II), can also be studied.

$$Au\text{-}S\text{-}R + e^{-} \leftrightarrow Au + {}^{-}S\text{-}R \qquad (II)$$

Since desorption characteristics depend on the environment of the gold-sulfur bond (including type of molecule, type of binding site and lateral packing), such an experiment can be useful to further confirm the binding of the thiolated molecules. If the binding is homogeneous over the whole gold substrate, an intense and sharp reductive (desorption) peak should be observed as well as an oxidative re-adsorption peak (Fig. 2.10).[31-36]

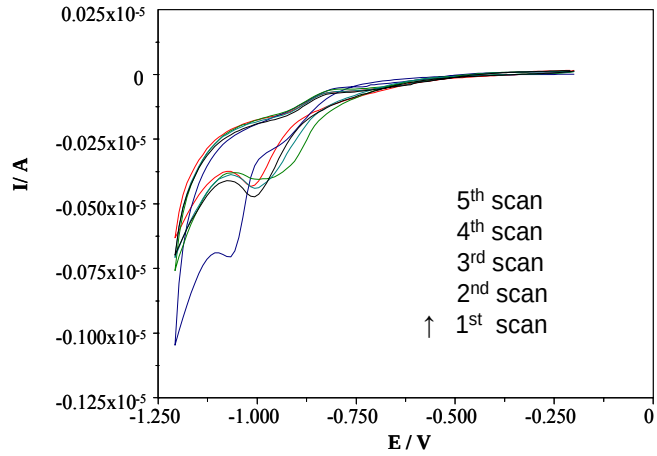

	Peak position (V)	Width (V)	Ep-Ep\2 (1\V)
1st scan	Reduction: -1.01 Oxidation: -0.814	0.08 0.09	-0.042 0.049
2nd scan	Reduction: -0.945 -0.824	0.14 0.11	-0.067 0.051

Figure 2.10: CV plots undecanthiol SAM of $C_{11}SH_{24}$, 1 night incubation in 1mM solution in $CHCl_3$ solvent. (0.5 M KOH 100 mV/s)

The reductive potential varies according to the molecular structure of the thiols and usually ranges from -0.75 V (as for *n*-undecanethiol) to -1.12 V (as for n-hexadecanethiol) with respect to Ag/AgCl electrodes. This potential difference makes it possible to selectively desorb specific thiols with respect to the other when a multi-component SAM is formed.[37]

2.3 Infrared (IR) spectroscopy

Optical vibrational spectroscopy is less sensitive than the electron-based techniques but is generally applicable to all kinds of interfaces. Each molecule has its own specific vibrational spectrum (finger print); the development of reflection IR vibrational spectroscopy made it possible to obtain structural information of the film studied.[38, 39]

According to IR selection rules light absorption from molecular vibrations is possible if the vibration is coupled with a change in the vibrational dipole moment (μ) and if the vibrational wavenumber is identical to the wavenumber of the incident radiation. Fundamental vibrations can be divided into four types:

1- Stretching vibrations where one or more bonds is lengthened or shortened;

2- Planar bending vibrations which involve only the variation of the bond angles;

3- Out-of-plane bending vibrations where one atom oscillates through a plane defined by (at least) three neighboring atoms;

4- Torsion vibrations where a dihedral angle (the angle between two planes, whose intersection line contain a bond) is varied.

These types of vibration are illustrated in Fig. 2.11.

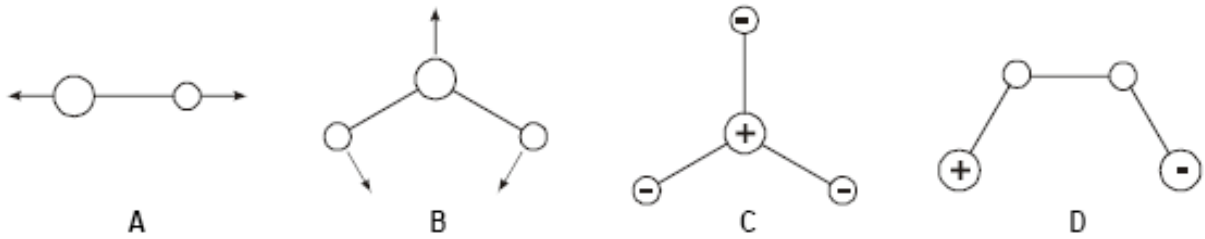

Figure 2.11: Schematic of the fundamental vibrations: stretching vibrations **(A)**, planar bending vibrations **(B)**, out-of-plane bending vibrations **(C)** and torsion vibrations **(D)**. The plus and minus sign indicates movements outside and inside the plane respectively.

The bending vibrations can be distinguished as rocking, twisting and wagging bands. Stretching vibrations adsorb at higher wavenumber regions than planar bending vibrations. Out-of-plane bending will be visible at lower wavenumbers than the planar bending vibrations and the torsion bands are visible at the lowest wavenumbers.

Vibrations can retain the group symmetry of the bond (symmetric vibration, sym) or they can change one or more of the symmetry elements of the molecule (asymmetrical vibrations, asym). Combination bands between two bands of different wavenumber and overtones may appear at twice or three times the wavenumber of the fundamental vibration and appear with a lower intensity. A simple harmonic oscillator model can be use to describe the vibration involving two atoms:

$$\nu = 2\pi\sqrt{\frac{k}{m}} \tag{2.8}$$

where k is the force constant of the bond and m is the reduced mass of the two atoms. For organic compound two interesting regions can be considered: the CH stretching vibrations

region visible at around 3000 cm^{-1} and the fingerprint region found from 800 to 1800 cm^{-1}.[40]

2.3.1 The FT-IR spectrometer

The main part of a FI-IR is represented by the interferometer.[41] In an interferometer a polychromatic beam of radiation is divided into two beams, which are recombined after a path length difference has been introduced Fig. 2.12. The recombination of the two beams originates a light intensity dependence on the path length difference. The resulting beam from the Michelson interferometer is focused in a sample compartment ad after absortion the light-beam reach the detector.

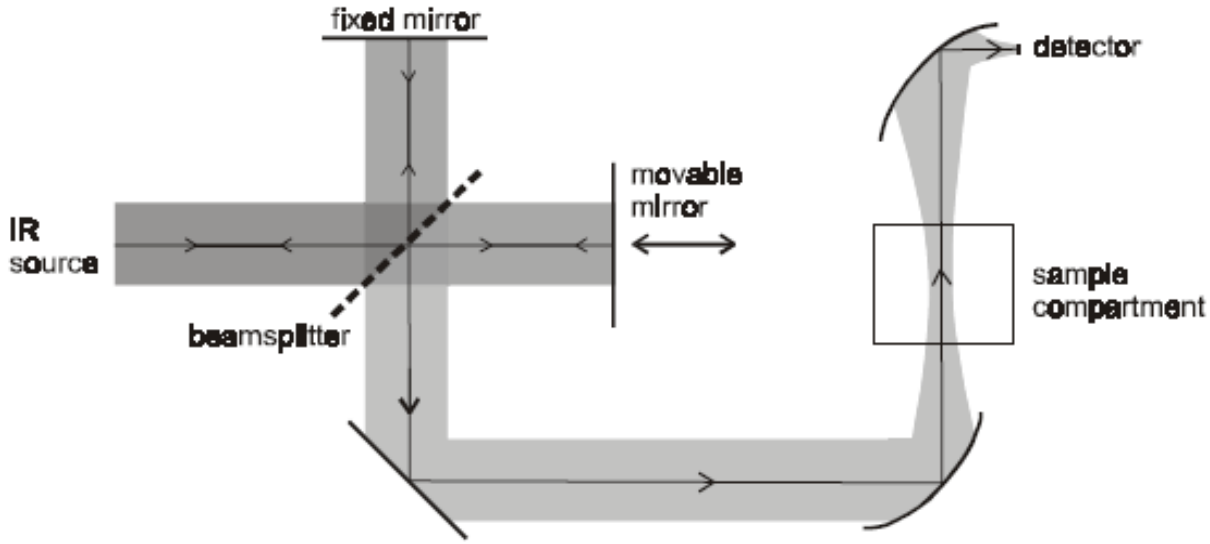

Figure 2.12: Schematic representation of the FT-IR spectrometer.

Only the varying part of the measured intensity is of interest for FT-IR spectroscopy, this signal is called the interferogram, I(δ), which is written as:

$$I(\delta) = \int_{-\infty}^{+\infty} [B(\nu)\cos 2\pi\nu\delta]d\nu \tag{2.11}$$

The Fourier transform of I(δ) give the spectrum of the light source:

$$B(\nu) = 2\int_{0}^{+\infty} [I(\delta)\cos 2\pi\nu\delta]d\delta \tag{2.12}$$

In practice the retardation cannot be sampled at infinitely small distances. However relatively small distances can be achieved which can be controlled by a calibration He-Ne laser that also passes the interferometer. Instrumental characteristics such as beam-splitter efficiency, mirrors or detector response which influence the light intensity of the source should also be considered.

Water contained in the atmosphere interferes in the measurement because of its very strong, sharp absorption bands around 1700 and 3700 cm^{-1}. The amount of water vapor in the atmosphere within the spectrometer can be reduced by purging with dry nitrogen gas or by putting the optical part of the FT-IR spectrometer in vacuum.

2.3.2 FT-IR Reflection Absorption Spectroscopy of Thin Layers

An important advantage of reflection absorption spectroscopy is the also IR-absorbing substrate can be used. In between the different IR technique developed in reflection-absorption mode the IRRAS and the PM-IRRAS[42] are the one that have been optimized to detect IR spectra of thin film on reflective substrate.[43] Interesting results obtained using of those techniques on SAMs on Au or Ag have been reported in the literature. For anisotropic films on the surfaces like a SAMs chemisorbed on gold the aim of performing FT-IRRAS are both the detection of functional group in the film and the molecular order structure of the film. Optical effect such as peak shift and loss of peak symmetry are typical of thick film and film with high refractive index and broad absorption bands.[44, 45]

2.3.3 Absorbance of a thin anisotropic film on metal substrate

Upon irradiation of a metal substrate with a plane wave at near-normal incidence, the reflected and incident beam can combine to form a standing wave field perpendicular to the substrate. The electric field of the s-polarized light is perpendicular at the plane of incidence and reflection; therefore it has only a component parallel to the metal surface. Upon reflection the s-polarized light is de-phased of 180°, therefore the combination of the incidence and reflected s-light produces electric field parallel to the substrate equal to zero (Fig. 2.13-A). Instead, the incident and reflected p-polarized light have an electric filed component which is perpendicular to the substrate surface and can therefore produce a standing wave field. The intensity of this new standing wave field is four times the intensity

of the irradiating beam as the light intensity is the square of the electric field amplitude. The thin layer will be within this standing wave field being perpendicular to the metal surface and therefore only the vibration transition dipole moment owing a component perpendicular to the metal surface will be detected in the IRRAS spectra.[46-48]

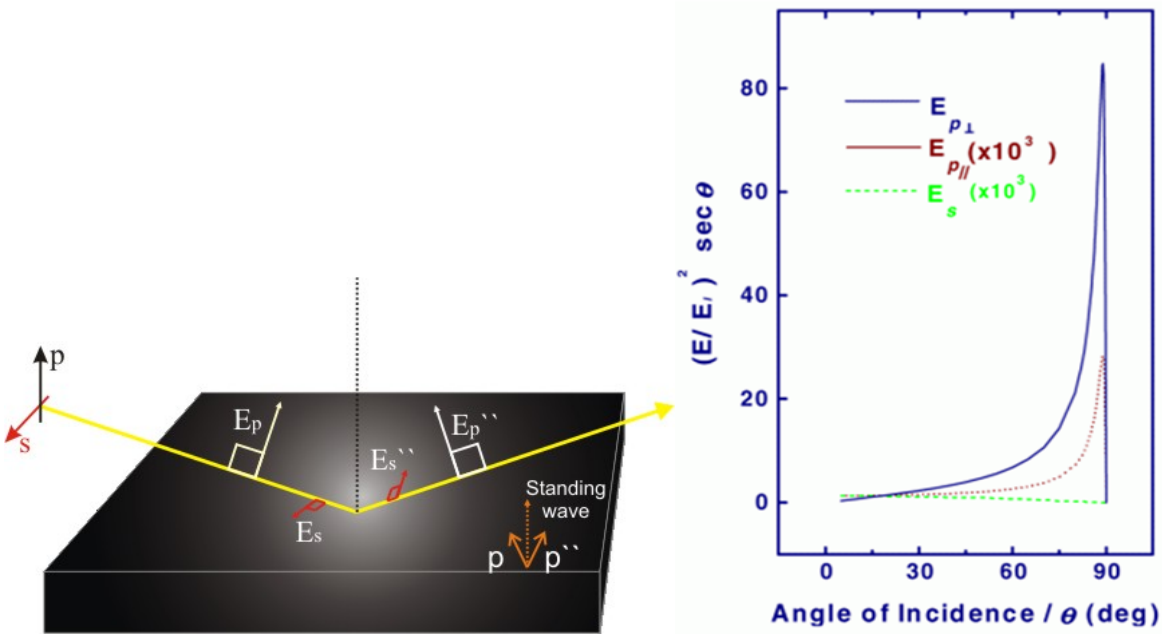

A **B**

Figure 2.13: A) Schematic drawing of the p- and s- polarized light reflected by a metal substrate. **B)** Dependence of square of the electric field amplitude E of the stationary wave on angle of incidence. $E_{p//}$ indicate the p-polarized light component parallel to the substrate; $E_{p\perp}$ is the p-polarized light component perpendicular to the substrate. Note that even if E_p is maximized at near grazing incidence, the E_s is negligible at all incident angles.

Fig. 2.13-B clearly shows a strong dependence of the standing wave field from the angle of incidence, dictated also from the refractive incident variation according to that angle. At around 80° the field intensity is maximized explaining the reason why this incident angle is commonly used in IRRAS spectrometers. The absorbance of a thin layer on a reflective substrate is defined as:

$$A = \frac{R_0 - R}{R_0} \tag{2.13}$$

where R_0 is the reflectance of the clean substrate and R is the reflectance of the adsorbed thin film. The measured absorbance is linearly dependent on the layer thickness in the range of 10nm.[49]

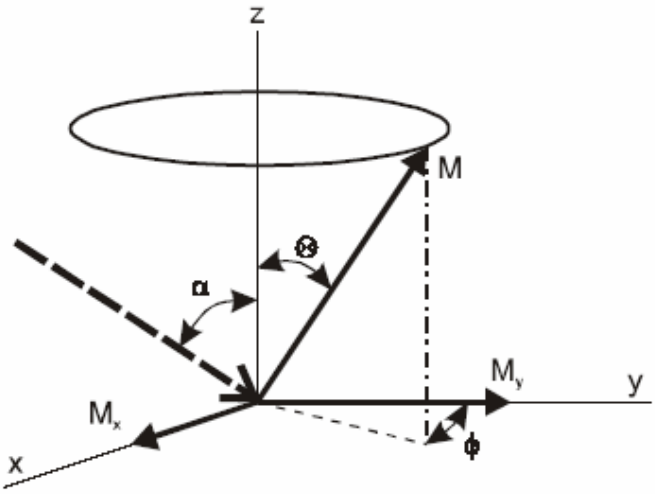

Figure 2.14: Cylinder symmetrical distribution of the transition dipole moment (M) with tilt angle Θ. The z-axis depicts the layer surface normal. The IR beam's plane of reflectance is the yz plane and the angle of incidence (α) is the angle between incident beam and the surface normal in the yz-plane.

In SAMs exist a high anisotropic assembly and we can describe the molecular orientation by assuming a cylinder symmetrical spread of a transition dipole moment with a tilt angle Θ around the surface normal (Fig 2.14). As there is only an electric field perpendicular to the substrate surface the absorbance of a transition dipole moment is thus dependent on the magnitude of this electric field component that depends on the angle of incidence, and on the magnitude of the component of the transition dipole moment that is oriented perpendicular to the substrate surface.[50]

A first approach is to compare the measured absorbance with that of the same layer in a transmission experiment under perpendicular incidence. These two experiments would provide the absorbance perpendicular and parallel to the surface and the orientation of the transition dipole moment can be determined from these values. However, the transmission experiment can not be done on a metal substrate because of the broad absorbance of IR light by metals.

Another possibility is to measure the properties of the material of which the film is composed, this can be done acquiring IR-spectra of the compound in KBr pellets. The absorption coefficient values of the isotropic material can be used to calculate the absorbance of an isotropic film, with the conditions of the reflection experiment. The orientation of the transition dipole moment is can be defined as[51]:

$$\cos^2\Theta(\nu) = \frac{A_{SAM}(\nu)}{A_{iso}(\nu)} \tag{2.14}$$

where A_{SAM} is the measured absorbance in the SAM and A_{iso} is the calculated absorbance of an isotropic film. The orientation of transition dipole moments can therefore be obtained from FT-IRRAS experiments on a metal substrate, but the technique has some disadvantages. In fact, it is worth to stress that not only the absorption coefficient (*k*) but also the refractive index (*n*) of the sample film is factors of normalized reflectivity change. In particular, in case of the film having strong and broad absorption band, the reflection spectra will considerably differ from the transmission spectra of film materials. In the transmission spectra, only the absorption coefficient *k* gives the band shape. On the contrary, the deformation of the band shape accompanied by the shift of the peak position is observed in the reflection spectra because of the anomalous dispersion of the refractive index of the sample. Therefore, careful attention should be paid when trying to obtain monolayer orientation parameter from the IRRAS spectra.

References

[1] G. Binning, H. Rohrer, *Phys. Rev. Lett.* **1986**, *49*, 57.

[2] W. A. Hofer, A. S. Foster, A. L. Shluger, *Reviews of Modern Physics* **2003**, *75*, 1287.

[3] W. A. Hofer, *Progress in Surface Science* **2003**, *71*, 147.

[4] D. Bonnell, *Wiley-CH* **2001**.

[5] B. Bhushan, H. Fuchs, *Springer* **2006**.

[6] M. Aguilar, A. I. Oliva, E. Anguiano, *Europhysics Letters* **1999**, *46*, 442.

[7] J. Bardeen, *Phys. Rev. Lett.* **1961**, *6*, 57.

[8] J. Tersoff, D. R. Hamann, *Phys. Rev. Lett.* **1983**, *50*, 1998.

[9] N. D. Lang, *Phys. Rev. Lett.* **1986**, *56*, 1164.

[10] D. M. Eigler, P. S. Weiss, E. K. Schweizer, N. D. Lang, *1991* **1991**, *66*, 1189.

[11] A. J. Fisher, P. E. Blöchl, *Phys. Rev. Lett.* **1993**, *70*, 3263.

[12] V. M. Hallmark, S. Chiang, K. P. Meinhardt, K. Hafner, *Phys. Rev. Lett.* **1993**, *70*, 3740.

[13] J. Yoshinobu, M. Kawai, I. Imamura, F. Marumo, R. Suzuki, H. Ozaki, M. Aoki, S. Masuda, M. Aida, *Physical Review Letters* **1997**, *79*, 3942.

[14] C. Klink, L. Olesen, F. Besenbacher, I. Stensgaard, E. Laegsgaard, N. D. Lang, *Phys. Rev. Lett.* **1993**, *71*, 4350.

[15] P. Hu, D. A. King, M. H. Lee, M. C. Payne, *Chem. Phys. Lett.* **1995**, *246*, 73.

[16] M. L. Bocquet, P. Sautet, *Surface Science* **1996**, *360*, 128.

[17] L. Bartels, G. Meyer, K. H. Rieder, *Applied Physics Letters* **1997**, *71*, 213.

[18] C. Chavy, C. Joachim, A. Altibelli, *Chem. Phys. Lett.* **1993**, *214*, 569.

[19] J. Lagoute, K. Kanisawa, S. Folsch, *Phys. Rev. B* **2004**, *70*, 245415.

[20] J. K. Gimzewski, C. Joachim, *Science* **1999**, *283*, 1683.

[21] L. A. Bumm, J. J. Arnold, T. D. Dunbar, D. L. Allara, P. S. Weiss, *Journal of Physical Chemistry B* **1999**, *103*, 8122.

[22] M. Salmeron, G. Neubauer, A. Folch, M. Tomitori, D. F. Ogletree, P. Sautet, *Langmuir* **1993**, *9*, 3600.

[23] Y. T. Kim, A. J. Bard, *Langmuir* **1992**, *8*, 1096.

[24] C. Schönenberger, J. A. M. Huethorst, J. Jorritsma, L. G. J. Fokkink, *Langmuir* **1994**, *10*, 611.

[25] O. Seitz, T. Bocking, A. Salomon, J. J. Gooding, D. Cahen, *Langmuir* **2006**, *22*, 6915.

[26] C. A. Widring, C. A. Alves, M. D. Porter, *J. Am. Chem. Soc.* **1991**, *113*, 2805.

[27] S. Terrettaz, A. M. Beck, M. J. Traub, J. C. Fettinger, C. J. Miller, *J. Phys. Chem.* **1995**, *99*, 11216.

[28] E. Sabatini, I. Rubinstein, *J. Phys. Chem.* **1987**, *91*, 6663.

[29] M. D. Porter, T. B. Bright, D. L. Allara, C. E. D. Chidsey, *J. Am. Chem. Soc.* **1987**, *109*, 3559.

[30] C. P. Smith, H. S. White, *Anal. Chem.* **1992**, *64*, 2398.

[31] D. Hobara, O. Miyake, S. Imabayashi, K. Niki, T. Kakiuchi, *Langmuir* **1998**, *14*, 3590.

[32] D.-F. Yang, C. P. Wilde, M. Morin, *Langmuir* **1996**, *12*, 6570.

[33] N. Nishi, D. Hobara, M. Yamamoto, T. Kakiuchi, *Langmuir* **2003**, *19*, 6187.

[34] N. Nishi, D. Hobara, M. Yamamoto, T. Kakiuchi, *Journal of Chemical Physics* **2003**, *118*, 1904.

[35] T. Kakiuchi, H. Usui, D. Hobara, M. Yamamoto, *Langmuir* **2002**, *18*, 5231.

[36] T. Kakiuchi, M. Iida, N. Gon, D. Hobara, S. Imabayashi, K. Niki, *Langmuir* **2001**, *17*, 1599.

[37] T. Sumi, K. Uosaki, *Journal of Physical Chemistry B* **2004**, *108*, 6422.

[38] L. J. Bellamy, *Chapman and Hall, London* **1975**.

[39] B. Stuart, *John Wiley & Sons, Ltd* **2004**.

[40] J. Coates, *John Wiley & Sons Ltd* **2000**.

[41] P. R. Griffiths, J. A. d. Haseth, *John Wiley & Sons, New York* **1986**.

[42] M. J. Green, B. J. Barner, R. M. Corn, *Rev. Sci. Instrum.* **1991**, *62*, 1426.

[43] V. P. Tolstoy, I. V. Chernyshova, V. A. Skryshevsky, *Wiley-Ch* **2003**.

[44] A. Kudelski, *Vibrational Spectroscopy* **2005**, *39*, 200.

[45] W. Knoll, *Annual Review of Physical Chemistry* **1998**, *49*, 569.

[46] R. G. Greenler, *The Journaf of Chemical Physics* **1966**, *44*, 310.

[47] J. D. Devlin, K. Cosani, *J. Phys. Chem.* **1981**, *85*, 2597.

[48] E. Y. Jiang, *Thermo Electron Corporation Editor* **2004**.

[49] W. G. Golden, D. D. Saperstein, M. W. Severson, J. Overend, *J. Phys. Chem.* **1984**, *88*, 574.

[50] M. J. Pilling, P. Gardner, S. Le Vent, *Surface Science* **2005**, *582*, 1.

[51] I. Zawisza, J. Lipkowski, *Langmuir* **2004**, *20*, 4579.

CHAPTER 3

METHODS

3.1 STM Measurements

STM can be carried under a variety of conditions under ultra high vacuum, in air or in liquid. In this thesis we use a commercial STM apparatus able to work in air and at the solid liquid interface. The measurements have been performed at room temperature.

STM images were obtained in constant current mode with a commercial apparatus (multimode Nanoscope IV, Veeco) in air and at room temperature. The STM tips were cut from a Pt/Ir wire (90/10, diameter 0.25 mm). Unit cells were averaged over several images making use of SPIP software (Scanning Probe Image Processor (SPIP) version 2.0, Image Metrology ApS, Lyngby, Denmark). For STM measurement the substrate are glued on a magnetic disk and an electric contact is made with the silver paint (supplied by Aldrich Chemicals).

3.1.2 Investigations at the solid-liquid interface

The STM set-up can be used to perform investigations at the interface between a solid aNd electrically conductive substrate, like Highly Oriented Pyrolitic Graphite (HOPG), and an almost saturated organic solution (Fig. 3.1).[1-3]

The proper selection of the tunneling parameters, tunneling current, I_t (~1 nA), and voltage between tip-sample, U_t (~1V), allows to control the distance tip-sample and therefore to choose to image only the first molecular layer physisorbed on HOPG. The *xy* calibration of

the piezo-element can be done *in-situ* lowering the tunneling impedance, therefore by decreasing tip-sample distance, in order to visualize the HOPG lattice underneath the organic layer. The substrate is usually imaged at low tunneling junction impedances (V_t~ 20mV, I_t ~ 60pA), while molecular adsorbate usually require larger impedances (V_t~ 1.2V, I_t ~ 5-50pA).

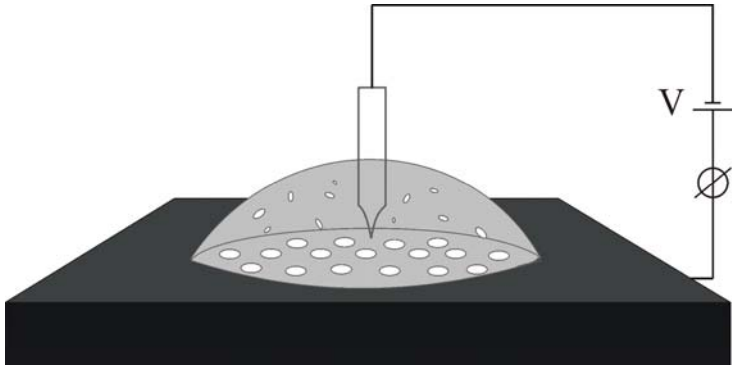

Figure 3.1: Scheme of the solid-liquid interface STM set-up.

These kinds of measurements require the use of a solvent with a low volatility and a low polarity. We employed the following solvents:

- 1-phenyloctane (boiling point, b.p. = 261-263 °C)
- 1,2,4 trichlorobenzene (b.p. = 215-220 °C)
- Tetradecane (b.p. = 252°C)

All these solvents are available from Aldrich Chemicals. When it has been possible it was preferred to use either phenyloctane or tetradecane as trichlorobenzene is highly toxic. The high boiling temperature and low the dielectric constant of these solvents allowed to measure for several hours having the STM tip immersed in the solution.

The HOPG lattice is resolved for 2-4 hours before each measurement session, until the images exhibit a good stability and the thermal stabilization of the instrument is reached. Only at this point a drop of the organic solution is applied to the basal plane of the substrate. Pictures are acquired at the same scan rate and scan length as for the HOPG substrate to make possible to correct the calculated unit cell according to the drift by using the SPIP software.

3.2 Cyclic Voltammetry Measurement

Cyclic Voltammetry (CV) measurements were obtained with an Autolab PGSTAT100 apparatus at room temperature. A standard three-electrode configuration was used with a SAM-coated gold electrode as the working electrode, Ag/AgCl as the reference electrode, and a platinum wire as the counter electrode in a glass vessel.

The SAMs were prepared by immersion of the gold working electrode (2mm gold tip diameter purchased from MetrOhm, France; 1mm gold tip electrode purchased from BasI, England) into the thiols containing solution under N_2 atmosphere. After at least 18 hours of immersion, the electrode was removed from the incubating solution and carefully rinsed by ethanol and immediately put in the CV set-up for the measurements.

The solution used in the blocking experiment contained the redox agent $K_3Fe(CN)_6$ 1 mM in 1 M KCl analyte solution. The sweep rate was set at 50mV/s for this measurement.
Cyclic voltammograms of the reductive desorption of the thiols bound at the gold electrode, were recorded in 0.5 M KOH at 100mV/s. The current was taken to be negative when the reductive desorption proceeded.

3.3 Ultra-flat substrates

In order to obtain good resolution during STM imaging, substrates featuring an atomic flatness over several hundred squared nanometers area are required. The preparation of the substrate plays a key role for the self-assembly of molecules at surfaces.
Layered substrates are widely used for the adsorption of the organic materials and SPM studies. For the present investigations two different commercially available crystalline supports were chosen:

· Muscovite mica (Momentite GmbH, Germany);
· Highly Oriented Pyrolitic Graphite (HOPG) (grade ZYB, Momentive GmbH, Germany).

Both of them can be easily cleaved with adhesive tape. The ease and reproducibility of the sample preparation as well as the chemical inertness and the atomically flatness on the

micrometer scale that can be achieved, render this type of preparation commonly used for Scanning Probe Microscopy investigations of physisorbed samples.

Muscovite mica has been used widely as support for both self-assembly of molecules from solutions and sublimation of a metallic layer in high-vacuum (HV).
HOPG was used as substrate for molecules physisorption in the STM studies.

3.3.1.1 The reconstructed Au (111) surface: Preparation methodologies

Key issues for a reproducible SAM formation are the flatness and the crystallinity of the metallic substrate. Therefore metallic supports have been developed using different procedures.
The STM sub-molecular resolution of the assembled systems requires ultra-flat conductive substrates like High Orderiented Pyrolitic Graphite (HOPG) and Au(111). While the HOPG is mainly used for basic studies on the assembly and electronic properties of functional molecules on solid substrate, gold substrates is also technologically relevant as it is currently employed in microelectronic.

Furthermore, Au(111) surfaces are of particular interest as model surfaces for the chemisorption of molecules exposing sulfur end-group. This strong Au-S interaction allows for the binding of different molecular systems showing high stability and high degree of order in lateral packing. Fig. 3.2 shows the Au(111) surface which is characterized by the typical herringbone reconstruction and dislocation defects[i].

[i] Reconstruction indicates the reorganization process that involves the surface atoms, act to reduce the surface tension.

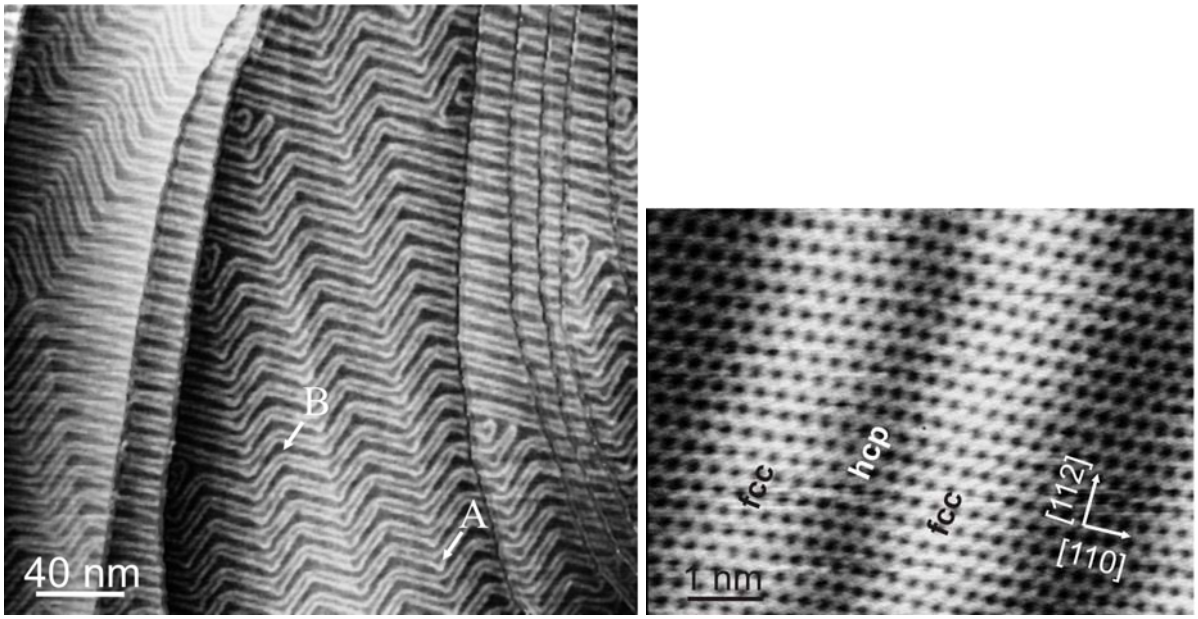

A) **B)**

Figure 3.2: STM images showing the herringbone reconstructed Au(111) surface. **A)** Alternating fcc and hcp stacking domains, as well as x- and y-type elbows are visible. **B)** Atomically resolved STM image revealing the slightly distorted hexagonal arrangement of the surface atoms together with the domain walls separating fcc and hcp stacking. The interatomic distances along [112] and [110] are 2.88Å and 2.75Å, respectively. (**ipn2.epfl.ch/LSEN/jvb/collection/coll_au111.htm**)

The rearrangement of the last atomic layer of Au(111) is unique for close packed surfaces. To reduce the surface tension, surface atoms contract the interatomic distance along the [110] direction from the bulk value of 2.89 Å to an average value of 2.75 Å. This anisotropic contraction is due to the fact that 23 gold atoms of the surface layer are arranged over 22 bulk lattice sites in this direction, leading to a $23\times\sqrt{3}$ overlayer structure and the creation of alternating domains of hexagonal close packed (hcp) and face centered cubic (fcc) stacking (see Fig. 3.3).

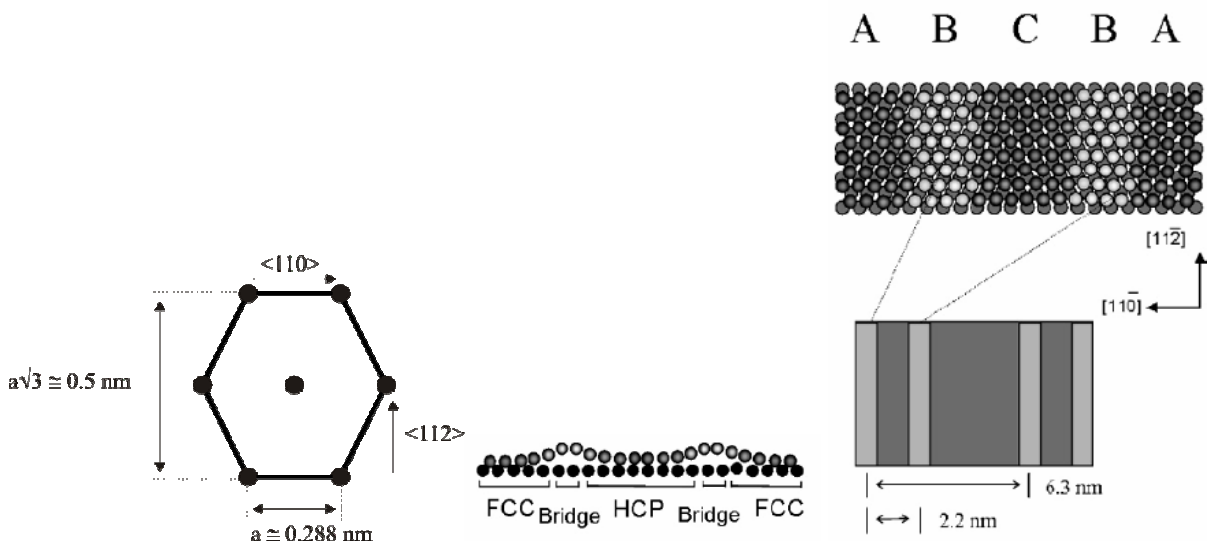

Figure 3.3: a) Unit cell parameters of a gold (111) plane without reconstruction. **b)** Lateral and **c)** top view reconstruction of the (23×√3) Au(111) surface: AC, indicates the fcc reconstruction which is alternated on the surface with hcp domains (B).[4]

The direction of the boundaries along the [112] direction is periodically rotated by 120°, forming the characteristic herringbone pattern. The elbows of the zig-zag shaped features exhibit two different appearances which are characterized by a broader hcp or fcc region in the turning point, denoted by A and B, respectively in Fig.3.2-A. Chambliss co-workers [5] proposed that the sharper edge of the A-type elbow is due to a point dislocation which leads to higher protruding atoms.

The (111) surface crystal structure contains the higher density of atoms on surface therefore it is more stable than the (110) or the (100) surfaces. The influence of the reconstruction on the adsorption of atoms and molecules on Au(111) is demonstrated for different systems which preferably nucleate at the elbows and often assemble as commensurate patterning with the herringbone structure.[6]

Anyway upon adsorption of sulfur containing compound a strong reorganization of the crystalline Au(111) reconstruction is induced and the typical herringbone pattern is no more present.[7]

3.3.1.2 Au(111) preparation procedures

Au(111) surfaces have been prepared by using different approaches namely: template striped gold and flame annealed gold substrates.

3.3.1.3 Preparation of Template stripped gold

Template stripped gold has been prepared following the procedure reported in detail by Semenza and co-workers.[8, 9] The preparation of template stripped-gold on mica is summarized in the scheme presented in Fig. 3.4. The mica has been chosen as deposition substrates because it is a crystalline natural product that easily gives highly crystalline surface terraces by cleavage. Gold atoms epitaxially grow on the flat mica substrate with a hexagonal compact arrangement which produce to the crystalline Au(111) surface structure.[10]

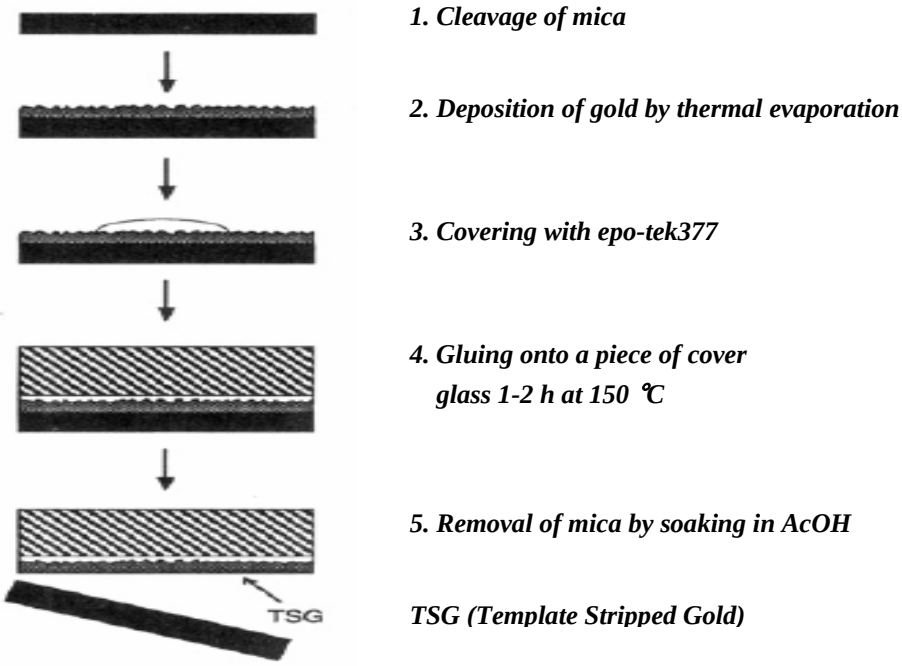

Figure 3.4: Template Stripped-Gold preparation scheme.

We followed two different procedures to obtain an atomically flat gold. In a first attempt we evaporated 200 nm of Au on mica heated at 300°C (Fig. 3.5-a). In a second try we firstly evaporated 15 nm of gold. Then this first thin gold film was annealed at 300° for at

least 6 hours. Finally we evaporated further 185 nm of gold (Fig. 3.5-b). In both cases the mica was degassed at 300°C for 2 days.

a) 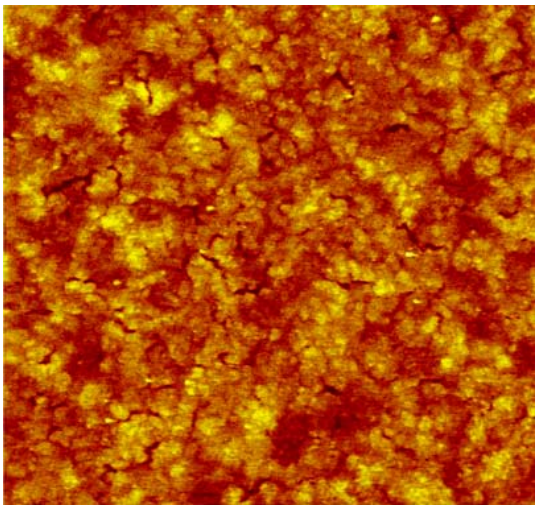 **b)** 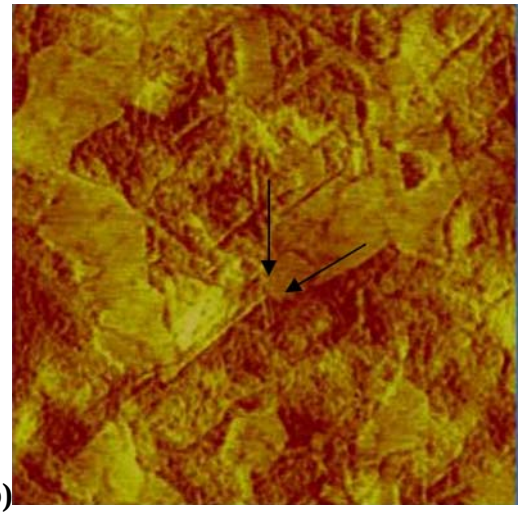

Figure 3.5: Atomic Force Microscopy images of template stripped gold prepared according two different procedures: **a)** (3x3)μm^2: 200 nm of gold evaporated on mica at 300°; **b)** (1.5x1.5)μm^2: 15 nm of gold evaporated on mica annealed at 300° followed by further evaporation of gold until reaching of a nominal thickness of 200nm; crystalline terraces of Au(111) are visible (see arrows).

The AFM images in Fig. 3.5 show that the annealing treatment is a viable approach to produce ultra-flat Au film. While the first film is very smooth, the second one also shows typical crystalline domains with mutual 60° sharp boundaries (see black arrows). Prolonged annealing at 350°C, improves the gold crystallinity. We also found that the thermal annealing of thicker or thinner gold layer, namely 10 and 30 nm thick, does not produce high crystalline surfaces.[11]

Although we could obtain crystalline Au(111) terraces, the presence of the epoxy paste gluing the gold substrate to a solid (usually glass) support, limits the use of those substrates in a variety of solvent, namely the epoxy glue is soluble in chlorinated solvents like chloroform and dichloromethane. For this reason we optimized a second procedure for the preparation of crystalline Au(111) surfaces, which is presented in the next paragraph.

3.3.1.3 Flame annealed gold substrates

Thin films of Ag and Au have been sublimed onto freshly cleaved mica discs in high vacuum at a chamber pressure of ~ 10^{-5} - 10^{-7} mbar and a deposition rate of 0.01nm/s. Before the evaporation the mica substrates were annealed for at least 5 hours at 450°, during the evaporation the temperature is kept at 450° to favor the surface diffusion and crystallization. At this stage gold/mica substrate is kept in a desiccator until its use. Before the immersion of the gold substrate in the target solution an annealing process is required. The annealing is executed by lighting a butane flame on the gold surface, the high temperature reached by the gold substrate allow for the crystallization of the surface and few nanometers wide Au(111) terraces can be observed. The exposition time of the substrate under the flame is trivial as for very high temperature evaporation of the gold can be induced and/or diffusion of mica component through the gold layer can occur. A good indication of the right temperature reached on the gold substrate for the crystallization is the red luminescence, observable by eyes, indicating that the substrate is at around 450°, this temperature is high enough to allow crystallization but is not high enough to induce gold evaporation or interlayer diffusion of the mica component. Au(111) evaporated on mica substrate has been also kindly provided by Professor Jean-Pierre Bucher (Université Louis Pasteur, Strasbourg). Because of their flatness and crystallinity, flame annealed gold has been mainly used for STM studies.

3.3.2 High Ordered Pyrolitic Graphite (HOPG)

A typical conductive substrate used for STM investigations is Highly Oriented Pyrolitic Graphite (HOPG) (Fig. 3.6) which is a layered substrate that can be freshly prepared by cleaving its surface with an adhesive tape. There are two most important features in the structure and electronic properties of graphite: a two-dimensional (2D) layered structure and an amphoteric feature. The basic unit of graphite, called graphene is an extreme state of condensate aromatic hydrocarbons with an infinite in plane-dimension, in which an infinite number of benzene hexagon rings are condensed to form a 2D extended electronic structure. The trigonal bonding in each graphene sheet involves overlap of carbon sp^2 hybridized orbital in plane, whereas the overlap of carbon $2p_z$ orbitals produces delocalized rings of π electrons

lying above and below each benzene ring, which makes graphite a good electrical conductor. Graphite thus features a 2D system from both structural and electronic aspect.

The AB stacking of graphene sheets gives graphite (Fig. 3.6), in which the weak inter-sheet interaction modifies the electronic structure into a semi-metallic one having a quasi-2D nature, as shown in Fig. 3.6-b. The graphene layers are bonded to each other by weak van der Waals forces, so that they can easily slide over one another, which is why graphite is soft and slippery. In contrast diamond, the second most common allotropic form of carbon, is composed of a tetrahedral network of covalently-bonded carbon atoms, where the single covalent bonds are formed by the overlap of sp^3 hybridized orbitals on each carbon atom.

The amphoteric properties arise from the fact that graphite can act either as an oxidizer or a reducer in chemical reactions. This characteristic stems from the zero-gap semiconductor type or semi-metallic electronic structure, in which the ionization potential and the electron affinity have the same value of 4.6 eV.[12, 13]

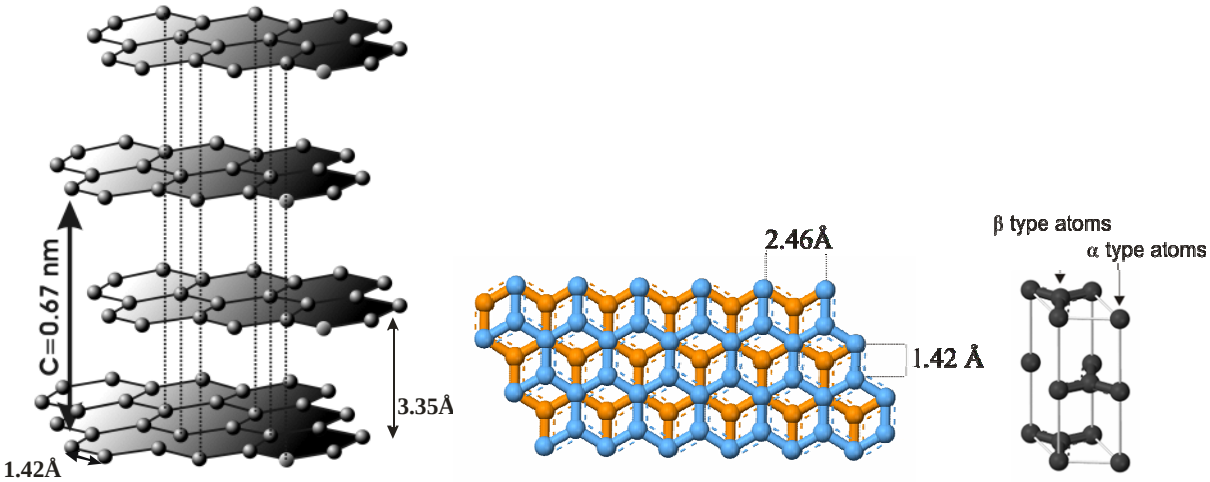

Figure 3.6: HOPG crystallographic structure: **a), c)** Over-layered Graphene sheets; **b)** α and β atoms type, α type atoms are supposed to be the only atoms visible in STM images of graphite surfaces.

HOPG is often used as substrate for STM imaging because of its conductive nature and its easy preparation by cleavage to prepare a fresh conductive surface.
This flat surface is neutral, hydrophobic and inert to organic solvents. Therefore it should be ideal for the self-assembly of either neutral or ionic adsorbates, since electrostatic interactions can be neglected.

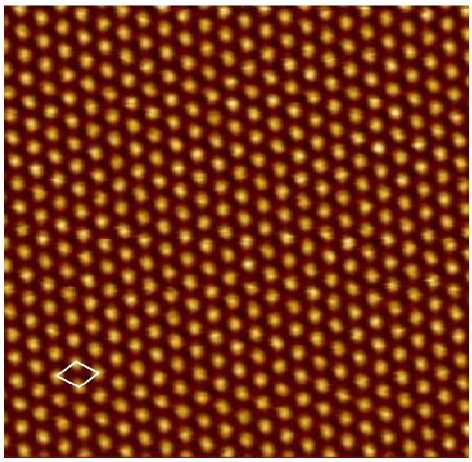

Figure 3.7: STM current image of HOPG. The unit cell is also shown: a=0.246 nm. The image has been corrected for thermal drift with SPIP software. (I_t= 60pA; V=20mV)

Fig. 3.7 displays an STM current image of HOPG with atomic scale resolution. A periodic hexagonal pattern with lateral spacing of 0.246 nm is observed. The lateral spacing between carbon atoms in the hexagonally structured graphene sheet however amounts to 0.142 nm only. Thus in the STM images only every second carbon atom or the center of the hexagons in the graphene sheet are effectively resolved. This has been explained by the non-equivalence of the carbon atoms in a graphene layer with respect to their spatial position above the underlying graphene sheet due to the A-B- type stacking in graphite (see α and β type atoms in Fig. 3.6-c). Alternatively it was suggested that the tunneling probability in the center of the hexagons of the graphene sheets is largest and therefore giving rise to a larger tunneling current.

3.4 Self-Assembled Monolayer preparation

All samples have been prepared by incubation of the gold electrodes or the Au(111) substrates in a solution containing a thiolated derivatives for at least 1 night or more (see scheme in Fig. 3.8). All the solutions have been degassed with N_2 before incubation.
After removal from the incubating solutions the substrates have been rinsed with solvent and dried under N_2 stream after washing.[14, 15]

Details about the specific sample preparation will be provided at the end of each chapter.

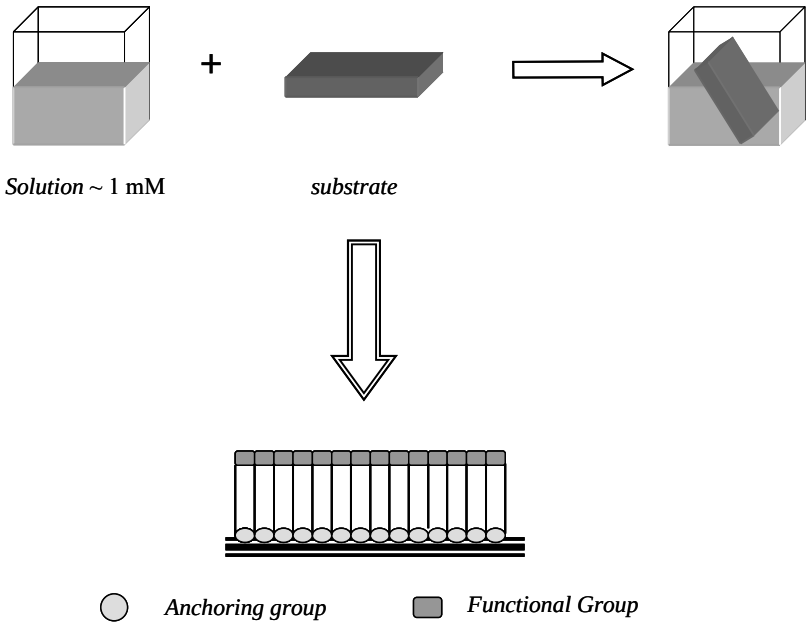

Figure 3.8: Schematic representation of SAMs preparation.

References

[1] D. M. Cyr, Venkataraman, B., Flynn, G.W., *Chemistry of Materials* **1996**, *8*, 1600.

[2] W. Mamdouh, H. Uji-i, J. S. Ladislaw, A. E. Dulcey, V. Percec, F. C. De Schryver, S. De Feyter, *Journal of the American Chemical Society* **2006**, *128*, 317.

[3] S. De Feyter, F. C. De Schryver, *Journal of Physical Chemistry B* **2005**, *109*, 4290.

[4] V. Arima, E. Fabiano, R. I. R. Blyth, F. Della Sala, F. Matino, J. Thompson, R. Cingolani, R. Rinaldi, *J. Am. Chem. Soc.* **2004**, *126*, 16951.

[5] D. D. Chambliss, R. J. Wilson, S. Chiang, *Physical Review Letters* **1991**, *66*, 1721.

[6] S. Clair, S. Pons, A. P. Seitsonen, H. Brune, K. Kern, J. V. Barth, *Journal of Physical Chemistry B* **2004**, *108*, 14585.

[7] M. M. Biener, J. Biener, C. M. Friend, *Langmuir* **2005**, *21*, 1668.

[8] P. Wagner, M. Hegner, H.-J. Guentherodt, S. G., **1995**, *11*, 3867.

[9] M. Hegner, P. Wagner, G. Semenza, *Surface Science* **1993**, *291*, 39.

[10] H. Ibach, *Surface Science Reports* **1997**, *29*, 195.

[11] M. H. Dishner, M. M. Ivey, S. Gorer, J. C. Hemminger, F. J. Feher, *Journal of Vacuum Science & Technology a-Vacuum Surfaces and Films* **1998**, *16*, 3295.

[12] B. T. Kelly, *Applied Surface Publisher, London* **1981**.

[13] W.-T. Pong, C. Durkan, *Journal of Physics D: Applied Physics* **2005**, *38*, R329.

[14] F. Schreiber, *Progress in Surface Science* **2000**, *65*, 151.

[15] J. C. Love, L. A. Estroff, J. K. Kriebel, R. G. Nuzzo, G. M. Whitesides, *Chemical Reviews* **2005**, *105*, 1103.

CHAPTER 4

ISOMERIZATION OF AZOBENZENE CHEMISORBED IN A MONO-COMPONENT SAM

4.1 Introduction

Inspired by the complex molecular machines found in nature, chemists have developed much simpler molecular motors. Single molecules can be functional, i.e. they can be designed to store information and to perform pre-programmed actions, thereby to act as a machine.[1-4] Nature exploits to a great extent light energy as energy inputs because it is environmental friendly and everlasting. Photochromic systems can convert light energy into mechanical energy, thus they can be employed as building blocks for the fabrication of prototypes of molecular devices based on the photomechanical effect[5-10]. Hitherto a controlled photochromic switch on surfaces has been achieved either on isolated chromophores or within assemblies of randomly arranged molecules. Among them, several systems incorporating azobenzene have been proposed, which exploit the reversible *trans-cis* isomerization triggered by light[11] or electric field[12, 13] for applications such as optical data storage devices,[14-16] switchable supramolecular cavities and sensors[17] and light-powered molecular machines delivering mechanical work[18, 19]. Recently, theoretical calculations have also proven the potential of (single) azo-molecules to operate as switching element in molecular electronic devices.[20-22]

Here we show, by Scanning Tunneling Microscopy imaging, the photochemical isomerization of a new terminally thiolated azobiphenyl rigid rod molecule. Interestingly, the isomerization of entire molecular 2D crystalline domains is observed, which is ruled by the interactions between nearest neighbours. This first observation of azo-benzene based system

displaying collective isomerization might be of interest for applications in high density data storage.

4.1.2 Azobenzenes at surfaces

Among photochromic molecules, azobenzenes have been extensively studied for their unique photoisomerization.[23] The transition from the thermodynamically more stable *trans* to the *cis* conformation can be induced by irradiation with UV light and reversed upon heating or irradiation with visible light.[24] The isomerization occurs at the N=N double bond yielding two different states, identified by the *trans(E)*- and the *cis(Z)*-isomer. Such photochemical *trans* ⇆ *cis* isomerization of azobenzene was first described by Krollpfeiffer and co-workers,[25] and it has been thoroughly studied in the last decades.[26, 27] While the solution properties are well-established, a poor investigation on densely packed molecular assembly at surfaces of isomerizable molecules has been performed. The main difficulty arises from the tight packing achieved in some molecular assemblies which hinders the spatial relaxation of the isomerizing molecule. The reversible switching of azobenzene derivatives has already been investigated at room temperature on the single molecule level by Scanning Tunneling Microscopy (STM) experiments in ultra-high vacuum studies on isolated molecules packed parallel to the basal plane of the substrate,[28-30] in physisorbed monolayers at the solid-liquid interface,[31, 32] on SAMs chemisorbed on Au nanoparticles[33] and as co-adsorbate in a chemisorbed alkyl thiolated SAM on solid flat substrates.[34] On the other hand, conformationally flexible alkylthiols exposing azobenzene head-groups forming single component SAMs have been reported being either *non or poorly* responsive to light excitation[35-38]. Moreover, similarly to the case of Langmuir-Blodgett films incorporating azobenzenes,[14, 39, 40] the photo-induced isomerization has not been thoroughly characterized down to the nanoscale in order to provide unambiguous evidence for its occurrence in ambient conditions, and no explanation has been given regarding the conformational reorganization within the SAM after the isomerization. In LB-films, a strategy to reduce the tightness of the molecular packing is to lower the surface pressure used to form the film, i.e preparing a more loosely packed film, allows the development of photo-switchable surfaces.[40, 41] Isomerization has been shown to occur for aromatic azo-compounds on the single molecule level by Scanning Tunneling Microscopy (STM),[28, 30] but in these reports the molecules were not self-assembled into tightly packed films, but

rather individually physisorbed on the metal surface in a flat geometry. In order to overcome the problem related to the steric hindrance arising from the tight packing in SAMs, photoisomerization was indeed accomplished in the past by "diluting" the function, i.e. by incorporating the azobenzene containing molecule in a shorter alkanethiol SAM matrix.[34] Unfortunately, in this latter case, neither a precise structural picture of the conformation of the azobenzene molecules in the hosting SAM before and after the switch, nor a high level of understanding of the structural reorganization of the hosting domain upon interconversion of the guest molecules could be achieved. In addition, it was not possible to unambiguously ascribe the azobenzene isomerization to neither a single nor a few molecules adsorbed at defect sites. This is indeed due to the fact that the photoinduced interconversion of single molecules of both azobenzenes[34] and other photochromic systems, e.g. diarylethenes,[42] chemisorbed in a hosting alkanethiol monolayer was observed only for molecules adsorbed at domain boundaries. In such locations the molecules are weakly anchored to the substrate and loosely packed, and therefore less stable, thus more subjected to fluctuations.

Another approach relies on the self-assembly of asymmetrical disulfides, which upon adsorption on the gold surface split into the azo-molecule and a shorter spacer molecule.[43-45] Unfortunately, alongside the required synthetic effort, phase segregation is most likely to occur when two components are chemisorbed on the surface. Azo-molecules forming self-assembled architectures featuring enough free volume due to the incorporation of bulky subunits have also been described.[46] Finally, photo-isomerization of azo-molecules was found to occur in SAMs on Si(111) taking advantage of the loosely packed character of SAMs on silicon surfaces.[47]

We designed a fully conjugated oligomer (AZO1, see chemical formula in Figure 4.1) adapt to chemisorb on Au(111) surfaces into a single-component SAM, with a packing motif similar to that of arenethiols.[48] We showed that this packing potentially enables, even molecules arranged in the densely packed and crystalline architecture to undergo isomerization. To further assess the assembly properties of these new fully conjugated azobenzene derivatives, in addition to the described compound AZO1, we designed a related aromatic azo-compound AZO2 (Figure 4.1). All the compounds described in this chapter have been synthesized in the laboratory of Professor Marcel Mayor in Basel (Switzerland), by Dr. Mark Elbing.

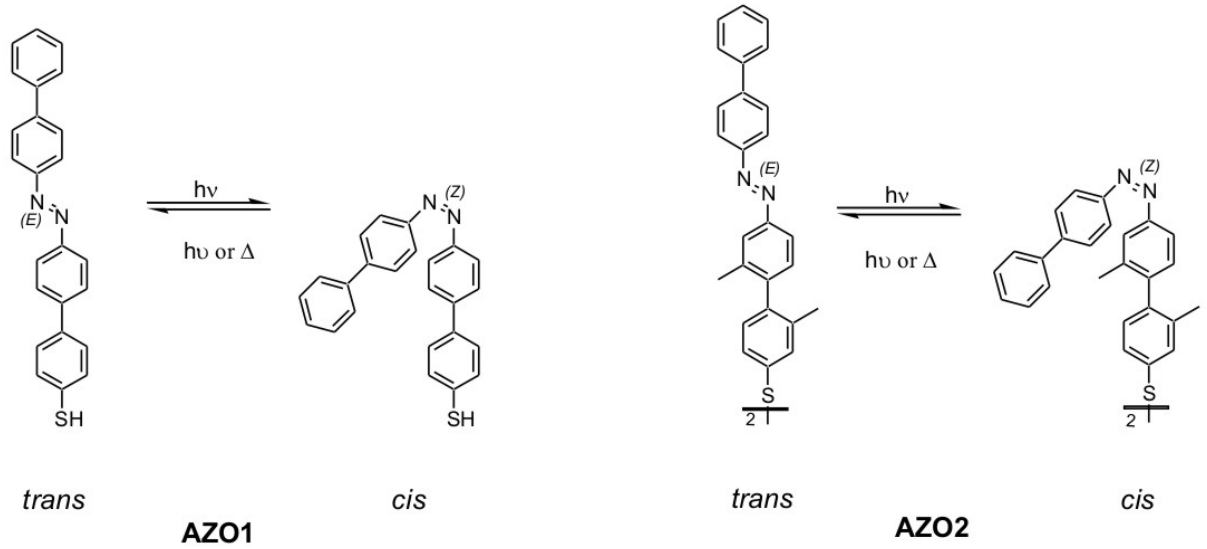

Figure 4.1: Molecular structure of AZO1 and AZO2. Due to the azo-functionality both structures are photo-switchable and due to the sulfur anchor-group both structures are able to form self-assembled monolayers on gold and platinum surfaces.

Due to their sulfur anchor-group both molecular rods can chemisorb on Au(111) surfaces forming single-component SAMs. In AZO1, apart from the sulfur anchor-group the azo-functionality bears on both sides an unsubstituted biphenyl building block. Hence, in a densely packed crystalline SAM this molecule is expected to adopt an almost planar conformation, in fact due to strong electron delocalization the dihedral rotation of both rings is negligible as proven by the x-ray diffraction measurements of a molecular analogue crystal (see Appendix to the chapter 4). Therefore, SAMs formed by AZO1 are supposed to be tightly packed similarly to arenethiols.[49-52] In AZO2 the same upper biphenyl moiety as for AZO1 has been used, but the other biphenyl unit bearing the sulfur anchor-group has additional methyl-substituents in 2 and 2'-positions. The methyl groups can be expected to induce sterical hindrance in this moiety, thereby increasing the dihedral rotation upon molecular assembly.[50] Consequently, π-π intermolecular interactions can be expected to be reduced compared to AZO1 giving SAMs of AZO2 featuring a more loosely packed structure.

AZO1 and AZO2 have been tailored in order to possess a high conformational rigidity which differs from more conformationally flexible thiolated azobenzenes bearing aliphatic units. In fact SAMs of arenethiols differ from those of alkanethiols for the rigid character of the molecular components. The π-conjugated backbone is responsible for T-shaped

interactions among the π-states that give rise to the herringbone structure characterizing SAMs of arenethiols.[53, 54] In aromatic SAMs the π-π intermolecular interactions are mostly responsible for the geometry of the two-dimensional packing on the Au(111) surface, whereas in alkanethiol SAMs such geometry is primarily governed by the sulphur headgroup-substrate interaction together with van der Waals interactions among adjacent alkane chains (see chapter 1). Finally, AZO1 due to its similar structure to arenethiols, can be expected to enable a tight packing at the supramolecular level originated by π-π intermolecular interactions. In this chapter we describe the nanoscale resolved *trans* ⇆*cis* isomerization of AZO1 and AZO2 occurring at surfaces by means of Scanning Tunneling Microscopy (STM) imaging and UV-Vis spectroscopy. Such spatially resolved mapping allowed gaining insight into the isomerization mechanism and yield.

4.2 Characterization of Self-assembled Monolayers (SAMs)

The isomerization of AZO1 and AZO2 in solution has been fully characterized by UV absorption spectroscopy. This work has been carried out by the group of Professor Maria Anita Rampi in Ferrara (section 4.4). They also provided UV results for the isomerization of the two molecules in a single component SAM on Gold and Platinum substrates (see Appendix 4 for further details). Given the interesting results of the photochemical studies on SAMs of AZO1 and AZO2 the self-assembly behavior of both compounds on gold surfaces has been carefully analyzed by using a variety of techniques including synchrotron-based photoelectron spectroscopy (XPS), near-edge absorption fine-structure (NEXAFS) spectroscopy, cyclic voltammetry (CV) and scanning tunneling microscopy (STM). These investigations were performed to gain detailed insight into the structure of these systems and to fully understand the observed photo-chemical behavior based on the structural characteristics of both target compounds. XPS and NEXAFS studies have been performed by the group of Professor Zharnikov in Heidelberg[i].

[i] More details on XPS and NEXAFS will be found in the paper "Single Component Self-Assembled Monolayers of Aromatic Azo-biphenyl: Structure and Light Induced Molecular Movements", by Mark Elbing, Alfred Blaszczyk, Violetta Ferri, Christian Grave, Giuseppina Pace, Andrei Shaporenko, Carsten von Hänsich, Marcel Mayor, Paolo Samorì, Maria Anita Rampi, Michael Zharnikov to be submitted for JACS journal.

4.2.1 Cyclic Voltammetry (CV) measurements

The tightness of the packing of SAMs can be studied by investigating the diffusion capability of a reversible redox-active species (e.g. $K_3[Fe(CN)_6]$) through the SAMs. The redox species can permeate the organic SAM when it is loosely packed, leading to the occurrence of a redox process at the electrode surface.[55] Then, both cathodic and anodic currents arising from reaction (I) are observed in the cyclic voltammogram.

$$Fe^{3+} + e^- \rightleftharpoons Fe^{2+} \qquad (I)$$

CV measurement on SAMs made with either AZO1 or AZO2 is represented in Figure 4.2. For the sake of comparison, data recorded on SAMs of undecanethiol, which are known to be tightly packed, as well as on bare gold electrodes are shown. In films of undecanethiol permeation of the redox species through the monolayer toward the gold surface is prevented and CV curves are essentially flat (curve d, black line). In contrast, measurements on a bare gold electrode clearly show oxidation and reduction peaks (curve a, red line). SAMs comprising the AZO1 molecular rod hardly show cathodic or anodic currents (curve c, blue line) and resemble CV curves obtained for undecanethiol suggesting a well packed assembly. In contrast, CV curves of SAMs formed by AZO2 (curve b, green line) clearly show the occurrence of the Fe^{2+}/Fe^{3+} redox reaction indicating the high permeability of the SAM. This provides unambiguous evidence that SAMs of AZO2 are more loosely packed than SAMs of AZO1 chemisorbed on the polycrystalline gold electrode. Structural defects arising from the loose packing of the AZO2 film represent favorable sites for the diffusion of the Fe^{2+}/Fe^{3+} species.

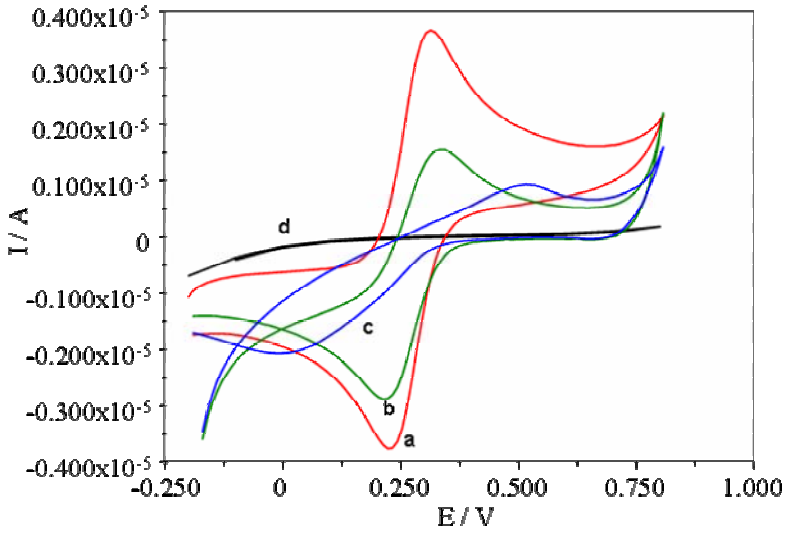

Figure 4.2: Cyclic Voltammetry plots: a) bare gold electrode (curve a, red line); b) SAM of AZO2 (curve b, green line); c) SAM of AZO1 (curve c, blue line); d) SAM of undecanethiol (curve d, black line). The measurements were carried under the following conditions: $K_3Fe(CN)_6$ 1mM, KCl 1M, scan rate 50mV/s.

Absorption-desorption experiments (see section 2.2) show that both target compounds chemisorb on Au via their sulfur anchor-groups (Fig. 4.3).[56-59]

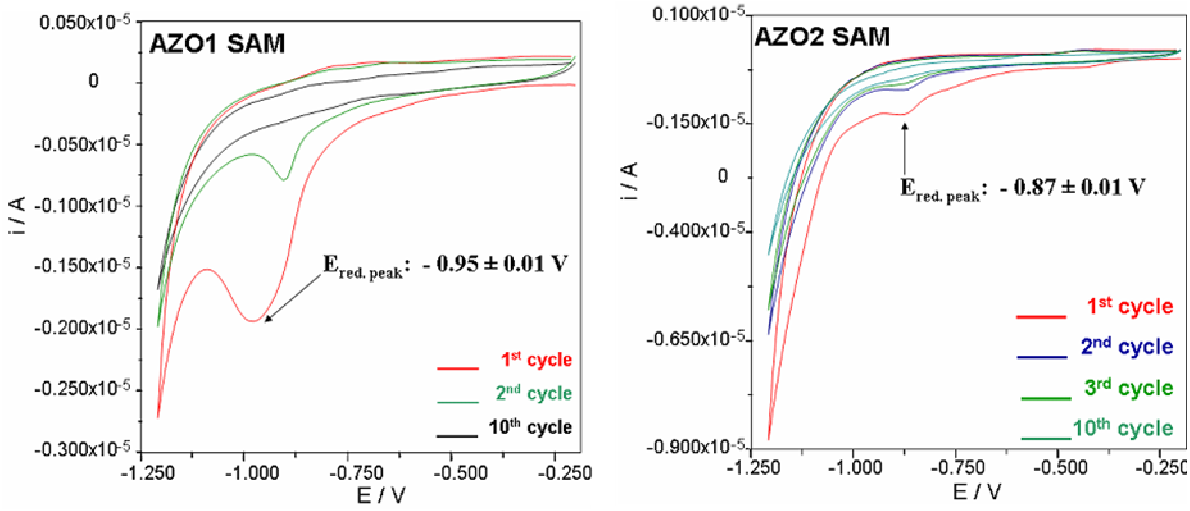

(A) **(B)**

Figure 4.3: Cyclic Voltammetry plots: **A)** SAM of AZO1; **B)** SAM of AZO2. The measurements were done under N_2 atmosphere and 0.5 M KOH, scan rate 100mV/s.

The voltammetric curve of SAMs of AZO1 displays a sharper desorption peak compared to AZO2 SAMs shifted toward more negative reductive potential values. This provides clear evidence for a more homogeneous character of the chemical environment around the binding sites of AZO1 than of AZO2. Therefore, the AZO1 SAM is more tightly packed and has a higher orientational order compared to the AZO2 monolayer. Most likely, stronger intermolecular interactions between the aromatic subunits of AZO1 with respect to AZO2 cause the more homogeneous packing in SAMs of AZO1. The lower stability of SAMs of AZO2 can be attributed to the steric hindrance introduced by the two methyl groups reducing lateral interchain interactions.

The combined results of the CV studies confirm that AZO1 forms better ordered SAMs than AZO2, a result which is in excellent agreement with the XPS and NEXAFS results obtained by the group of Professor Zharnikov.

4.3 STM measurements

It is typically more difficult to achieve high-resolution STM images of arenethiols on Au(111), if compared to alkanethiols SAMs, due to the relatively smaller size of the domains and higher density of structural defects. While the formation of a commensurate domain of alkanethiol on Au(111) having ($\sqrt{3} \times \sqrt{3}$)R30° unit cell is primarily governed by the gold-sulphur interaction, in arenethiol SAMs the π-π interchain interactions control the assembly leading to the formation of a herringbone structure.[48, 60-63]

Alongside, arenethiols pack more perpendicularly with respect to the substrate, which leads to optimization of intermolecular interactions. Different lattice parameters have been reported for SAMs of alkylthiols substituted with azobenzene head-groups.[64-66] These unit cells exhibit a rectangular geometry and contain two molecules. Importantly, the rectangular lattices of alkylthiols with azobenzene head-groups have been found to resemble the unit cells of SAMs of arenethiols on Au(111) suggesting that the packing is mainly governed by π-π interactions between the aromatic moieties. However, it is still a matter of debate if the arenethiol SAM packing leads to a commensurate molecular lattice[67-69] or not.[52, 70, 71] The strong interchain interactions among adjacent molecules have been typically thought to be responsible for an incommensurate lattice[72] of the arenethiols SAMs on gold, although recently the herringbone structure has been attributed to a commensurate lattice[72]. Since in

general it is difficult to resolve the atomic structure of the gold surface underlying the SAMs, we cannot define how the Au(111) surface reconstruct upon the molecular self-assembly.

SAMs formed by trans isomers have been prepared under careful exclusion of light therefore, from molecules predominantly in their *trans* conformation. While STM current images of SAMs of AZO1 chemisorbed on Au(111) show well ordered molecular domains (Fig. 4.4), a good molecular resolution for SAMs of target compound AZO2 could not be achieved. This result is consistent with the previous observations, as the lack in STM resolution is consistent with a disordered monolayer in SAMs of AZO2.

For target compound AZO1 a densely packed monolayer consisting of highly oriented domains up to 20 nm wide has been found.

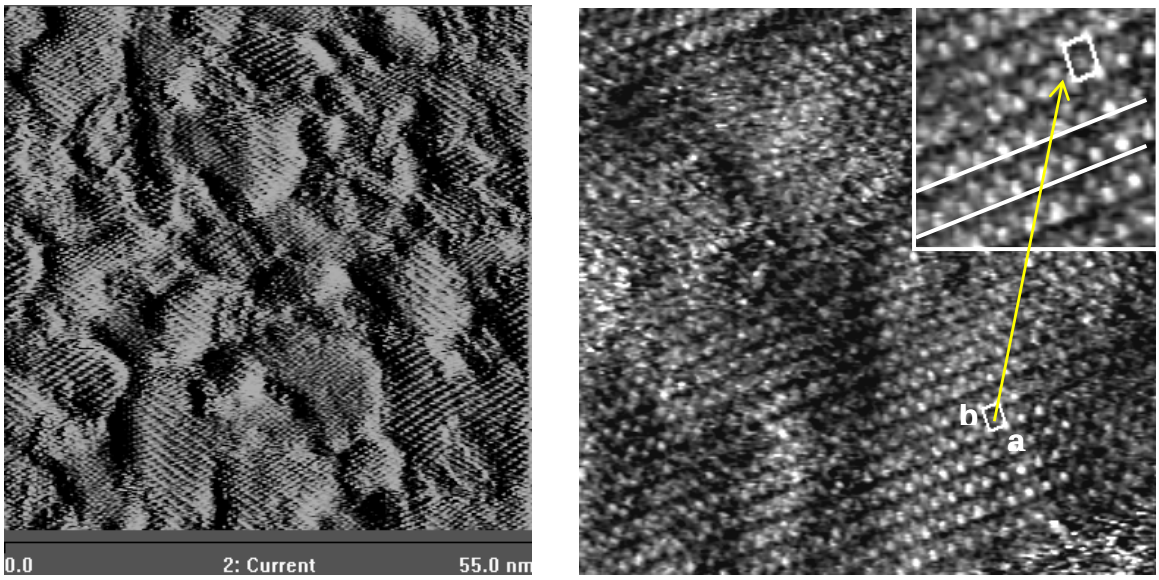

(A) **(B)**

Figure 4.4: A-B) Constant-current STM image of *trans*-AZO SAM on Au(111). **B)** Rectangular unit cell containing two molecules: a= (0.65±0.05)nm , b= (0.89±0.05)nm and α= (84±5) °. Similar unit cell was reported for arenethiols SAMs on Au(111). Imaging parameters: average tunnelling current, I_t = 55 pA; bias voltage, V_t = 150mV.

The STM image in Fig. 4.4 shows a monocrystalline domain: each bright spot represents a single molecule adopting the *trans* conformation the unit cell, whose lattice parameters are: a= (0.65 ± 0.05)nm , b= (0.89 ± 0.05)nm and α = (84° ± 5°), contains two molecules. Such packing is in very good agreement with that of arenethiol SAMs[62] and azobenzene alkylthiolated molecules chemisorbed on Au(111).[35, 71] In such crystalline

motif the molecules pack more perpendicularly to the Au(111) surface if compared to alkanethiol SAMs, an evidence that has been proven by XPS and NEXAFS studies, from which a tilt angle of 20° has been calculated[ii] (a schematic drawing of the tilt angle is presented in Fig. 4.5).

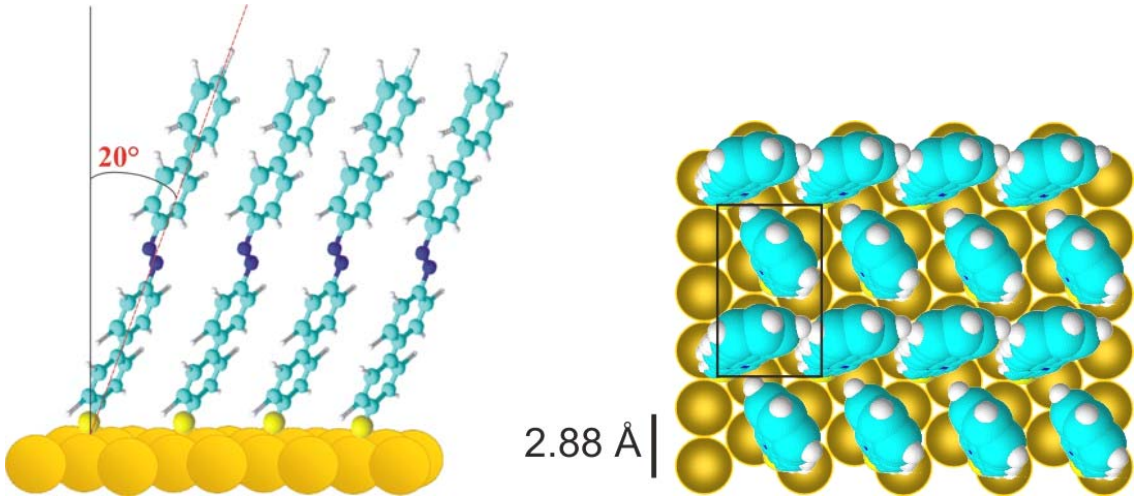

(A) **(B)**

Figure 4.5: A) Molecular sketch illustrating the molecular tilt angle as found from XPS and NEXAFS studies. **B)** Molecular sketch of a commensurate AZO molecular lattice.

Similarly to arenethiol SAMs the *trans*-AZO1 molecular lattice exhibits parallel stripes of dimeric molecules displaying a herringbone motif. The angle between the bright stripes of different domains amounts to 60 ± 5° reflecting the three-fold symmetry of the underlying Au(111) surface (Fig. 4.4-A). The domains are also separated by so-called "etch pits"[73] marked by black arrows in Fig. 4.6.[iii] Moreover, the formation of islands of gold adatoms (indicated by white arrows in Fig. 4.6) demonstrates a strong reconstruction of the gold surface. The domains formed on these small islands of adatoms are oriented along the same directions as the domains appearing on the underlying gold terrace suggesting the growth of a

[ii] The tilt angle indicates the angle formed between the molecular axe and the normal to the basal plane of the surface.

[iii] Etch pits (or holes) are well known features in SAMs of simple alkanethiols. They are caused by the relaxation of the Au(111) surface reconstruction upon adsorption of the thiol group.

commensurate lattice on the reconstructed gold substrate, as illustrated in the molecular sketch in Fig. 4.5-B.[iv]

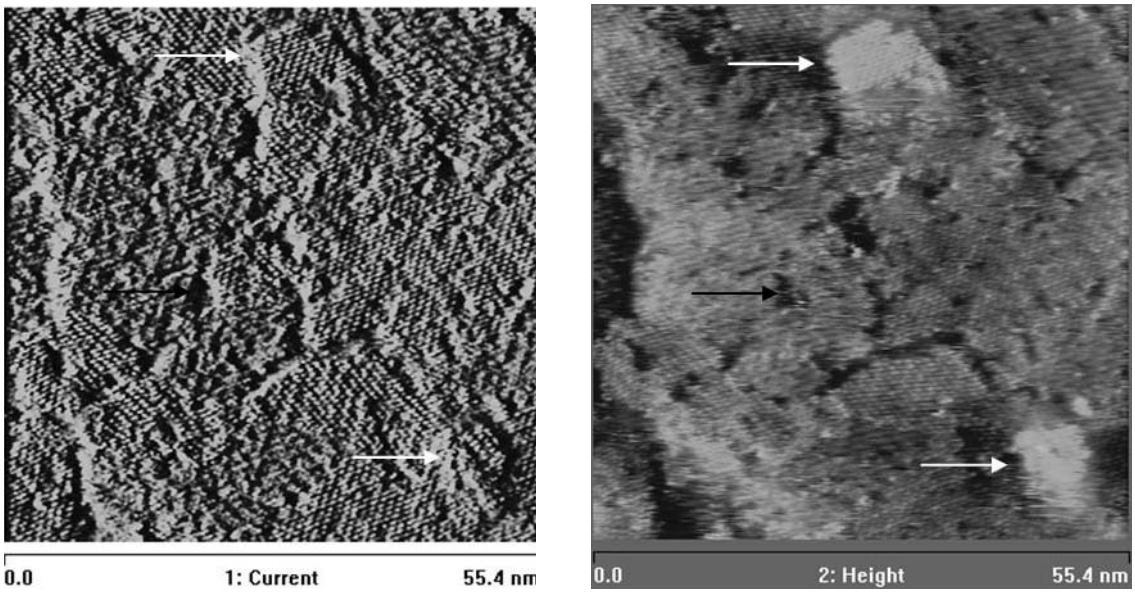

Figure 4.6: STM image showing high-resolution images of the monolayer of AZO1 on Au(111). Left: current-contrast image; right: height-contrast image. Black arrows indicate pits and white arrows indicate islands of adatoms. Average Tunneling Current, I_t = 5.0 pA; Bias voltage, V_t = 260 mV.

In previous STM studies of SAMs of alkylthiols with azobenzene headgroups on Au(111) two types of domains with different tunneling contrast have been found, i.e. an herringbone and a pseudo-hexagonal lattice.[71] While both domains possess identical unit cell parameters and contain two molecules, the second spot was found to locate either at the center of the unit cell or displaced towards one of the corners of the cell giving rise to a pseudo-hexagonal or a herringbone lattice, respectively. (It is worth to remind that each spot corresponds to one molecule.) According to the explanation given in previous works, those domains have the same unit cell but differ on the molecular arrangement within the cell.

[iv] Previous studies , using scanning tunneling microscopy (STM), have shown that SAMs derived from arenethiols form an ordered structure on Au(111) surfaces, with the lattice constants of *a*= (5.2 ± 0.4) Å *b*= (9.7 ± 0.9) Å and α= 55° ± 5°. Among many possible models that are consistent with the measured lattice constants, a simple commensurate structure (√3× 2√3)R30° was previously proposed, which has the lattice constants *a*= 4.99 Å and *b*= 9.98 Å and α= 60°.

Consistently, we observed that under variation of the scan angle the pseudo-hexagonal lattice appear as the rectangular one and vice-versa.

For AZO1 we observed the same two types of domains e.g., domains marked with A in Fig. 4.7 show a herringbone structure with the same unit cell and image contrast as the *trans* domains in Fig. 4.4-B, while domain B in Fig. 4.7-B show a pseudo-hexagonal lattice. The pictures differ only in the scan angle, all the others scan parameters are kept constant. Significantly, upon rotation of the scan angle used during the image acquisition domain A displays a pseudo-hexagonal lattice (domain A in Figure 4.7-A and after rotation ($\Delta\theta_{b\text{-}a}$= 90°) in Figure 4.7-C). Another example of such scan angle effect is represented by the pseudo-hexagonal domain B found in Fig. 4.7-B which after rotation of the scan angle to $\Delta\theta_{b\text{-}d}$= +15° appear in Figure 4.7-D with a herringbone contrast. Therefore, the observed lattice structure seems to depend on the scan angle used to record the image; therefore only one molecular lattice exists.

The herringbone and pseudo-hexagonal cell has been observed for images recorded at 90° and -15°, 0° respectively. Similar behavior has been found simultaneously for domains B and A, which feature different crystalline orientations therefore, imaging artifacts can be ruled out. At the same time, tip induced processes can be excluded, as the contrast variation has been found either using asymmetric (prepared by mechanical cut) and symmetric STM tips (fabricated by chemical etching). Another example for such an effect is showed in Fig. 4.8.

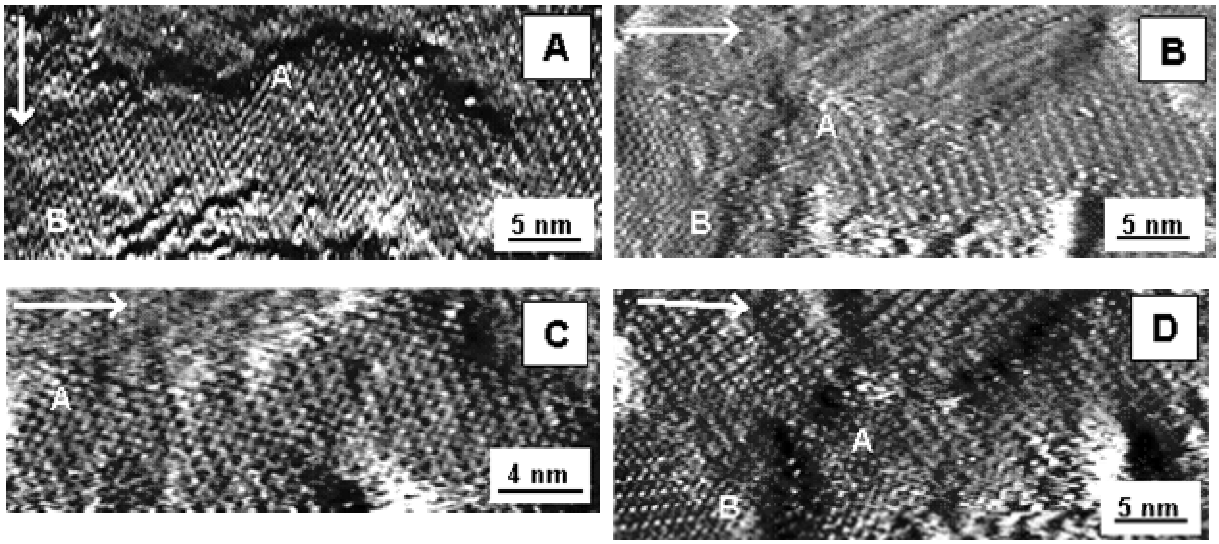

Figure 4.7: Constant-current images of SAM of AZO1. **A)** Image of the initial scan; **B)** Image obtained on the same area as for A), but after scan angle rotation of 90° (clockwise rotation); **C)** Zoom on domain A in Fig. 4.7-B; **D)** Image obtained on the same area as for B), but after scan angle rotation of 15° (anticlockwise rotation). Average Tunneling Current, I_t = 5.0 pA; Bias voltage, V_t = 260 mV.

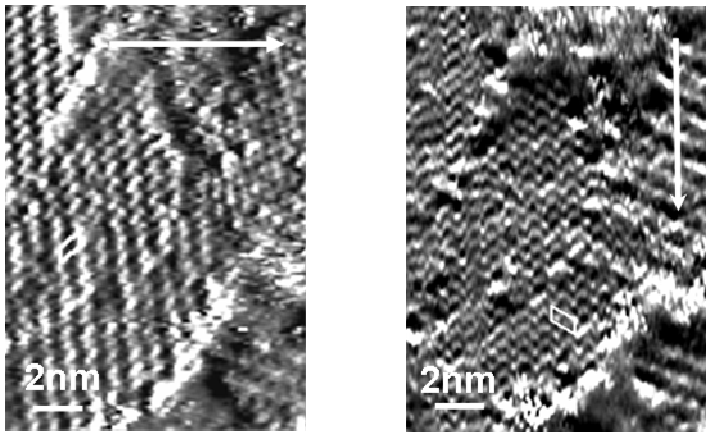

Figure 4.8: STM image of AZO1 AZO1 monolayer on Au(111). White arrows indicate the scan direction. Left: herringbone like unit cell: a= (0.60 ± 0.05) nm; b= (1.0 ± 0.05) nm: Right: pseudo-hexagonal like unit cell same area after 90° rotation of the scan angle: a= (0.60 ± 0.05) nm; b= (1.1 ± 0.05) nm.

The contrast variation was found to be completely reversible upon reverse scan angle rotation[71] hence, the presence of two non-equivalent Au-S binding sites can be neglected. The influence of the molecular conformation on the tunneling is known to lead to the c(4×2)

superlattice in alkanethiols SAMs. Alkanethiols bind the gold substrate according to the $(\sqrt{3}\times\sqrt{3})$R30° commensurate lattice, and the unit cell reflects the Au-S binding site geometry. According to the bundle model, the conformational relaxation of the alkane chain in the SAM determines the twisting of the upper methyl head-group of only one molecule in the unit cell. This leads to the c(4×2) superlattice, where brighter spots appear together with darker spots, and it is believed that there is no change of the binding site during this relaxation process.[73] Our contrast variation cannot be explained in terms of a difference in the chain conformation of the two molecules in the unit cell, because of the high rigidity of the AZO1 backbone.

Our explanation of the observed scan angle effect relies on the contribution of the symmetry of the molecular orbital the tunneling process. In fact, beside the tip-sample distance, the geometry and symmetry of the molecular orbitals should be considered to interpret the image contrast in STM measurements. We believe that the image contrast variation observed depends on the different overlap between the tip apex density of states and the molecular orbitals when changing the tip-scan direction.

Since alkyl chain posses a cylindrical shape, the molecular orbital are symmetric with respect to the tip apex density of states, thus such an effect has not been observed for *n*-alkanethiols SAMs. The two Azo1 molecules contained in the unit cell are not arranged face to face but rather in a T-shaped arrangement, as showed by the presence of the herringbone structure; therefore the orientation of their molecular orbitals is not equivalent with respect to the scanning tip. The Azo1 molecules can be described as rigid plates; the geometry and symmetry of their molecular orbitals determining the observed scan angle effect.

Those considerations are to some extent consistent with previous measurements performed with Atomic Force Microscopy.[65] In those studies lattice parameters similar to ours have been found. Given that AFM provides a topographical map of a surface, the different contrast reported in this previous work can only be due to the orientation of the upper phenyl ring of the arenethiols. According to Heckl and co-workers,[74] who observed a similar scan angle effect in STM imaging on monolayer of the nucleic acid base, adenine, adsorbed on molybdenum disulfide (MoS_2). They stated that the scan angle effect can be caused by the dependence of the polarizability of the molecular bonds on the scan angle, which is induced by the electric field of the tip.

In view of the above arguments, we suggest that the observed scan angle effect can be attributed to the influence of the symmetry of the molecular orbitals contributing to tunneling, because given the herringbone arrangement the orientation of the molecular orbitals of the two AZO1 molecules in the unit cell differs with respect to the scanning tip. This is a quite interesting result as it provides subtle insight into the contribution of molecular orbitals to the tunneling. Therefore STM contrast in SAMs imaging is not merely caused by the density of electronic states localized at the Au-S bond.[75]

4.4 Photoisomerization of AZO's SAMs

4.4.1 Photochemical Studies

Photochemical investigations in solution as well as studies of SAMs chemisorbed on metal surfaces provide insight into the isomerization behavior of these azo-compounds, which further corroborate the STM results. All the UV spectra showed in this paragraph have been kindly provided by Dr. Violetta Ferri (University of Ferrara, Italy)

The *trans*- and *cis*-isomers of azo-compounds feature different UV-Vis spectra. While the spectrum of the *trans*-isomers shows an intense π-π*-transition band around λ= 350 nm and a weaker (forbidden) n-π*-band around λ= 450 nm, the spectrum of the *cis*-isomer is characterized by a more intense n-π*-transition band around λ= 450 nm.[24] Irradiation of the *trans*-isomer induces a *trans*→*cis* photoisomerization reaching a photostationary state. The back *cis*→*trans* isomerization can occur both via a thermal reaction, because the *trans*-isomer is thermodynamically more stable, or via a photoinduced isomerization by irradiation of the n-π* absorption band of the *cis* isomer. Photochemical studies in chloroform solutions revealed that our molecule represents an optically addressable molecular switch which can undergo *trans* ⇆ *cis* photoisomerization, as monitored by UV-vis spectroscopy. Fig. 4.9 shows the UV-Vis spectral changes of AZO2 (and AZO1) in chloroform solution occurring under irradiation of an initially pure *trans*-isomer at its maximum absorption wavelength of λ=360 nm (AZO1: λ=370 nm).

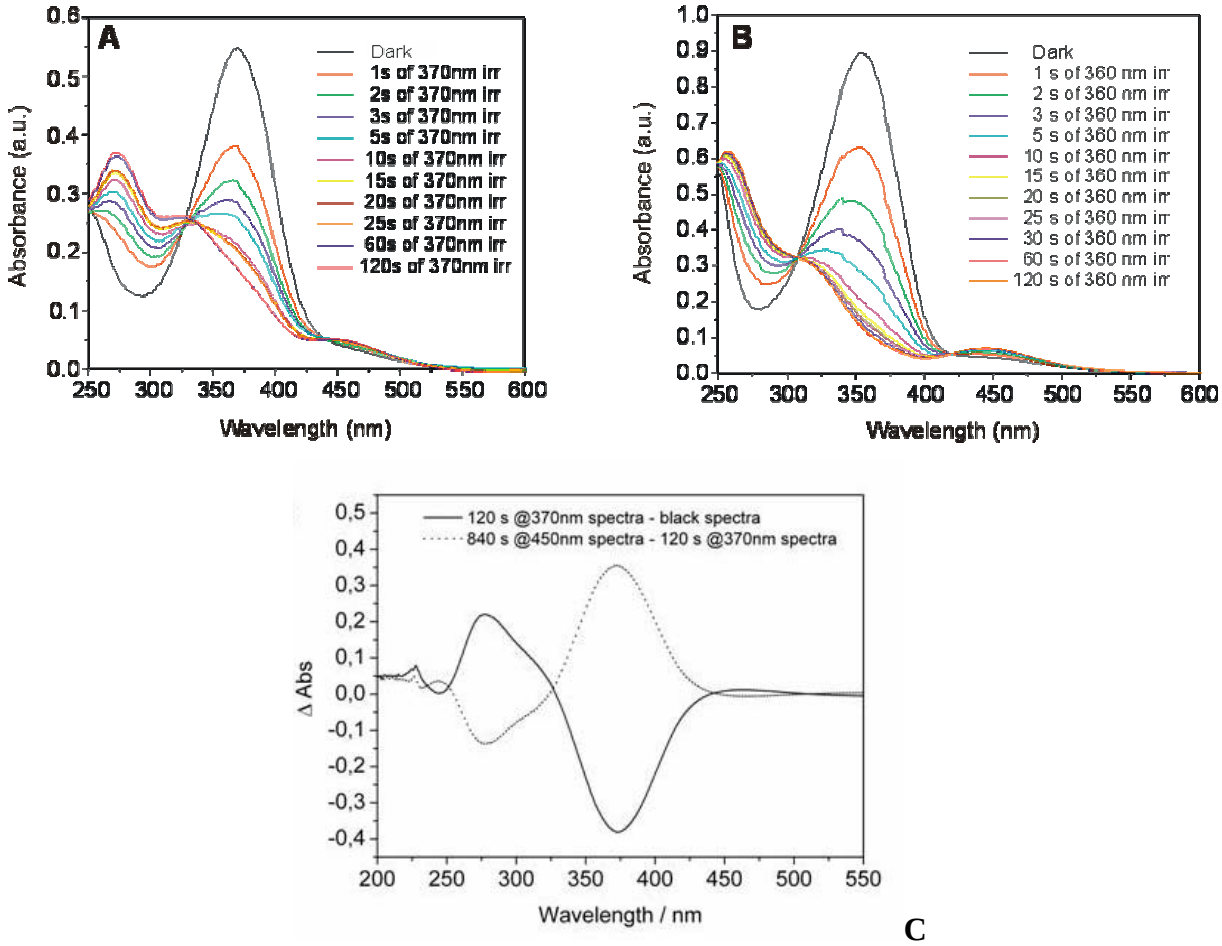

Figure 4.9: Time evolution of the UV-Vis absorption spectrum in solution: **A)** the *trans*-isomer of AZO1 irradiated at λ = 370 nm up to 120 sec in chloroform solution; **B)** the *trans*-isomer of AZO2 irradiated at λ = 360 nm up to 120 sec in chloroform solution. **C)** UV/Vis spectral changes upon photoisomerization of AZO1 in chloroform solution.

^{1}H-NMR studies in solution upon light irradiation provided evidence for the formation of a photostationary state with a *trans*→*cis* conversion of 88% for AZO1 (and 89% for AZO2) and a back thermal isomerization characterized by a first order reaction with a rate constant $\mathbf{k_{AZO1/sol}}$ = (8.5± 0.30)•10 $^{-4}$ sec $^{-1}$ (and $\mathbf{k_{AZO2/sol}}$ = (1.19±0.09)•10 $^{-4}$ sec $^{-1}$ for AZO2, see Appendix to the chapter 4 and Table 4.1).[44]

Optical studies performed in transmission mode revealed spectral changes upon subsequent irradiations at λ=450 nm and λ=360 nm of SAMs chemisorbed both on transparent Pt and Au surfaces as displayed in Fig.4.10-A-C and Fig. 4.10-B-C, respectively. The spectra in Fig. 4.10 unequivocally show the reversible character of the switching process on solid substrates (refer to the Appendix to chapter 4 for more details).

The photo-conversion of the photostationary state within the SAM was calculated to span between 94% and 100% (see Table 4.1 in the appendix to chapter 4). The stability and reversibility of the signal detected during the lifetime of a device is of paramount importance when evaluating the use of an organic compound for molecular device applications. The back thermal reaction on the surface is dominated by a first order kinetic with a rate constant $\mathbf{k_{AZO1/Au}}$ =(2.82±0.14)•10 $^{-4}$ sec^{-1} and $\mathbf{k_{AZO2/Au}}$ =(1.67±010)•10 $^{-4}$ sec^{-1} on gold substrate and $\mathbf{k_{AZO1/Pt}}$ =(2.21±0.05)•10 $^{-4}$ sec^{-1} and $\mathbf{k_{AZO2/Pt}}$ =(1.33±0.06)•10 $^{-4}$ sec^{-1} on platinum substrate. These values indicate clearly that the *cis→trans* thermal reaction is slower when AZO1 is organized in SAMs if compared to AZO1 dissolved in a chloroform solution, probably because of the higher sterical constrain existing in the densely packed monolayer. In fact, due the π-π interactions in SAM the cis form is better stabilized than in solution.

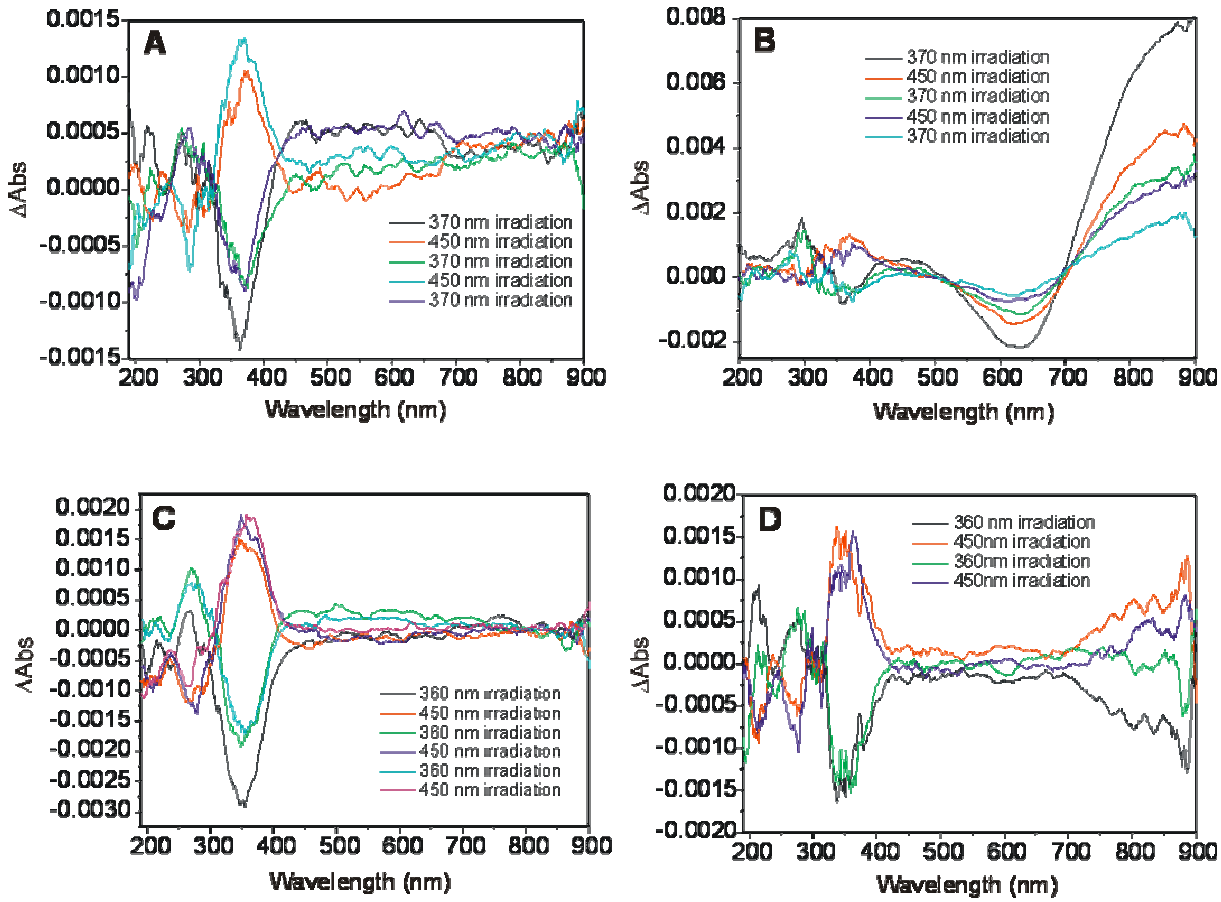

Figure 4.10: Absorption spectra of the reversible switching of SAMs of: **A)** AZO1 on a **Pt** surface; **B)** AZO1 on a **Au** surface; **C)** AZO2 on a **Pt** surface; **D)** AZO2 on a **Au** surface. These are UV-Vis spectral changes occurring upon photoisomerization of AZO1 and AZO2 arranged in SAMs. The SAMs have been switched back and forth between the *trans* and the

cis conformer, by irradiating the AZO2 sample with UV light at 450 nm and 360 nm, and the AZO1 sample at 450nm and 370nm. After each switching process absorption spectrum were recorded. The curves have been obtained by subtracting two sub-sequent absorption spectra.

While the spectral changes recorded on Au surfaces clearly show the Surface Plasmon Bands, these features are not observed in the corresponding spectra on Pt surfaces. Comparison of these spectral changes with those recorded in solution (Fig. 4.9-C) unequivocally provides evidence for the reversible character of the switching process on solid substrates for both molecular rods.

4.4.2 STM studies

STM studies of the chemisorbed monolayer made it possible to investigate the structural and light-induced dynamical properties of AZO1 on Au(111) with a molecular resolution on the trans and *cis* AZO1 SAMs (cartoon in Fig. 4.11). Unfortunately it was not possible to carry on a thorough characterization of the AZO2 SAM because of the lack in ordered molecular packing which avoided getting molecular resolution STM images.

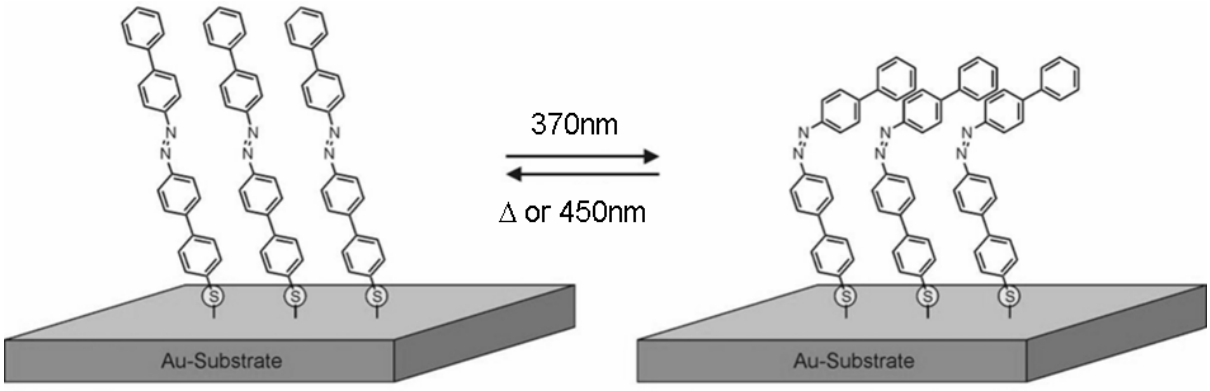

Figure 4.11: Cartoon of the switching molecule on an Au surface. For the sake of example, a small domain of molecule AZO1 (4'-(Biphenyl-4-ylazo)-biphenyl-4-thiol) immobilized on a Au surface have been sketched. Intermolecular interactions between adjacent molecules stabilize the packing of domains consisting exclusively of *trans*-isomers (left) as well as the packing of domains consisting exclusively of *cis*-isomers (right).

A SAM of AZO1 was prepared by incubating the substrate under dark condition overnight and studied at the solid-air interface. The film was then irradiated for 15 minutes at 365 nm, in order to activate the *trans*→*cis* isomerization. Fig. 4.12 and Fig. 4.13 display a STM image recorded 90 min after the irradiation. A single *cis* molecule is marked by the blue oval in Fig. 4.12-B. The upper part of the image exhibits molecules mostly isomerized in the *cis* conformation, whereas the bottom part is mainly dominated by the *trans* conformer.

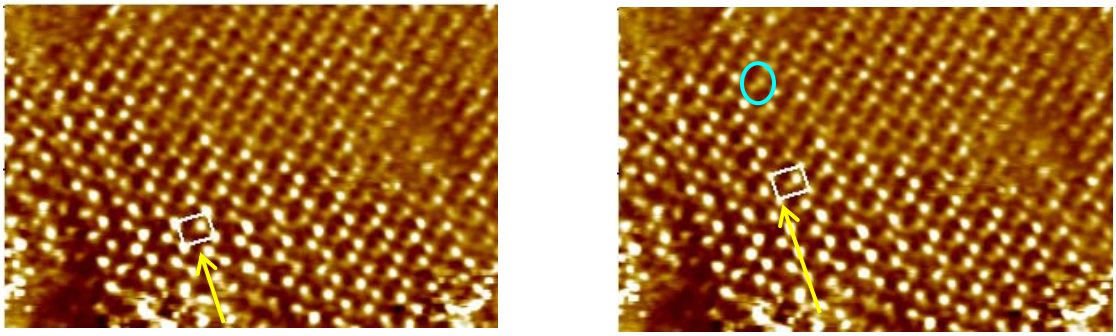

A) **B)**

Figure 4.12: STM current images of a SAM of AZO1 after irradiation at 365 nm. The yellow arrows indicate: **A)** unit cell containing only trans molecules; **B)** unit cell containing at least 1 cis Azo1 molecule. Unit cell parameters: a= (0.62 ± 0.05) nm, b= (0.81 ± 0.05) nm and α = 88° ± 5°.

The *cis* molecule appears in the STM current images as formed by two spots. The two spots were observed to be located in identical positions also upon changing systematically the scan angle and scan rate, as well as on different samples and employing different tips, therefore ruling out any imaging artifact. Moreover the switch was visualized by STM using various tunneling parameters, therefore diverse tunneling gap impedances. Thus, although we can not fully neglect a mechanical or electrical contribution of the tip to the switch, we do believe it does not play a prime role. Although the isomerization occurs over some hundreds adjacent molecules, it is not possible to state if the isomerization can take place over the whole sample surface.

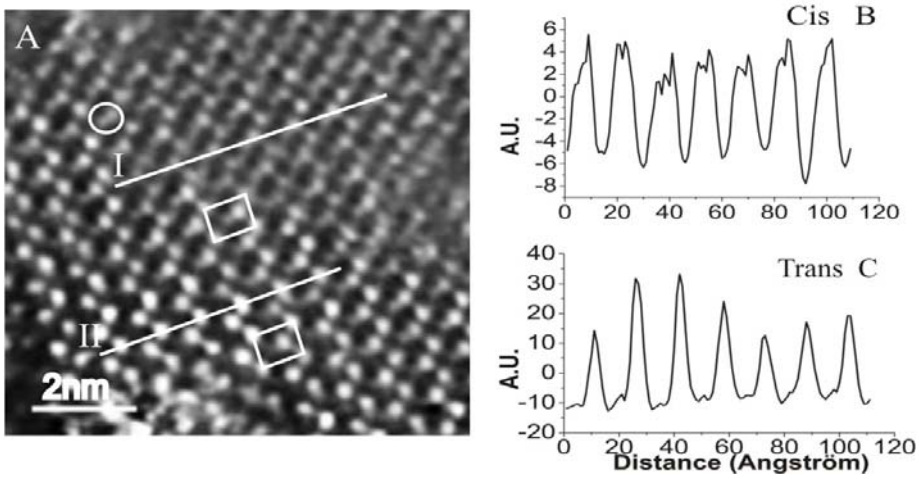

Figure 4.13: Cooperative switching occurring over a single molecular domain. STM image of SAM of AZO1 formed on template stripped Au(111) incubated in the dark for 1 night in $5*10^{-4}$ M solution in toluene (I_T = 49.00 pA; V_T = 145 mV). In the image a single *cis* molecule is marked by the oval. The sample was irradiated for 15 minutes at 365nm before measurements. The image was recorded 90 minutes after the irradiation. This time frame is very small if compared to the two weeks needed to achieve a complete restoration of the *trans* isomer of alkyl-thiolated *cis*-azobenzenes under dark.[76] The bottom unit cell contains the *trans* isomers; the upper unit cell contains *cis* molecules. Line profiles showing: **B)** profile I the *cis* conformer and **C)** profile II the *trans* conformer.

In Fig. 4.13 the profiles I and II are traced across the molecules adopting a *cis* and a *trans* conformation, respectively. Noteworthy, the profiles are traced along the direction of the unit cell main axis, i.e. the direction of the switch.

Both profiles I and II exhibit a constant distance between binding sites which amounts to 8.8Å. However, in profile I each molecule displays two peaks separated by a distance of 2.6 Å, which represents a fingerprint of the *cis* isomer. This value is not directly related to the distances calculated according to the atomic (geometrical) model. In fact the tunneling is governed by the overlap of the tip's density of state with well-defined molecular orbitals containing the contribution of the molecule-substrate interaction. Therefore, the measured distance between the two spots of a *cis* molecule should be explained in terms of the shape of the molecular orbitals contributing to the tunneling and not according to the distances between the atoms or groups. The high electron density at the Au-S bond has been shown to originate a high contrast in STM images allowing the easy identification of the Au-thiols

binding sites.[77] Therefore, we attribute the brighter spot to the straight biphenyl-thiolated side of the aromatic chain.[73] Consequently, the second spot corresponds to the terminal biphenyl side-group of the aromatic chain that is relocated upon isomerization. The isomerization to the *cis* conformation brings the upper biphenyl side of the chain closer to the gold surface. In such a position the biphenyl moiety electronically interacts with the substrate; a tunneling through-space process allows to monitor these moieties by STM. In Fig. 4.13, only a partial coverage of the domain with cis molecules can be observed, it is reasonable to state that either the *trans*→*cis* isomerization was not complete over the entire domain or that a *cis* →*trans* thermal back-isomerization has occurred.

The unit cell parameters found for the *cis* domains, which amount to a= (0.62 ± 0.05) nm, b= (0.81 ± 0.05) nm and α = (88° ± 5°), are identical to those of the *trans* domains, within the experimental error bars. This strongly supports an isomerization mechanism occurring without rearrangements at the Au-sulphur binding sites. Thus only a conformational transition of the aromatic chain takes place, which is presumably accompanied by a change in the molecular tilt angle to compensate the difference in the molecular volume between the *trans* and *cis* conformers. The same lattice parameters of the *cis* unit cell have been found chemisorbing the *cis* conformer on the Au substrate. We also prepared samples by incubating the gold surface overnight in a solution of AZO1 under light irradiation (at 365 nm) and further irradiating for 90 min after removal from the solution (Fig. 4.14). This is relevant as it suggests that both *cis* and *trans* conformers can chemisorb into thermodynamically stable and highly ordered crystalline films. Likewise the *trans* domains, the *cis* domains adopt an herringbone structure, proving that the π-π intermolecular interactions are also responsible for the stability of the *cis* domains. In previous studies *cis* azobenzene derivatives have been physisorbed only flat on Au(111) by a prior irradiation of the azobenzene solutions, but it was not possible to form ordered *cis* domains starting from the *trans* conformers adsorbed on the gold.[78]

Significantly, in Fig. 4.14 it is possible to identify the folding direction of the switching molecules, as indicated by the arrows. Inside a *cis*-unit cell the two molecules isomerize bending the upper biphenyl side in opposite directions. The unidirectional character of the switch occurring on adjacent molecules along the direction of the unit cell main axis, together with the opposite orientation of bending in neighboring rows, is caused by the need to minimize the steric hindrance during the conformational rearrangement. As the *trans* binding

sites seem to be not disturbed by the switching process, we deduce that the intermolecular interactions between the *cis* molecules stabilize the herringbone structure of the new *cis* domain, which is further corroborated by the slow thermal back-isomerization detected for the AZO1 SAMs by UV-Vis absorption measurements.

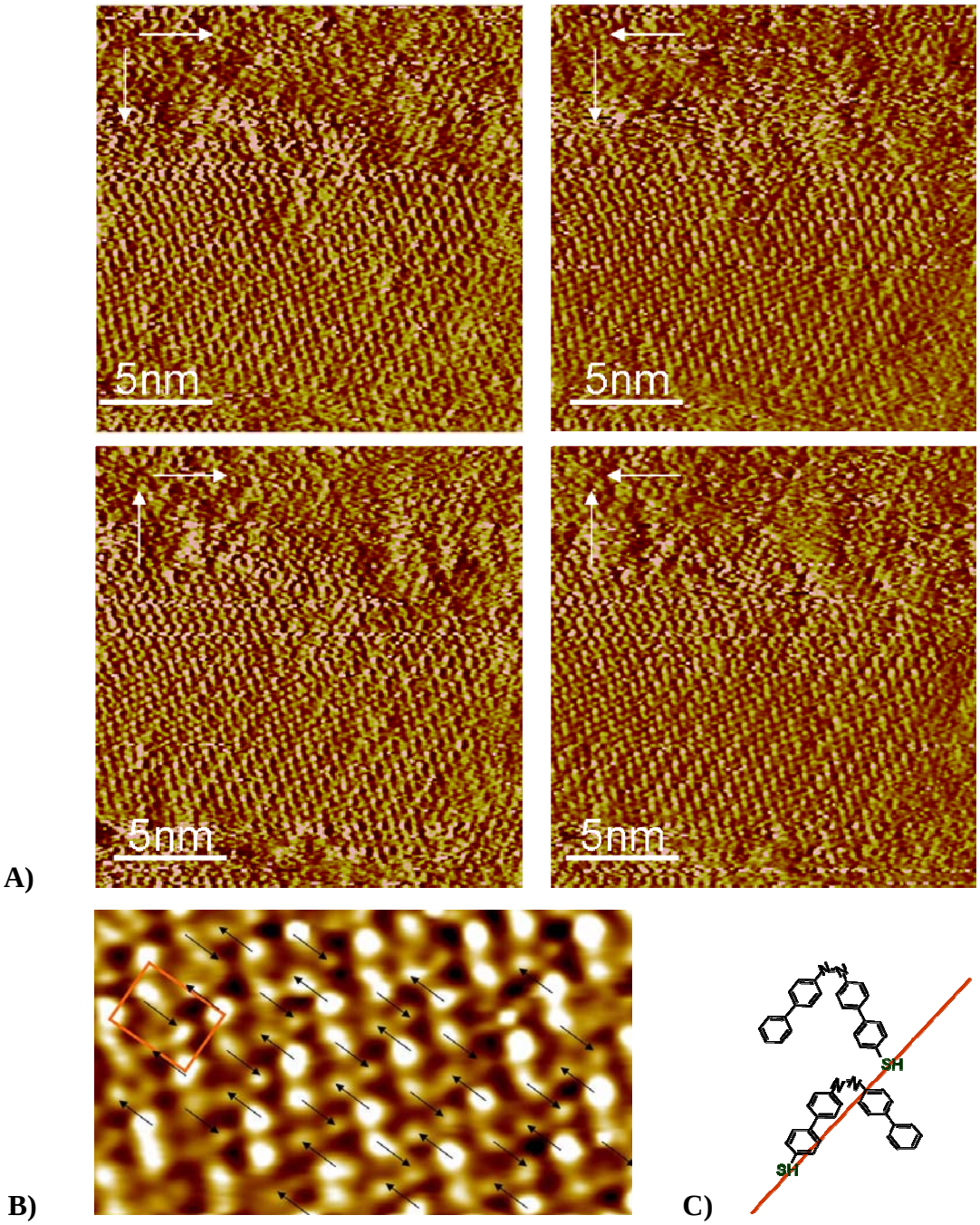

Figure 4.14: STM image showing a *cis* domain of a sample prepared by incubating overnight the Au(111) substrate in a $CHCl_3$ solution of AZO1 under light irradiation at 365 nm. After removal from the incubating solution the sample was further irradiated for 90 minutes before

imaging. The picture has been recorded roughly 30 minutes after irradiation. **A)** Images taken at different scan directions (the white arrows indicate the scan directions). **B)** Cis AZO1 domains: the arrows indicate the folding direction of the each isomerizing molecule in the domain. **C)** Sketch of the cis isomerization folding direction along the main unit cell axes. Imaging parameters: Average Tunneling Current (I_T) = 13.22 pA; Bias voltage (V_T) = 280 mV. Lattice parameters: a= (0.62 ± 0.05) nm, b= (0.81 ± 0.05) nm, α= 92° ± 5°, Area= (0.50±0.1) nm^2.

We showed that the isomerization is extended over many adjacent molecules arranged into a few tens of nanometers wide crystalline domain. The observation of such a long range isomerization means that the yield of conversion upon a domain of the *trans* conformer is nearly 100%, i.e. it is higher than the isomerization yield in solution, as also documented by optical spectroscopy. This long range order can be ascribed to a cooperative process which determines the long range conversion. Upon the initial isomerization of a few molecules, the intermolecular interactions between the *cis*-molecules and the surrounding *trans* isomers are most likely weakened, promoting the isomerization of other adjacent molecules along the unit cell main axis direction, a mechanistic picture that is further supported by the unidirectional character of the bending. The possibility to stabilize the *cis* conformer through the intermolecular interactions among adjacent molecules in a *cis* domain is responsible for the considerably increased yield of the isomerization on the solid substrate with respect to the solution yield. This is confirmed by the value of the kinetic constant calculated for the thermal back *cis*→*trans* reaction on metal surface, which is more than 7 times lower than in solution. We infer that the rigidity of the aromatic backbone is responsible for the cooperative isomerization and the π-π interchain interactions are fundamental for the long lifetime of the *cis* isomer at surface. In fact, upon switching of one molecule the number of accessible conformations (i.e. relaxation states) of the adjacent molecules is limited by the rigidity of the backbone. Such reduced number of conformations that can be adopted to stabilize the *cis* domains favors the occurrence of a cooperative and unidirectional switch. This is the reason why the so far reported systems consisting of bidimensional crystals of alkylthiols exposing azobenzene head-groups[35, 71] did not display comparable switching properties, as both requirements, i.e. rigidity and π–π interchain interactions, were not fulfilled.[79]

4.5 Exploiting the photo-mechanical effect in electronic devices

Recently, it has been demonstrated by Gaub and co-workers that the photoisomerization process of individual polymer chains incorporating azobenzenes can express mechanical work.[20] In light of these findings, one can foresee self-assembled monolayers (SAMs)[80, 81] of aromatic azobenzenes, as those previously described, to act as molecular systems able to express mechanical forces by exploiting a cooperative sub-nanometer structural change. The cooperative nature of the isomerization of adjacent AZO1 molecules in these SAMs suggests them as ideal systems to act as a cargo lifter. To demonstrate and exploit this cooperative effect we have used a metal-molecule-metal junction (Fig. 4.15), based on a Hg top-electrode. In collaboration with Professor Maria Anita Rampi from the University of Ferrara, we have shown that, upon irradiation, AZO1 SAMs incorporated in a junction between a Au(111) surface and a mercury (Hg) drop are able to (i) lift the "heavy" Hg drop against gravity, and (ii) reversibly photoswitch the current flowing through the junction.

Hg was chosen because it is a metal featuring a compliant liquid surface.[82] The junction incorporates the AZO1 SAM chemisorbed on a 10 nm thick transparent Au(111) electrode on a quartz support and a Hg drop coated with a SAM of dodecanethiol as top electrode.

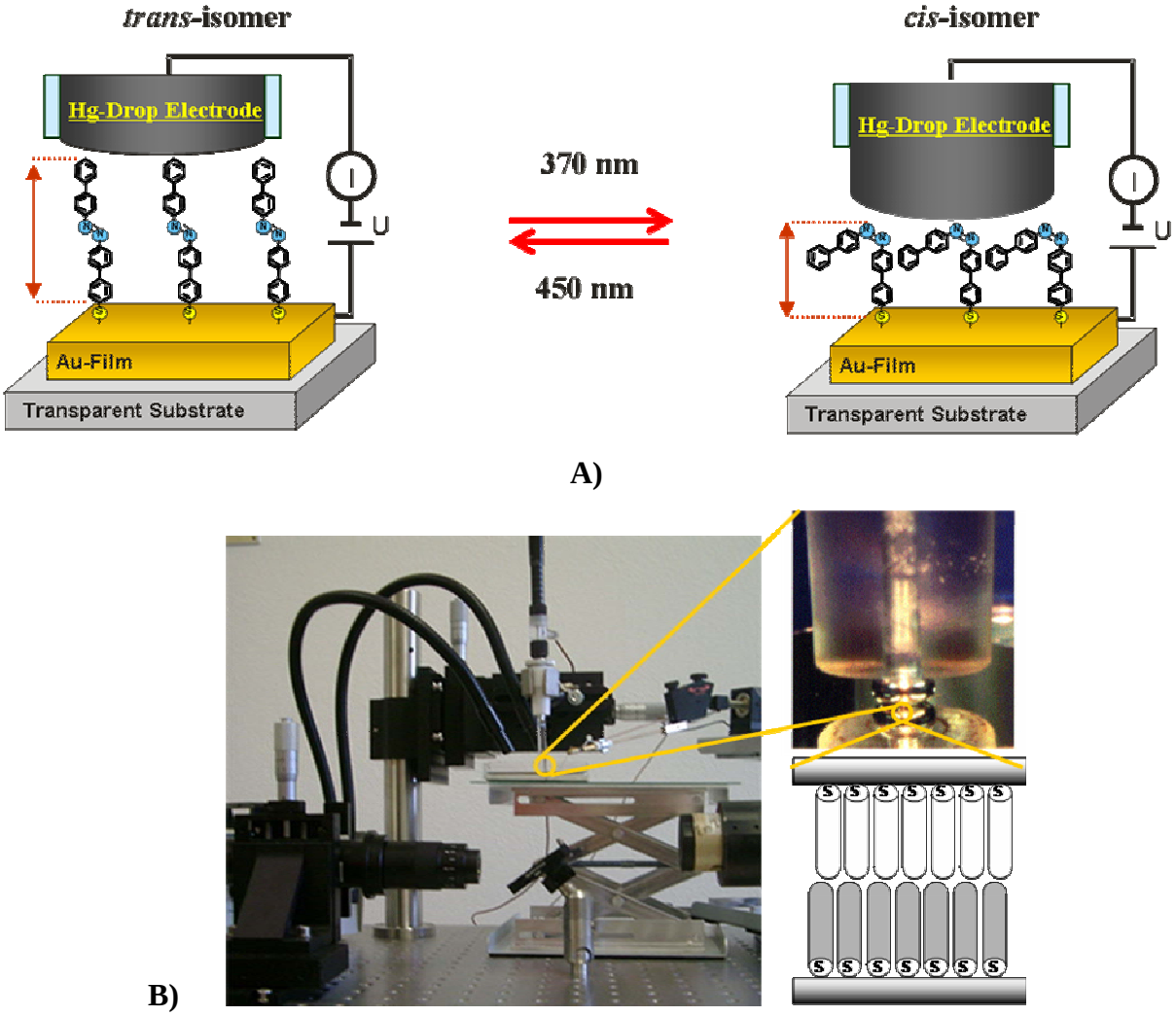

Figure 4.15: A) Sketch of the SAM_{AZO} immobilized between a transparent Au surface and the Hg drop electrode. Due to the light triggered isomerization between the rod-like *trans* isomer (left) and more compact *cis* isomer (right) the distance between both electrodes varies, providing both, an optoelectronic switch and an opto-mechanical "cargo" lifter. **B)** Photographic image of the experimental set-up used to perform the current-voltage measurement in the Au-SAM_{AZO}//SAM_{C12}-Hg junction. B) Image on the right is a magnification photograph of the junction. Image on the left is a schematic illustration of the Au-SAM_{AZO}//SAM_{C12}-Hg junction.

Current-voltage (I-V) characteristics averaged over more than 30 junctions incorporating SAM_{AZO} in the *trans* and in the *cis* conformation are shown in Fig. 4.16-a. The difference in the measured currents, which amounts to about 1.4 orders of magnitude, is in agreement with a through-bond tunnelling mechanism usually described by the equation I =

$I_0\ e^{-\beta\ \Delta d}$.[83] Accordingly the observed current values fit well assuming a comparable decay factor (β=0.5±0.1Å^{-1}) as for polyphenyl chains[82] and a difference in thickness between SAMs containing the *trans* and the *cis* form of about $\Delta d = d_{trans} - d_{cis} \approx 7$Å.

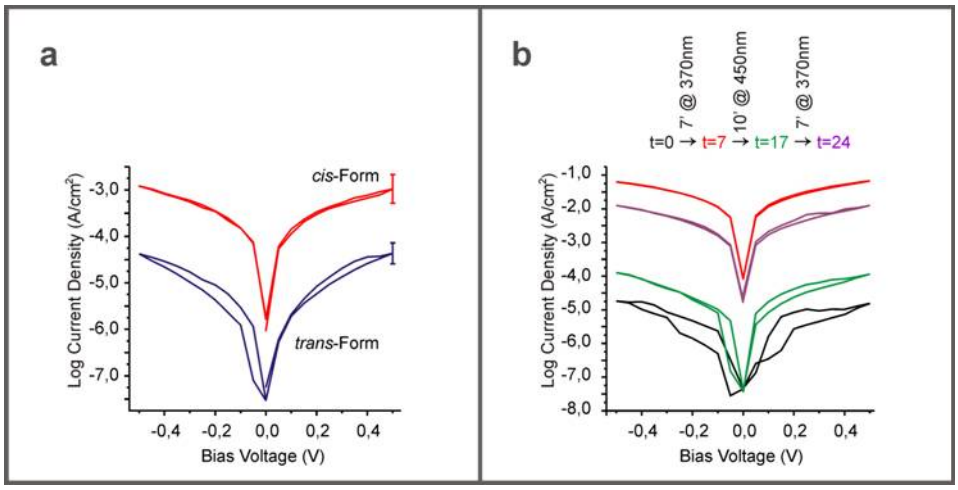

Figure 4.16: Light-induced switching of electrical properties of AZO1 SAM. **a**) I-V curves measured in *ex-situ* junctions Au-SAM_{AZO}//$SAM_{C_{12}}$-Hg incorporating the *trans* (blue lines) and the *cis* isomer (red lines). **b**) I-V curves recorded *in-situ* on a junction Au-SAM_{AZO}//$SAM_{C_{12}}$-Hg incorporating the *trans* isomer subsequently irradiated with alternating wavelengths, λ = 370 nm and 450 nm, as indicated in the picture.

The most significant results were obtained on the SAM_{AZO}-based junctions, upon alternating irradiation *in-situ* of the SAM_{AZO} through the transparent Au surface. As displayed in the I-V curves in Fig. 4.16-b, starting from the SAM_{AZO}-junction in its *trans* conformation, the current density increases and decreases reversibly over one order of magnitude upon alternating irradiation at λ = 370 nm and λ = 450 nm, respectively. The reversible character of the photoinduced current variation provides unambiguous evidence for the stability of the Au(111)-SAM_{AZO}//$SAM_{C_{12}}$-Hg junction. In particular, it rules out both i) an interdigitation of the C_{12}-SAMs exposed on the Hg drop with the SAM_{AZO} chemisorbed on the Au(111) surface, and ii) a considerable lateral displacement of the Hg drop upon light induced extension of the *cis* form. Importantly, similar differences in current were obtained upon *in-situ* (Fig. 4.16-b) and *ex-situ* (Fig. 4.16-a) irradiation. The data of Fig. 4.16 indicate that i) the reversible *cis-trans* photo-conversion exhibits the same high yield both in *in-situ* and *ex-situ* experiments and ii) the SAM_{AZO} is able to keep the electrical contact with the upper C_{12}-

SAM-stabilized Hg electrode upon repeated cycles. A loss of electrical contact would have resulted in a lower current for the *cis* with respect to the *trans* isomer. The switching behaviour can be explained in terms of the SAM_{AZO} reversibly lifting and lowering the Hg drop on top of the SAM_{AZO}. Taking into account the radius of the spherical drop (~1.5 mm) and the density of Hg (13546 kg/m^3), switching the SAM_{AZO} from the *cis* to the *trans* isomer must lift a mass of 1.9×10^{-4} kg a distance of Δd. The total force per area exerted by the Hg on the SAM_{AZO} is 1.0×10^5 N/m^2; this value is calculated based on a simple force balance that accounts for gravitational effects, atmospheric pressure, and surface tension (see SI for details). Assuming that the surface packing density of the SAM_{AZO} is 4.0×10^{18} molecules/m^2 (as obtained from the size of the unit cell of the SAM_{AZO} detected by STM[79]), the average force exerted by the Hg on an individual AZO molecule in the SAM amounts to $F_M = 2.6 \times 10^{-14}$ N. The cooperative forces per unit area generated by the SAM_{AZO}, i.e. at least 1.0×10^5 N/m^2, are sufficiently large enough to lift or displace the Hg drop, and comparison of this force with the one determined by Gaub for each molecule,[20] which amounts to 10^{-12}N, indicates that the system is still far from exploiting its full potential

Our results demonstrate that by harnessing the cooperative nature of the isomerization in adjacent highly rigid AZO molecules, it is possible to photoswitch the current through a molecular junction and to develop a prototypical molecular machine acting as a cargo lifter. These findings pave the way towards the fabrication of a new class of molecular motors expressing forces of unprecedented magnitude, and towards optically switchable nano-electronic circuitry. Therefore the reported azobenzene SAMs hold potential as nanoscale materials for future applications both as light-powered molecular machines performing mechanical work, and as photo-switchable monolayers for nano-electronics, e.g. for diodes and transistors.[84, 85]

4.6 Summary and Conclusions

Two conjugated aromatic azo-compounds AZO1 and AZO2 bearing sulfur anchor-groups to allow self-assembly onto metal surfaces have been synthesized. By design, AZO1 represents an essentially planar, completely rigid molecular rod, as proven by crystal structure analysis. The planar structure results in strong π-π-interactions. Differently, the presence of two methyl-groups on the biphenyl of AZO2 leads to a reduction of

intermolecular π-stacking, as determined by the dihedral angle between the two-phenyl-rings.[49]

While AZO1 forms tightly packed SAMs on Au with a high degree of ordering, AZO2 packs more loosely giving less ordered films, as proven by XPS, NEXAFS, CV and STM investigations. Kinetical studies on AZO2 are reported in the Appendix. Interestingly, the *trans→cis* photo-isomerization and thermal as well as photoinduced back *cis→trans* isomerization were observed for both target compounds AZO1 and AZO2 in solution and organized in SAMs. Even more, the yields of photo-isomerization of AZO1 and AZO2 in SAMs on Au are comparable within the experimental error. In particular for AZO1, a yield of photo-conversion very close to 100% was observed. This important result questions the common beliefe that isomerization in SAMs of azo-compounds can only be achieved efficiently, when a loosely packed monolayer is formed. In fact, a slightly lower yield of photo-isomerization was observed for AZO2, which forms SAMs less densely packed. For AZO2 similar rates for thermal back *cis→trans* isomerization in solution and in SAMs were measured. Presumably, the arrangement of AZO2 in the disordered SAMs resembles the environment in solution. Instead, the tight packing of AZO1 SAM introduce sterical constrain which might slower the back *cis-trans* isomerization with respect to the solution rate.

Furthermore, we have shown that a properly designed azobenzene molecule can undergo *cis-trans* photoisomerization in large domains at surfaces. This switch, which occurs in densely packed single component SAMs without perturbing the molecular lattice, is complete over hundreds of molecules and it exhibits a cooperative character. Such a cooperative process is novel and widely applicable for switchable single component SAMs consisting of intrinsically rigid and tightly packed molecules, given that the mechano-chemical switch is not sterically hindered. The high yield of the *cis-trans* isomerization on metal substrate opens intriguing perspectives for high density data storage devices[84] based on photochromic compounds. This long range photoisomerization taking place on the surface is new, and it was not observed in previous STM studies performed at the solid-liquid interface, since the dynamic exchange between the supernatant solution and the adsorbate did not allow to unambiguously determine if the isomerization was occurring on the surface or in the solution through a sub-sequent desorption and re-adsorption process.[31, 32] This is an ideal system to be implemented in crossbar memories and for the achievement of light driven

logic operations.[86] A monolayer of photoisomerizable molecules embedded in a molecular switch tunnel junction can be used as a data storage element (bit).[84]

4.7 Experimental procedures

For CV studies gold electrodes have been used as a metal substrate, and for STM measurements we employed ultra-flat gold substrates Au(111).

For UV measurements, Pt and Au films with a nominal thickness of 100Å have been prepared on quartz by E-Beam deposition and vacuum sublimation, respectively.

The SAMs were prepared by immersion of the gold substrates into a 0.1-0.5 mM solution of AZO1 (or AZO2) in degassed chloroform or toluene at room temperature for 24-48 h. After immersion, the samples were carefully rinsed with pure chloroform and blown dry with nitrogen.

STM sample where irradiate at 365nm wavelength with a UV Lamp, Bioblock. Unit cells were averaged over several images making use of SPIP software (Scanning Probe Image Processor (SPIP) version 2.0 image metrology ApS, Lyngby, Denmark).

References

[1] V. Balzani, A. Credi, F. M. Raymo, J. F. Stoddart, *Angew. Chem. Int. Ed.* **2000**, *39*, 3349.

[2] F. M. Raymo, *Adv. Mater.* **2002**, *14*, 401.

[3] W. R. Browne, B. L. Feringa, *Nature Nanotechnology* **2006**, *1*, 25.

[4] E. R. Kay, D. A. Leigh, F. Zerbetto, *Angew. Chem. Int. Edit.* **2007**, *46*, 72.

[5] N. Koumura, R. W. J. Zijlstra, R. A. van Delden, N. Harada, B. L. Feringa, *Nature* **1999**, *401*, 152.

[6] A. M. Brouwer, C. Frochot, F. G. Gatti, D. A. Leigh, L. Mottier, F. Paolucci, S. Roffia, G. W. H. Wurpel, *Science* **2001**, *291*, 2124.

[7] J. V. Hernandez, E. R. Kay, D. A. Leigh, *Science* **2004**, *306*, 1532.

[8] P. Mobian, J. M. Kern, J. P. Sauvage, *Angew. Chem. Int. Edit.* **2004**, *43*, 2392.

[9] V. Balzani, M. Clemente-Leon, A. Credi, B. Ferrer, M. Venturi, A. H. Flood, J. F. Stoddart, *Proc. Natl. Acad. Sci. USA* **2006**, *103*, 1178.

[10] M. Irie, *Chem. Rev.* **2000**, *100*, 1685.

[11] M. Kondo, Y. L. Yu, T. Ikeda, *Angewandte Chemie-International Edition* **2006**, *45*, 1378.

[12] Y. Zong, J. Ruhe, W. Knoll, *Thin Solid Films* **2005**, *477*, 203.

[13] R. Advincula, M. K. Park, A. Baba, F. Kaneko, *Langmuir* **2003**, *19*, 654.

[14] Z. F. Liu, K. Hashimoto, A. Fujishima, *Nature* **1990**, *347*, 658.

[15] T. Ikeda, O. Tsutsumi, *Science* **1995**, *268*, 1873.

[16] M. Z. Alam, T. Yoshioka, T. Ogata, T. Nonaka, S. Kurihara, *Chemistry-a European Journal* **2007**, *13*, 2641.

[17] S. Shinkai, *Pure & Appl. Chem.* **1987**, *59*, 425.

[18] Y. L. Yu, M. Nakano, T. Ikeda, *Nature* **2003**, *425*, 145.

[19] T. Hugel, N. B. Holland, A. Cattani, L. Moroder, M. Seitz, H. E. Gaub, *Science* **2002**, *296*, 1103.

[20] L. V. Schafer, E. M. Muller, H. E. Gaub, H. Grubmuller, *Angewandte Chemie-International Edition* **2007**, *46*, 2232.

[21] C. Zhang, M. H. Du, H. P. Cheng, X. G. Zhang, A. E. Roitberg, J. L. Krause, *Phys. Rev. Lett.* **2004**, *92*, 158301.

[22] M. Del Valle, R. Gutierrez, C. Tejedor, G. Cuniberti, *Nature Nanotechnology* **2007**, *2*, 176.

[23] C. Dugave, L. Demange, *Chemical Reviews* **2003**, *103*, 2475.

[24] T. Nagele, R. Hoche, W. Zinth, J. Wachtveitl, *Chemical Physics Letters* **1997**, *272*, 489.

[25] F. Krollpfeiffer, C. Muhlhausen, G. Wolf, *Annalen* **1934**, *508*, 39.

[26] J. Griffiths, *Chem. Soc. Rev.* **1972**, *1*, 481.

[27] N. Tamai, H. Miyasaka, *Chem. Rev.* **2000**, *100*, 1875.

[28] J. Henzl, M. Mehlhorn, H. Gawronski, K. H. Rieder, K. Morgenstern, *Angew. Chem. Int. Ed.* **2006**, *45*, 603.

[29] B. Y. Choi, S. J. Kahng, S. Kim, H. Kim, H. W. Kim, Y. J. Song, J. Ihm, Y. Kuk, *Phys. Rev. Lett.* **2006**, *96*, 156106.

[30] M. Alemani, M. V. Peters, S. Hecht, K. H. Rieder, F. Moresco, L. Grill, *J. Am. Chem. Soc.* **2006**, *128*, 14446.

[31] S. De Feyter, A. Gesquiere, M. M. Abdel-Mottaleb, P. C. M. Grim, F. C. De Schryver, C. Meiners, M. Sieffert, S. Valiyaveettil, K. Mullen, *Acc. Chem. Res.* **2000**, *33*, 520.

[32] C. L. Feng, Y. J. Zhang, J. Jin, Y. L. Song, L. Y. Xie, G. R. Qu, L. Jiang, D. B. Zhu, *Surf. Sci.* **2002**, *513*, 111.

[33] J. Zhang, J. K. Whitesell, M. A. Fox, *Chem. Mater.* **2001**, *13*, 2323.

[34] S. Yasuda, T. Nakamura, M. Matsumoto, H. Shigekawa, *J. Am. Chem. Soc.* **2003**, *125*, 16430.

[35] S. D. Evans, S. R. Johnson, H. Ringsdorf, L. M. Williams, H. Wolf, *Langmuir* **1998**, *14*, 6436.

[36] R. Wang, T. Iyoda, D. A. Tryk, K. Hashimoto, A. Fujishima, *Langmuir* **1997**, *13*, 4644.

[37] R. Micheletto, M. Yokokawa, M. Schroeder, D. Hobara, Y. Ding, T. Kakiuchi, *Applied Surface Science* **2004**, *228*, 265.

[38] F. Sagues, R. Albalat, R. Reigada, J. Crusats, J. Ignes-Mullol, J. Claret, *Journal of the American Chemical Society* **2005**, *127*, 5296.

[39] M. Matsumoto, D. Miyazaki, M. Tanaka, R. Azumi, E. Manda, Y. Kondo, N. Yoshino, H. Tachibana, *J. Am. Chem. Soc.* **1998**, *120*, 1479.

[40] M. Velez, S. Mukhopadhyay, I. Muzikante, G. Matisova, S. Vieira, *Langmuir* **1997**, *13*, 870.

[41] F. Nakamura, E. Ito, Y. Sakao, N. Ueno, I. N. Gatuna, F. S. Ohuchi, M. Hara, *Nano Letters* **2003**, *3*, 1083.

[42] N. Katsonis, T. Kudernac, M. Walko, S. J. van der Moten, B. J. van Wees, B. L. Feringa, *Adv. Mater.* **2006**, *18*, 1397.

[43] H. Akiyama, K. Tamada, J. Nagasawa, K. Abe, T. Tamaki, *Journal of Physical Chemistry B* **2003**, *107*, 130.

[44] K. Tamada, H. Akiyama, T. X. Wei, *Langmuir* **2002**, *18*, 5239.

[45] S. Sortino, S. Petralia, S. Conoci, S. Di Bella, *Journal of Materials Chemistry* **2004**, *14*, 811.

[46] M. Ito, T. X. Wei, P. L. Chen, H. Akiyama, M. Matsumoto, K. Tamada, Y. Yamamoto, *Journal of Materials Chemistry* **2005**, *15*, 478.

[47] Y. Q. Wen, W. H. Yi, L. J. Meng, M. Feng, G. Y. Jiang, W. F. Yuan, Y. Q. Zhang, H. J. Gao, L. Jiang, Y. L. Song, *Journal of Physical Chemistry B* **2005**, *109*, 14465.

[48] P. Cyganik, M. Buck, T. Strunskus, A. Shaporenko, J. D. E. T. Wilton-Ely, M. Zharnikov, C. Wöll, *J. Am. Chem. Soc.* **2006**, *128*, 13868.

[49] A. Shaporenko, M. Elbing, A. Baszczyk, C. von Hanisch, M. Mayor, M. Zharnikov, *Journal of Physical Chemistry B* **2006**, *110*, 4307.

[50] S. T. Pasco, G. L. Baker, *Synthetic Metals* **1997**, *84*, 275.

[51] H. J. Himmel, A. Terfort, C. Woll, *Journal of the American Chemical Society* **1998**, *120*, 12069.

[52] J. F. Kang, A. Ulman, S. Liao, R. Jordan, G. H. Yang, G. Y. Liu, *Langmuir* **2001**, *17*, 95.

[53] C. A. Hunter, K. R. Lawson, J. Perkins, C. J. Urch, *J. Chem. Soc., Perkin Transaction 2* **2001**, 651.

[54] C. A. Hunter, K. M. Sanders, *J. Am. Chem. Soc.* **1990**, *112*, 5525.

[55] Y. Wang, A. E. Kaifer, *Journal of Physical Chemistry B* **1998**, *102*, 9922.

[56] D. Hobara, O. Miyake, S. Imabayashi, K. Niki, T. Kakiuchi, *Langmuir* **1998**, *14*, 3590.

[57] N. Nishi, D. Hobara, M. Yamamoto, T. Kakiuchi, *Langmuir* **2003**, *19*, 6187.

[58] Q. Cheng, A. Brajter-Toth, *Anal. Chem.* **1995**, *67*, 2767.

[59] D.-F. Yang, C. P. Wilde, M. Morin, *Langmuir* **1996**, *12*, 6570.

Appendix to chapter 4

A- 4.1 Solid state structure analysis of an AZO1 precursor

Of particular interest were structural information of the azobiphenyl backbone and attempts to growth single crystals have been made with both compounds comprising the structural motive AZO1 and an AZO1 precursor called P-AZO1 hereafter. While the target structure AZO1 always provided too thin needles, single crystals suitable for X-ray analysis have been obtained by slow cooling a hot solution of P-AZO1 in toluene. P-AZO1 crystallizes acentric in the orthorhombic space group $Pna2_1$.

X-ray analysis of the thioacetate derivative of AZO1 showed that both biphenyl subunits are essentially planar, as the biphenyl subunit bearing the sulfur-group shows a torsion angle of 2.2(3)° and the other biphenyl exhibited a torsion angle of 2.5(3)° between the two phenyl-rings. The bond length between the two phenyl rings is 150.3(3) pm (C(5)-C(8)) and 151.0(3) pm (C(17)-C(20)), respectively, which is slightly longer than the length of the C(sp2)-C(sp2) bond in unsubstituted biphenyls (148 pm). Due to the planar nature of N=N-group, both biphenyl subunits reside in the same plane. Apart from the methyl group of the methylsulfoxy substituent, P-AZO1 shows an almost completely planar arrangement. The length of the molecule estimated by the S(1)−C(23) distance amounts to 1.9724(4) nm.

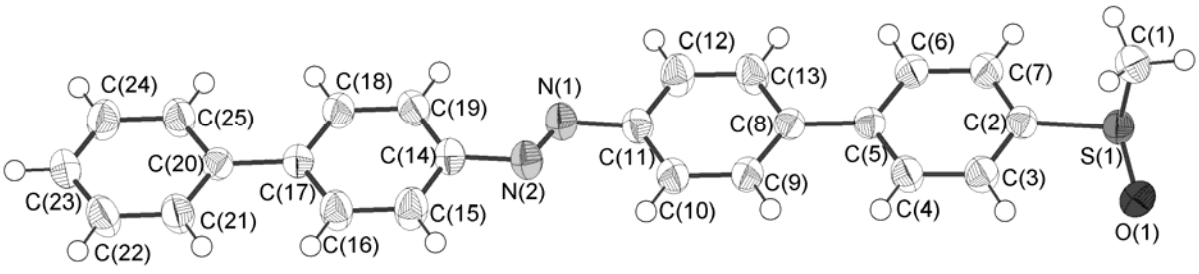

Figure A-4.1: Solid state structure of compound P-AZO1 (ORTEP, thermal ellipsoids set at the 50% probability level).Selected bond lengths/pm and bond angles/°: S(1)-O(1) 150.2(2), S(1)-C(1) 180.9(3), S(1)-C(2) 181.6(3), N(1)-N(2) 125.8(3), N(1)-C(11) 144.7(3), N(2)-

C(14) 144.9(3), C(5)-C(8) 150.3(3), C(17)-C(20) 151.0(3); C(13)-C(8)-C(5) 121.7(2), C(4)-C(5)-C(8) 121.5(2), C(21)-C(20)-C(17) 121.3(2), C(25)-C(20)-C(17) 122.0(2).

P-AZO1 ($C_{25}H_{20}N_2OS$): a = 815.62(16), b = 557.76(11), c = 43.966(9) pm, $\alpha = \beta = \gamma = 90°$, V = 2000.1(7) · 10^6 pm^3; orhtorhombic $Pna2_1$, Z = 4, $\rho_{calc.}$ = 1.317 gcm^{-1}, $\mu(Mo_{K\alpha})$ = 0,181 mm^{-1}, STOE IPDS2, $Mo_{K\alpha}$-radiation, λ = 0.71073 Å, T = 200 K, $2\theta_{max}$ = 52°; 6869 reflections measured, 3603 independent reflections (R_{int} = 0.0519), 3221 independent reflections with $F_o > 4\sigma(F_o)$. The structure was solved by direct methods and refined, by full-matrix least square techniques against F^2, 263 parameters (S, O, N, C refined anisotropically, H atoms were calculated at ideal positions.); $R1$ = 0.0431; $wR2$ = 0.1218 (all data); Gof: 1.074; maximum peak 0.192 $Å^{-3}$. CCDC-642546 contains the supplementary crystallographic data for this paper. These data can be obtained free of charge via www.ccdc.cam.ac.uk/conts/retrieving.html (or from Cambridge Crystallographic Data Centre, 12 Union Road, Cambridge CB21EZ, UK; fax: (+44)1223-336-033; or deposit@ccdc.cam.ac.uk).

A- 4.2 UV/Vis spectroscopy and photo-irradiation

All the work presented in this session has been carried on by the group of Professor Maria Anita Rampi at the University of Ferrara (Italy). This appendix has been added to the chapter 4 to better clarify the main results presented in this chapter.

A- 4.2.1 Photo-isomerization in Solution

UV-vis kinetic analysis is complicated by both the overlapping of the spectra of *trans*- and *cis*-isomer and by the relatively fast thermal and photochemical back reaction.

^{1}H-NMR-spectroscopy makes it possible to distinguish between the *trans*- and *cis*-isomer of azo-compounds due to the different spatial arrangements of the two isomers. The yield of the photoconversion in solution of AZO1 and AZO2 from the *trans* to the *cis* form has been calculated from the ratio of the ^{1}H-NMR signals of the two isomers in the initial and in the photostationary state.[1] The spectrum of the *cis* form has been calculated combining the data of the % of the photoconversion from *trans* to *cis* form obtained form the ^{1}H-NMR spectra and the related UV-Vis spectra.

It was found to amount to 0.88±0.03 for AZO1, being the yield of photo-isomerization (AZO2: 0.89±0.02; see also Table 4.1). Taking into account this calculated composition of the photostationary state it has been possible to deconvolve the UV-vis spectrum giving the spectrum of the pure *cis*-isomer of AZO2 (and AZO1, Fig. A-4.2).

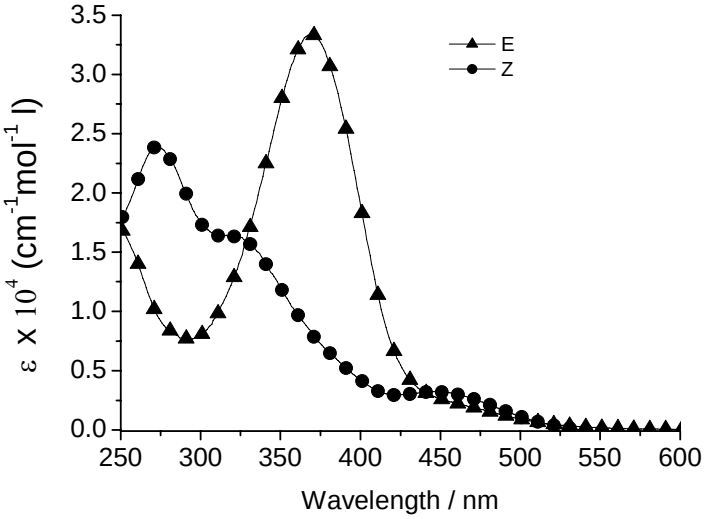

Figure A-4.2: Measured UV-Vis absorption spectra of the *trans* isomer and calculated UV-Vis absorption spectra of the *cis* isomers of AZO1 in a chloroform solution.

The kinetics of the thermal back *cis*→*trans* isomerization of AZO1 was followed by recording the increase of the absorption in the UV-vis spectrum at λ= 370 nm (Fig. A-4.3).

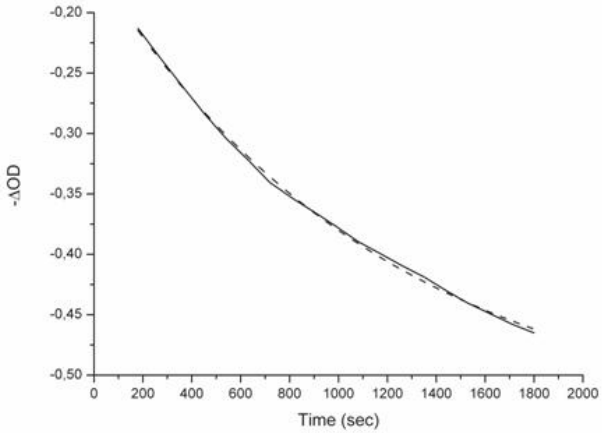

Fig. A-4.3: Change of OD for AZO1 recorded at l = 370 nm vs. time, for the thermal *cis* to *trans* back reaction of AZO1 in chloroform. The dashed line represents the best fit of the experimental data to a first order kinetic, with a k = 8.6x10-4 sec-1.

As shown in Table 1, from this data the lifetime and the rate constant for AZO2 was calculated according to a first order kinetic equation to k= $1.19x10^{-4} \pm 0.09$ s^{-1} (AZO1: k= $8.55x10^{-4} \pm 0.30$ s^{-1}). These results indicate that the yield of photo-conversion is very similar for both compounds. A comparison between the rates of the thermal back reaction for both AZO1 and AZO2 in solution is complicated by the different structural features of the two compounds. AZO1 exists as monomer in solution, while AZO2 exists as dimer. In addition, AZO2 has four extra methyl-groups. Even if a thorough explanation of such kinetic difference is difficult, we infer that the bulky methyl groups together with its dimeric state slow down the back isomerization kinetic of the AZO2.

A- 4.2.2 Photo-isomerization in SAMs

The photo-isomerization process of both AZO1 and AZO2 organized in SAMs on semitransparent Au and Pt metal film (nominal thickness= 20 nm) was followed by UV-vis spectroscopy in transmission mode. The variation of absorbance related to the *trans→cis* isomerization $\Delta A_{trans \rightarrow cis}$ of single monolayers of azo-compounds is usually smaller than 0.003 and can be severely affected by surface plasmon bands (SPBs) of the metal surface. Unlike Au surfaces, Pt surfaces do not exhibit SPBs in the region 200-900 nm[2-4] and both substrates have been used in this investigation. Furthermore, the irradiation of the samples was performed *"in-situ"*, i.e. the isomerizing light beam was irradiated at 90° with respect to the UV-vis sampling beam, all inside the spectrophotometer to avoid artifacts related to the repositioning of the sample.

Strong interactions of organic compounds in LB films usually give rise to a clear bathochromic shift in the UV-vis spectrum of the film compared to solution studies.[5, 6] The UV-vis spectra of AZO1 in solution and when organized in SAMs, however, are very similar (see Fig. 4.9) suggesting small dependence on their environment. The same has been observed from teh Uv-spectra of AZO2 in solution and in SAMs. Therefore, we assume that the extinction coefficients of the *trans*- and the *cis*-isomers do not change considerably upon organization in SAMs. Under this approximation, the yield of the *trans→cis* photo-conversion of SAMs of AZO1 and AZO2 on Pt as well as on Au surfaces can be calculated from the absorption spectra of the photostationary state and the spectra of the pure *trans*- and pure (computed) *cis*-isomer in solution. Deconvolution of the absorption spectra of the

photostationary state then gave a yield of photo-isomerization on Au substrates of 0.95 ± 0.02 for AZO2 and 0.97 ± 0.03 for AZO1 (see also Table 4.1). Therefore, within the experimental error comparable yields of photo-conversion were obtained for both compounds organized in SAMs on gold. In particular for AZO1, a yield of photoconversion very close to 100% was observed. This is a very interesting and important result, because high yields of photo-isomerization of SAMs of azo-compounds have mostly been achieved, when special measures were taken to provide free volume in the SAM.

The thermal *cis* → *trans* back isomerization of AZO1, both in solution and in SAMs on Au and Pt, has been followed by recording the increase of UV-Vis spectra at λ = 360 nm (see Fig. A-4.4 for the OD measured on for SAM of AZO1 on gold substrate). From these data the lifetimes and the constant rates were calculated.

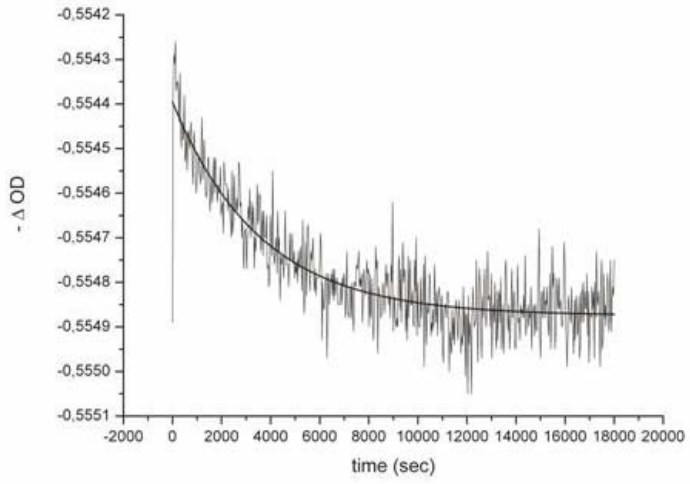

Figure A-4.4: Changes of OD at l = 370 nm vs. time for the thermal *cis* to *trans* back reaction of AZO1 in SAMs on Au surfaces. The black line represents the best fit of the experimental data to a first order kinetic, with a k = 1.33x10 -4 sec^{-1}.

The kinetic constants reported in the main text for the back thermal reaction in solution, on Pt and on Au surfaces are calculated according to a first order kinetic equation. For SAMs of AZO2 on Au k= $1.67x10^{-4}$ ± 0.10 s^{-1} was found and k= $1.33x10^{-4}$ ± 0.06 s^{-1} for SAMs on Pt For SAMs of AZO1 has been found: k= $2.82x10^{-4}$ ± 0.14 s^{-1} on Au and k= $2.21x10^{-4}$ ± 0.05 s^{-1} on Pt. The kinetic constants reported in the table 4.1 for the back thermal reaction in solution, on Pt and on Au surfaces are calculated according to a first order kinetic equation. Hence, comparable values have been determined for the thermal *cis*→*trans* isomerization of both compounds.

A- 4.3 Experimental procedures for Photochemical Investigations

UV/Vis spectra have been recorded with a Kontron Uvikon 931 spectrophotometer. The irradiation of the SAMs of AZO1 and AZO2 has been performed *in-situ* inside the spectrophotometer cavity. The irradiation cycles have been executed with a Spectraluminator LOT Oriel. The exposure time of the irradiation has been indicated in the figures. Measurements on SAMs on Pt and Au substrates were carried out under nitrogen in order to avoid the substrate oxidation. The bandwidth of the light source in the UV/Vis region was 5 nm. The photoisomerization of the SAMs has been measured as spectral differences to reduce the interference of the metal absorption band. Pt metal surface has been used as a solid substrate in order to record the spectral differences related to the *trans→cis* isomerization without the contribution of the changes in Surface Plasmon bands of the metal.

	Photo-isomerization yield	$K_{cis\text{-}trans}$ **(sec^{-1}) x10^{-4}**
AZO1		
solution	0.88 ± 0.03	8.5 ± 0.30
SAM on Au	0.97 ± 0.03	2.82 ± 0.14
SAM on Pt	-	2.21 ± 0.05
AZO2		
solution	0.89 ± 0.02	1.19 ± 0.09
SAM on Au	0.95 ± 0.02	1.67 ± 0.10
SAM on Pt	-	1.33 ± 0.06

Table 4.1: Yields of photo-isomerization and rate constants, $k_{cis\rightarrow trans}$, of the thermal back *cis→trans* reaction of AZO1 and AZO2 in solution and in SAMs on **Pt** and **Au** surfaces. The errors of the yields of photo-isomerization are the errors of integration of the NMR peaks. The errors on the kinetic constants are calculated by Gaussian Error.

References of the Appendix to chapter 4

[1] K. M. Tait, J. A. Parkinson, S. P. Bates, W. J. Ebenezer, A. C. Jones, *Journal of Photochemistry and Photobiology a-Chemistry* **2003**, *154*, 179.

[2] G. Kalyuzhny, M. A. Schneeweiss, A. Shanzer, A. Vaskevich, I. Rubinstein, *Journal of the American Chemical Society* **2001**, *123*, 3177.

[3] M. Wanunu, A. Vaskevich, I. Rubinstein, *Journal of the American Chemical Society* **2004**, *126*, 5569.

[4] S. Conoci, S. Petralia, P. Samori, F. M. Raymo, S. Di Bella, S. Sortino, *Advanced Functional Materials* **2006**, *16*, 1425.

[5] J. R. Lakowicz, *Anal. Biochem.* **2001**, *298*, 1.

[6] J. M. Pedrosa, M. T. M. Romero, L. Camacho, D. Möbius, *J. Phys. Chem. B* **2002**, *106*, 2583.

[60] G. Yang, G.-Y. Liu, *J. Phys. Chem. B* **2003**, *107*, 8746.

[61] P. Cyganik, M. Buck, J. D. E. T. Wilton-Ely, C. Woll, *Journal of Physical Chemistry B* **2005**, *109*, 10902.

[62] W. Azzam, C. Fuxen, A. Birkner, H. T. Rong, M. Buck, C. Wöll, *Langmuir* **2003**, *19*, 4958.

[63] L. G. Duan, S. J., *J. Phys. Chem. B* **2001**, *105*, 9812.

[64] W. B. Caldwell, D. J. Campbell, K. Chen, B. R. Herr, A. M. Mirkin, M. K. Durbin, P. Dutta, K. G. Huang, *J. Am. Chem. Soc.* **1995**, *117*, 6071.

[65] M. Jaschke, H. Schonherr, H.-J. Butt, E. Bamberg, M. K. Besocke, H. Ringsdorf, *J. Phys. Chem.* **1996**, *100*, 2290.

[66] T. Takami, B. Delamarche, C. G. Michel, H. Wolf, H. Ringsdorf, *Langmuir* **1995**, *11*, 3876.

[67] H. Wolf, H. Ringsdorf, B. Delamarche, T. Takami, H. Kang, B. Michel, C. Gerber, M. Jaschke, H.-J. Butt, E. Bamberg, *J. Phys. Chem.* **1995**, *99*, 7102.

[68] S. W. Han, C. H. Kim, S. H. Hong, Y. K. Chung, K. Kim, *Langmuir* **1999**, *15*, 1579.

[69] K. Tamada, J. Nagasawa, F. Nakanishi, K. Abe, T. Ishida, M. Hara, W. Knoll, *Langmuir* **1998**, *14*, 3264.

[70] T. Ishida, H. Fukushima, W. Mizutani, S. Miyashita, H. Ogiso, K. Ozaki, H. Tokumoto, *Langmuir* **2002**, *18*, 83.

[71] S. C. B. Mannsfeld, T. W. Canzler, T. Fritz, H. Proehl, K. Leo, S. Stumpf, G. Goretzki, K. Gloe, *J. Phys. Chem. B* **2002**, *106*, 2255.

[72] G. H. Yang, Y. L. Qian, C. Engtrakul, L. R. Sita, G. Y. Liu, *Journal of Physical Chemistry B* **2000**, *104*, 9059.

[73] G. E. Poirier, *Langmuir* **1997**, *13*, 2019.

[74] S. J. Sowerby, M. Edelwirth, M. Reiter, W. M. Heckl, *Langmuir* **1998**, *14*, 5195.

[75] R. R. Nazmutdinov, J. D. Zhang, T. T. Zinkicheva, I. R. Manyurov, J. Ulstrup, *Langmuir* **2006**, *22*, 7556.

[76] Z. X. Wang, A. M. Nygard, M. J. Cook, D. A. Russell, *Langmuir* **2004**, *20*, 5850.

[77] W. P. Fitts, J. M. White, G. E. Poirier, *Langmuir* **2002**, *18*, 1561.

[78] L. P. Xu, L. J. Wan, *J. Phys. Chem. B* **2006**, *110*, 3185.

[79] G. Pace, V. Ferri, C. Grave, M. Elbing, C. von Hanisch, M. Zharnikov, M. Mayor, M. A. Rampi, P. Samori, *Proceedings of the National Academy of Sciences of the United States of America* **2007**, *104*, 9937.

[80] J. C. Love, L. A. Estroff, J. K. Kriebel, R. G. Nuzzo, G. M. Whitesides, *Chemical Reviews* **2005**, *105*, 1103.

[81] A. S. Blum, J. G. Kushmerick, D. P. Long, C. H. Patterson, J. C. Yang, J. C. Henderson, Y. X. Yao, J. M. Tour, R. Shashidhar, B. R. Ratna, *Nature Materials* **2005**, *4*, 167.

[82] R. E. Holmlin, R. Haag, M. L. Chabinyc, R. F. Ismagilov, A. E. Cohen, A. Terfort, M. A. Rampi, G. M. Whitesides, *Journal of the American Chemical Society* **2001**, *123*, 5075.

[83] A. Salomon, D. Cahen, S. Lindsay, J. Tomfohr, V. B. Engelkes, C. D. Frisbie, *Advanced Materials* **2003**, *15*, 1881.

[84] J. E. Green, J. W. Choi, A. Boukai, Y. Bunimovich, E. Johnston-Halperin, E. DeIonno, Y. Luo, B. A. Sheriff, K. Xu, Y. S. Shin, H. R. Tseng, J. F. Stoddart, J. R. Heath, *Nature* **2007**, *445*, 414.

[85] A. Nitzan, M. A. Ratner, *Science* **2003**, *300*, 1384.

[86] J. R. Heath, M. A. Ratner, *Phys. Today* **2003**, *May*, 43.

CHAPTER 5

MIXED SELF-ASSEMBLED MONOLAYERS

5.1 Introduction

The controlled spatial confinement of individual functional nano-objects on surfaces is of paramount importance for basic studies on single molecule properties, *i.e.* reactivity and kinetics[1], paving the way towards applications in the fields of (bio)chemical sensors and molecular electronics, and ultimately for the miniaturization of electronic devices. Numerous molecular switches and motors have been proposed.[2] However, in spite of their good dynamic properties thoroughly characterized in solution, very little has been done on the exploitation of these characteristics for the development of electronic (nano)devices operating on surfaces.[3] The major restriction is represented by constraints brought into play by the solid surface, such as the molecule-substrate interactions, the steric hindrance due to dense packing at surfaces reducing the molecular conformational freedom, the instability and uncertainty of the binding, to name a few. All these factors drastically affect the well established solution properties and hamper the applicability of these molecules in electronic devices.

Of particular importance as a first step is the building-up, with nanoscale precision, of highly ordered multi-component arrays of functional units on solid substrates, to enable the active functional group to be easily addressed. This ordered spatial confinement of single active molecules permits the ultimate control of the single molecule properties when an external stimulus is applied and, on the long term, it should make it possible to shrink the size of electronic memory bits to the limit of a single molecule.

Among different methodologies proposed for the assembly of functional molecules on solid substrates, the chemisorption of Self-Assembled Monolayers (SAMs) on gold is the most widely studied and characterized. Their easy preparation and high stability make them ideal systems for further improving the control over the assembly at the supramolecular level of active molecules on gold. Despite of the good control achieved on the molecular binding and packing in mono-component SAMs on Au(111), *e.g.* of alkanethiols or arenethiols, it is still very difficult to prepare mixed SAMs in which a single active component can be easily addressed.

Many efforts have been devoted to the isolation of single active molecules as guests in a hosting SAM.[4] Unfortunately, mixing two thiolated compounds on a metallic substrate leads either to phase segregation[5] of the two components in separate single component domains[6-8] or to the insertion of the guest molecules at defect sites of the hosting molecular matrix[9-11]. The latter case allows for the spatial confinement of active molecules, although their location at defect sites reflects the poor stability of the molecule-substrate bond, thus leading to great uncertainty in the measured molecular properties. In fact, single molecules or small molecular clusters chemisorbed at defect sites can easily diffuse, desorb and re-adsorb, and they are more subject to conformational fluctuations because of the lack of lateral packing. An alternative to this approach is to favour the assembly of multi-component crystalline domains. In such multi-component bidimensional crystal, the active functional molecules will be "neatly diluted" on the surface. A good design of the molecular components would make possible to build ordered arrays of target functional molecules shielded from each other by an inert hosting matrix.

In this chapter we present results obtained from a model system designed to favour the miscibility in a bi-dimensional crystal. Taking advantage of basic principles of supramolecular chemistry[12], here we devise a new and general approach to tailor multi-component crystalline SAMs, thereby achieving control over the spatial confinement of functional nano-objects on surfaces with sub-nanometer resolution. Sub-molecularly resolved STM imaging provides direct evidence for the formation of such crystalline mixed SAMs. The description and discussion of the experimental results will be reported after a brief overview on SAM patterning and mixed SAMs.

5.2 Patterning of SAMs

The ability to control the spatial arrangements is a crucial factor in innovative technologies, such as molecular-scale electronics. The inherent chemical and physical properties of SAMs offer the possibility to pattern a substrate at the molecular scale. Multi-component monolayers extent the versatility of SAMs and open new perspectives for their technological applications. As a matter of example, in a bi-component SAM each component can be functionalized in a manner to expose different functionality, giving rise to a SAM featuring different reactivity on the same surface.

The patterning of a SAM has been engineered in different ways. The most often employed strategy is desorption of molecules previously bound in a SAM to favour the adsorption of differently functionalized molecules (scheme 5.1). The desorption might be induced i) by electrochemical reaction, in this case a reduction voltage is applied to the gold electrode to favour the desorption of molecules bound on the gold while new thiolated derivatives coming from the solution fill the as formed molecular vacancies; ii) by irradiation with energetic beams which destroy the assembly at the target surface area; iii) by a scanning probe which can favour the molecules removal. After desorption the patterned surface might be kept uncovered or backfilled with new adsorbates[9].

In the early ‘90s Whitesides and co-authors introduced a new technique, called soft-lithography, for the precise patterning of metal surfaces using a SAM as ultra-thin organic resist.[13] The SAM act as a protective layer limiting the metal oxidative etching allowing a highest flexibility in patterning the metal substrate.

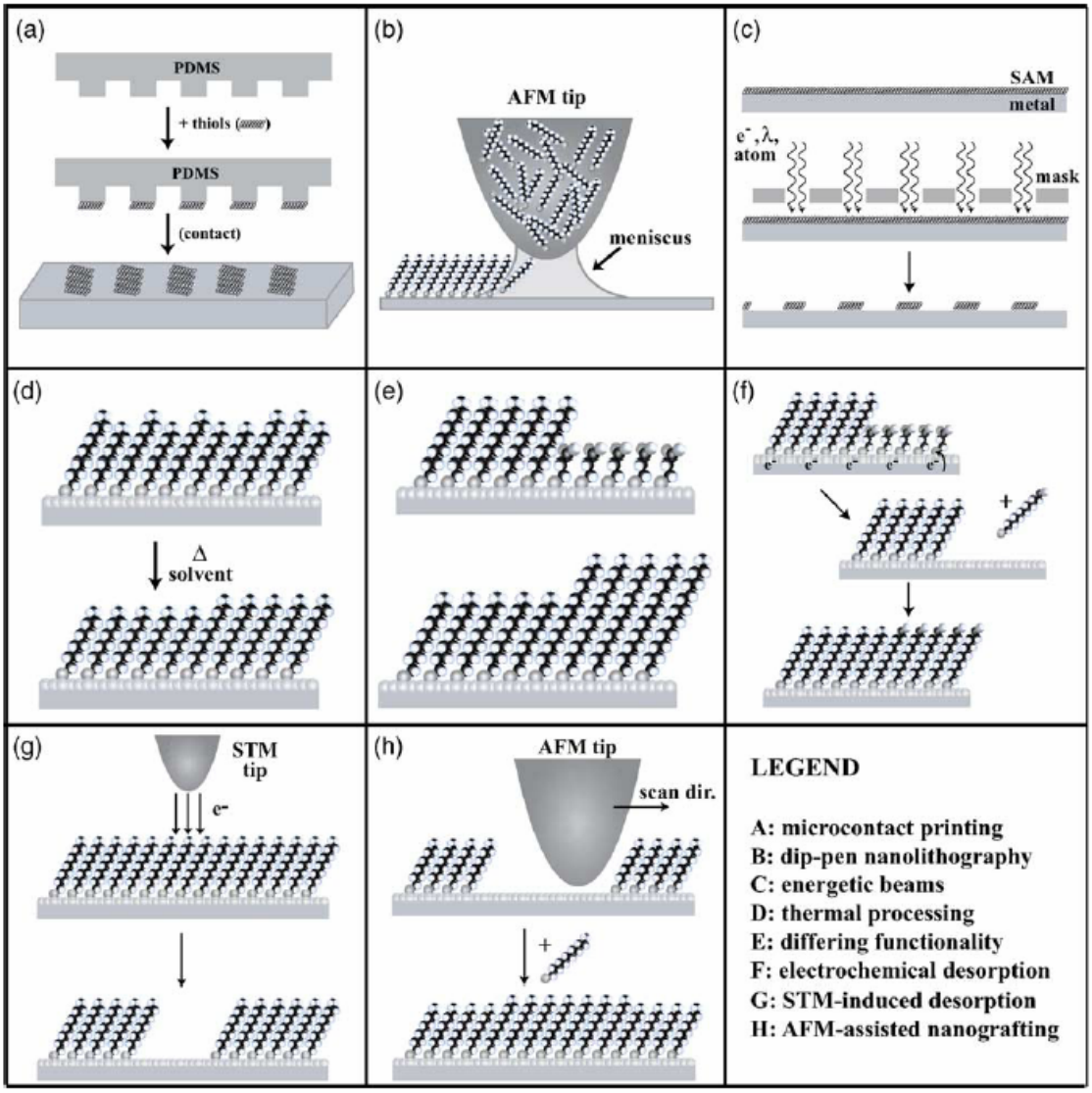

Scheme 5.1: Schematic representation of the different techniques developed to pattern a SAM.[9]

Patterning of features in multi-components SAMs has been successfully demonstrated using methods such as "soft lithography",[13-15] selective desorption by electrochemical methods,[16, 17] and scanning probe lithography.[18-21]

Defects sites like domain boundaries, molecular vacancies and gold step edges are sites of high probability for absorption. It has been shown that incoming ("guest") molecules will insert into a ("host") SAM at its local defect sites by exposing the preformed SAM to a solution of guest adsorbate that is of low concentration (typically 0.1-0.5 mM) and for short periods of time (minutes to hours). Molecules adsorbed at defects sites are easier to be accessed by solvent as well as by impurity, as they are not protected by the neighbouring

molecules like in the closed packed film. Furthermore these defect sites within the "host" SAM are the most susceptible to exchange to new "guest" molecules.

Mixed SAM can be also prepared through electrochemical processes on the preformed SAM. As previously described, it is possible to desorb thiolated molecules from a gold electrode substrate by applying a reduction potential (Scheme 5.1-F). This reaction can be used to remove molecules from the surface for then to refill the as originated molecular vacancies with a second component. Kakiuki and co-authors prepared a three components mixed SAM exploiting the difference in reduction potential between different thiolated derivatives. In particular, they prepared, by co-adsorption from solution, a bi-component SAM of 3-mercapto-propionic acid (3-MPA) and undecanethiol (UDT). They selectively desorbed the 3-MPA, as it has a less negative reduction potential than UDT, and they backfilled the SAM with either n-hexadecanthiol or 11-mercaptoundecanoic acid[17].

In the following, the case of binary SAMs formed from co-adsorption from solution containing two thiolated components will be described though, the kinetic and thermodynamic factors reported similarly affect multi-component SAMs.

5.2.1 Thermodynamic and kinetic factors in the formation of Mixed SAMs

The composition of a SAM is the result of a delicate interplay between kinetics and thermodynamics. Upon mixing in the incubating solution two components which differ enough in molecular composition, the most common observation in the SAM is a short-range phase separation. This means that the two compounds aggregate into homogeneous mono-component domains to maximize homo-molecular interactions. The relative fractional coverage of molecules on the surface will not necessarily reflect that of the solution. This phenomenon is not surprising as the interactions playing role during the molecular assembly process on the substrate are different from the one which stabilize molecules in solution. This phase separation (or phase segregation) in ordered mono-component domains is an evidence that enthalpic interactions are important as they determine the single domain structure. In fact, considering a pure entropic contribution to the formation of the molecular patterning, completely mixed domains should be formed. Instead, the intermolecular interactions within a molecular domain are often similar to those in a crystal. However, the size of each domain,

the density of defects over the entire SAM and the ratio between the two components at the surface are under kinetic control.

The binding competition between the two adsorbates depends on their relative solvation, the sticking probability[22][i] and the intermolecular interactions at the monolayer.

A perfect definition for SAMs is provided by Allara and co-workers[10]: SAMs are 2D molecular assemblies trapped at local thermodynamic minima. However we do not know how close these structures are to thermodynamic equilibrium, i.e. to the absolute minimum. Gaining insight into the physical-chemical factors that govern phase separation into intermolecular interactions between adsorbates opens the way to the formation of nanoscale structures that can be controlled by the correct design of the molecular components.

Plotting the mole fraction in the monolayer as a function of its mole fraction in solution Allara and co-authors found that if the two components of the surface act independently, then the contact angle is a linear function of the composition of the surface. In order to describe the thermodynamics of those systems the authors considered the Bragg-Williams model for binary ideal solution. This model defines a thermodynamic relationship between the composition of the solution and the composition of the SAM also in terms of interaction between nearest neighbour within the SAM. Equilibrium state is determined by the equilibrium between molecules in the SAM and by the exchange equilibrium between molecules in solution and in the SAM. At room temperature, the exchange equilibrium is strongly dependent on the solution concentration, but not enough to give a first order reaction with respect to thiol concentration, and, on the defects sites within the monolayer. Once a first ordered monolayer is formed the exchange process is slowed down even if the equilibrium is not reached, in fact molecules stabilized by the lateral packing in a crystalline domain are less likely to desorb. SAMs formed at room temperature usually do not reach the equilibrium.

Essentially, three scenarios can be drawn for the phases formed during different thiolated components co-adsorption forming a SAM: i) the SAM is formed by one phase defined by a mono-component SAM formed uniquely by one of the two components (Fig. 5.1-a); ii) phase segregation can occur leading to isolated mono-component domains as shown in Fig. 5.1-b); iii) a fully miscible SAMs can be formed, that is “a homogeneous

[i] The sticking probability is the probability of a binding event upon adsorption of the molecule or atom on the surface.

mixture of both components", like a bi-component crystalline domain and, "it will not consist of regions of separate phases"[23, 24] (Fig. 5.1-c).

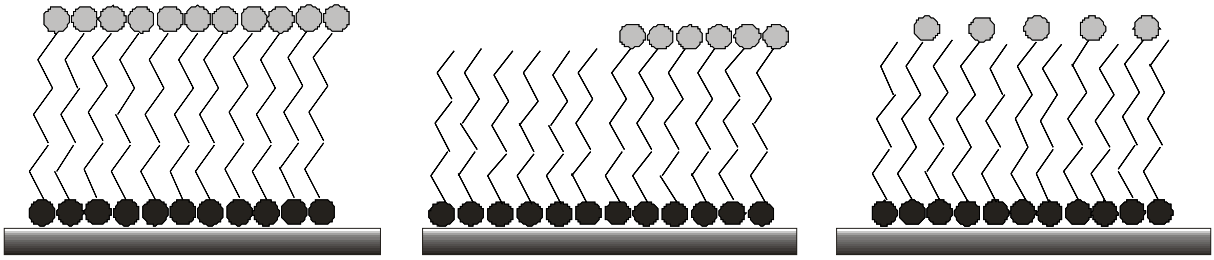

a) **b)** **c)**

Figure 5.1: Schematic drawings of: **a)** mono-component SAM; **b)** phase-segregated SAM; **c)** homogeneously mixed SAM.

Assumptions of the free energy model are: i) thiols in solution are not interacting and ii) no conformational reorganization energy contributes to the SAM formation. The equilibrium is described in equation 5.1:

$$A_{sol} + B_{sol} \leftrightarrow A_{SAM} + B_{SAM} \tag{5.1}$$

where A_{sol} and B_{sol} are the solution concentration of the component A and B respectively and A_{SAM} and B_{SAM} are the corresponding concentrations in the SAM.
The chemical potentials in solution (μ_{sol}) and on surface (μ_{SAM}) are described as follow:

$$\mu_i^{sol} = \mu_i^{+} + kTlny_i \tag{5.2}$$

$$\mu_i^{SAM} = \mu_i^{*} + kTlnx_i + \omega(1 - x_i)^2 \tag{5.3}$$

where for the component i: μ_i^{+} is the chemical potential of the thiol when is at infinite dilution; μ_i^{*} is the chemical potential of the thiolate in the single component SAM; y_i is the mole fraction in solution; x_i is the mole fraction in the SAM; ω is the interaction parameter, which describes intermolecular interactions within the SAM; k is the Boltzmann's constant; T is the absolute temperature of the system. Assuming the infinite dilution the activity coefficient γ_i, is equal to 1, therefore the molar activity a_i is equal to x_i.

$$\omega = (Z/2)[2\omega_{AB} - \omega_{AA} - \omega_{BB}] \tag{5.4}$$

Z, is the number of nearest neighbours in the SAM, ω_{ij} is the interaction energy between molecules i and j. The free energy associated to the SAM formation is:

$$\Delta f = x_A(\mu_A^{SAM} - \mu_A^{sol}) + x_B(\mu_B^{SAM} - \mu_B^{sol}) \tag{5.5}$$

$$\Delta f = x_A(\mu_A^{*} - \mu_A^{+}) - x_A kT \ln y_A = x_B(\mu_B^{*} - \mu_B^{+}) - x_B kT \ln y_B + \Delta f_{mixing}^{SAM} \tag{5.6}$$

The free energy Δf of mixing of the components in the SAMs Δf_{mixing}^{SAM}, is:

$$\Delta f_{mixing}^{SAM} = kT\left(x_A \ln x_A + x_B \ln x_B\right) + \omega x_A x_B \tag{5.7}$$

The first term of equation 5.7 is the entropy of mixing; the second term is the internal enthalpy of mixing. The model does not account for the conformational rearrangement of the chains needed to the optimization of the lateral interactions in the SAMs. This is a pretty strong approximation even if the main conclusions of the model are consistent with the experimental evidences.

Further mathematical developments of the model are reported in the paper from Folkers and co-author,[23] in the following we present the main conclusions of the work arising from the calculation of the concentration values giving the absolute and the relative minima of equation (5.6) therefore, giving the equilibrium conditions:

The most important parameter that determines the phase behaviour of the SAM is the interaction parameter ω, which hold for the enthalpic contribution to the free energy of the SAM:

- for $\omega<0$ the interactions between unlike molecules (AB) are more favourable than interactions between like molecules (AA or BB) and homogenous mixing would be favoured (Fig 5.1-c) for all the solution concentrations;
- for $\omega=0$ the mixture is ideal, i.e. AA, BB, AB interactions have the same enthalpic energy therefore, entropy will still favour the formation of a homogeneously mixed domain (one single phase in the SAM);
- for $0<\omega<2kT$, the enthalpic energy balance between different molecule-molecule interactions, would favour the self-interactions between like molecules, but the entropy contribution to the free energy still dominates over the assembly, and it would still be possible to observe homogeneous mixing of molecules A and B in the SAM;

- for ω=2kT we encounter the critical mixing point;

for ω>2kT hetero-molecular interactions are energetically not favoured and for any solution concentration the maximum minimization of the free energy would lead the formation of a single component SAM (e.g. of A if $\omega_{AA} > \omega_{AB}$ and $\omega_{AA} > \omega_{BB}$) and metastable phases appear (Fig. 5.1-a); i.e. those are phases whose composition x_i is in equilibrium with the solution ($(d\Delta f/dx_i)=0$ and $\Delta f_{xi}=0$) but they do not represent an absolute minimum in the free energy of the system[ii].

Phase segregation indicates that any of the different molecular domains is energetically favoured and accessible at ambient temperature. The most stable domain is represented by the molecular assembly that ensures the best interplay between the overall intermolecular and surface interactions leading to the highest minimization of the domain free energy.

An important conclusion of this theoretical work is that for a SAM in equilibrium with a contacting solution, the coexistence of two phases above the same substrate can occur only for a specific solution concentration $X=\exp\left(\frac{(\mu_A^* - \mu_A^+) - (\mu_B^* - \mu_B^+)}{kT}\right)$ for which $x_A=x_B=0.5$ and, for ω>2kT. Without the achievement of at least one of these conditions the model shows that at thermodynamic equilibrium with a solution containing a mixture of two components, the SAM consists of one single phase. Therefore, the formation of phase separated SAMs (metastable states according to the model) over a wide range of concentration suggests that the SAMs have not reached the equilibrium (Fig. 5.1-b).[25] The equilibrium can be reached more quickly if the exchange between thiolates in the SAM and thiols in solutions is favoured. Actually, this exchange is slow and incomplete at room temperature and becomes slower with the increasing length of as the alkyl group on the thiol functionalized molecule.

Solvent effects may also play a role in the adsorption process. A low solubility determines the spontaneous aggregation of the thiolated molecules and therefore the dynamics of absorption, desorption and diffusion will be slower and the possibility to anneal defects into the assembly is also reduced. In a bi-component solution the difference in solubility can play an important role when diluting the system. The molecular component that experiences the highest degree of solvation is less available to the binding on the gold substrates therefore the formation of molecular assembled growth nuclei is slower.

[ii] Metastability is the ability of a non-equilibrium state to persist for a long period of time.

Molecules bearing distinct ω-functional groups might also lead to phase segregation.[26] Whitesides and co-authors found that SAMs formed by OH-terminated and CH_3-terminated, as well as COOH-terminated and CH_3-terminated, alkylthiols are slightly miscible.[27, 28]

Phase-separated SAMs have been also observed for adsorbates differing in buried functional groups, i.e. functional groups added in the chain backbone. Upon mixing decanethiol and 3-mercapto-N-nonylpropionammide at different molar ratio in solution, phase separation was always obtained. This phenomenon has been inferred to the presence of hydrogen bond in the mono-component domains formed by the 3-mercapto-N-nonylpropionammide [9, 29].

By varying the chain length the interplay between kinetics and thermodynamics is more evident. Spontaneous phase separation often occurs upon co-adsorption from miscible solutions of *n*-alkanethiols which differ by more than 2 methylene units. For a chain length difference of 1 or 2 methylene groups phase separation is less likely unless post-adsorption processing, like thermal annealing, is performed.[30, 31]

Molecules with longer chain tend to dominate the surface coverage over the assembly by virtue of enhanced stability imparted by the greater interchain interactions, thus it will be found in greater concentration on the surface compared to shorter chain. Shorter chains are less solvated and diffuse more rapidly in solution than on the surface so their surface coverage is higher at the beginning of the assembly process, but over long incubation time the more stable interchain interactions assured by the longest chain make them to dominate over the final SAM coverage.[22, 24] However molecules of similar composition are more likely not to phase separate upon co-adsorption.[30] The energy of solvation and the exchange equilibrium dynamics will be similar due to the similar molecular structures and the energy differences between homo-molecular and hetero-molecular interactions will be not so high to partially stabilize mixed domains.

5.3 Results and discussion

In order to avoid phase segregation and foster complete miscibility of two molecular components in a SAM, a fine tuning of the interplay of intramolecular, intermolecular and interfacial interactions is required.

Complete miscibility may be achieved by stabilizing the hetero-molecular interactions between the two components with respect to the homo-molecular interactions. It is also possible to design molecular components with similar chemical structures, thereby exhibiting energetically comparable hetero-molecular and homo-molecular interactions within the SAM therefore, favouring the mixing. An accurate design of the two components is necessary and specific intermolecular interactions have to be defined.

To accomplish this goal we have designed and synthesized (in collaboration with Professor Anne Petitjean from Queen's University, Ontario, Canada, and Marie-Noëlle Lalloz from Professor Lehn group, ISIS-ULP, Strasbourg, France) molecules **1** and **3** and combined it with commercial undecanethiol (**2**) (Fig. 5.2). Both molecules bear (i) a sulphur-containing end-group to promote covalent binding to Au surfaces, and (ii) an alkyl backbone to favour the lateral packing within the SAMs through van der Waals interactions, significantly, also of hetero-molecular type. Moreover, molecules **1** and **2** expose an amide group to promote highly directional homo-molecular interactions through the formation of linear hydrogen bonded networks[32-34].

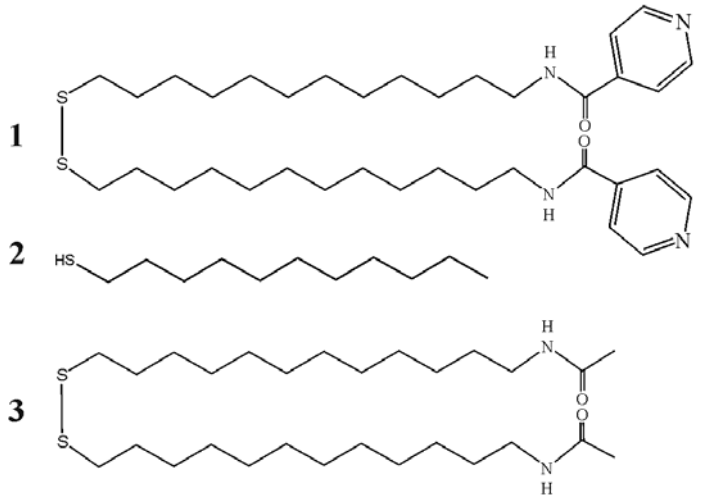

Figure 5.2: Molecular structures of compounds under study: pyridine-amide derivative (**1**), undecanethiol (**2**) and the methyl-amide derivative (**3**).

5.3.1 Mono-component SAMs

The self-assembly of **1**, **2** and **3** as single component SAMs has been studied by Scanning Tunneling Microscopy (STM). These results have been confirmed with detailed studies by Cyclic Voltammetry (CV), and Fourier Transform Infrared Reflection Adsorption Spectroscopy (FT-IRRAS).

On Au(111), undecanethiol (**2**) forms a densely packed SAM showing a commensurate (√3×√3)R30° hexagonal lattice with respect to the Au(111) surface (Fig. 5.3-a). We also observed the typical c(4√3×2√3)R30° (or c(4×2)) superstructures of this hexagonal lattice. It has been previously observed that this superstructure is extensively formed upon sample annealing (see session 5.3.3).

Nearest neighbours in the (√3×√3)R30° structures are 0.5 nm apart; moreover, all molecules in the lattice exhibit the same contrast in the STM images. Previous work revealed four levels of brightness associated with the c(4×2). This variation in the image contrast has been ascribed to the different orientation adopted by the upper methyl groups.

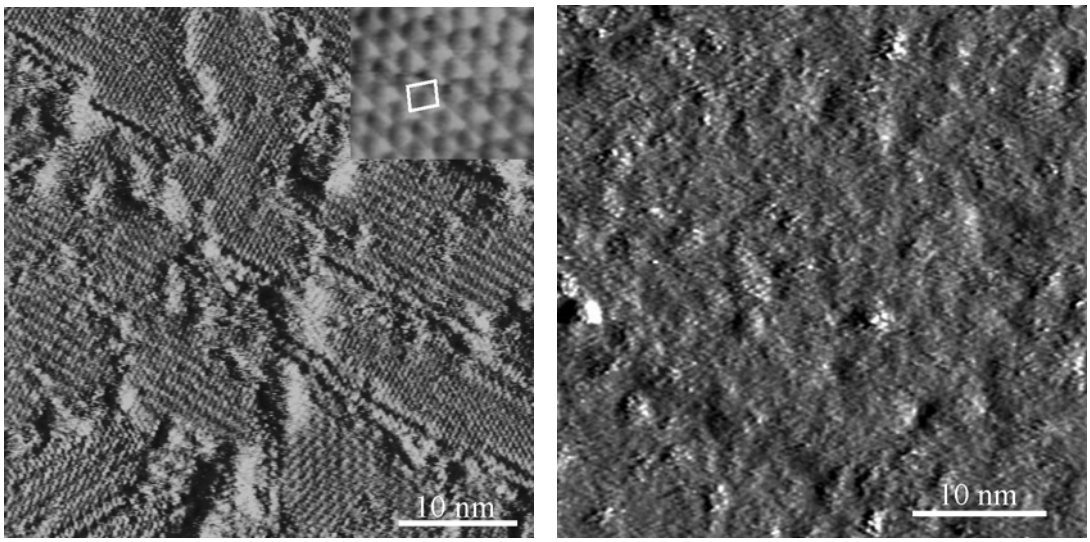

a) **b)**

Figure 5.3: a) Mono-component SAM of **2** (undecanethiol) SAM; Average Tunneling Current, It= 15pA, Bias Voltage, V= 750mV. Inset: SAM of **2** unit cell (√3×√3)R30°. **b)** Mono-component SAMs of **1;** It= 20pA; V= 999.4mV.

Conversely, molecules **1** and **3** do not form single-component, densely packed SAMs as shown in the STM image of a mono-component SAM (Fig. 5.2-b and Fig. 5.3). CV, FT-IRRAS and STM measurements provided evidence for the formation of a SAM of **1** and **3** on the Au(111) substrate.

Although it has never been possible to achieve a good molecular resolution above SAM of **1** (Fig. 5.2-b), we could observe ordered domains of molecule **3**. However, such ordered molecular assembly is hardly formed on this SAMs and only few ordered domains are found over the same substrate, which are often surrounded by large noisy areas, possibly indicating a lack of molecular lateral assembly. The molecular lattice found in Fig. 5.3 for molecule **3**, is similar to the one observed for alkanethiols on gold $(\sqrt{3}\times\sqrt{3})R30°$. This structure can be attributed to an assembly where the major intermolecular interactions is of van der Waals type between the alkyl chains, therefore this hexagonal packing is promoted by hydrophobic interactions rather than H-bonding between the amide units.

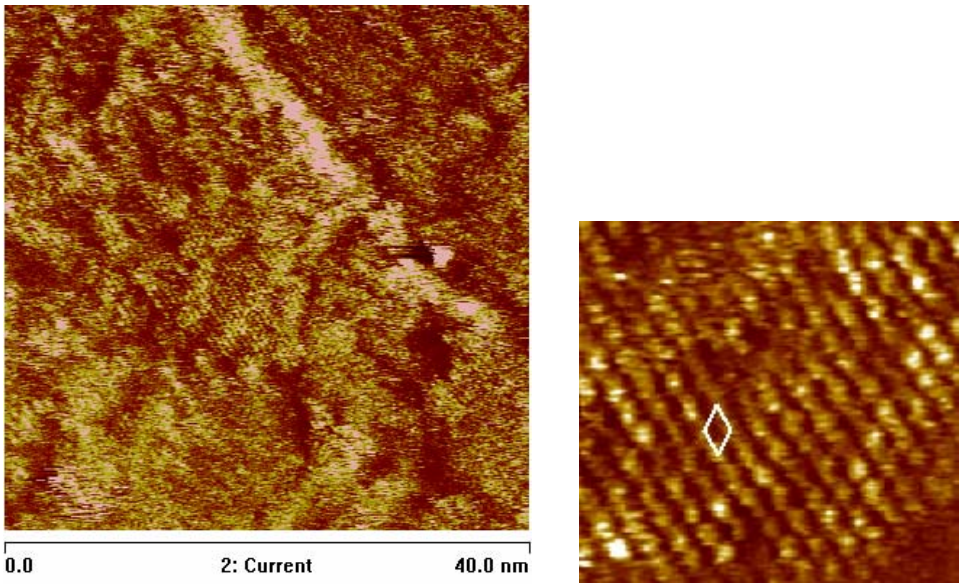

A) **B)**

Figure 5.3: A) and b) STM images of mono-component SAM of **3**: **B)** unit cell parameter a= (0.55 ± 0.05)nm; b= (0.52 ± 0.05)nm; α = 58° (It= 1.5pA; V= 1309mV).

Cyclic Voltammetry measurements also confirm the presence of the binding of molecules **1** and **3** through the formation of Au-S bond.

The experimental evidence for the covalent binding of molecules **1** and **3** is presented in Fig. 5.4 and Fig. 5.5 respectively, where the reduction peak found at -1.05 Volt indicates a

desorption process induced by the Au-S reduction and cleavage (see section 2.2). The reduction potentials for **1** and **3** are the same within the experimental error. In fact the two molecules differ only in the functionalization of the ω position making the assembly of the two molecules near the Au-S binding site rather similar. Binding can be improved by increasing the solubility of the two compounds, by adding dichlorometane or chloroform in the ethanolic solution. We also observed that in presence of a weak acid like acetic acid binding is slightly improved, probably because the acid decrease the strength of the H-bond between amide units in solution.[35] Unfortunately, despite repeated attempts, permeability experiments demonstrate that a high density of defects is present over the SAM of **1** and **3**.

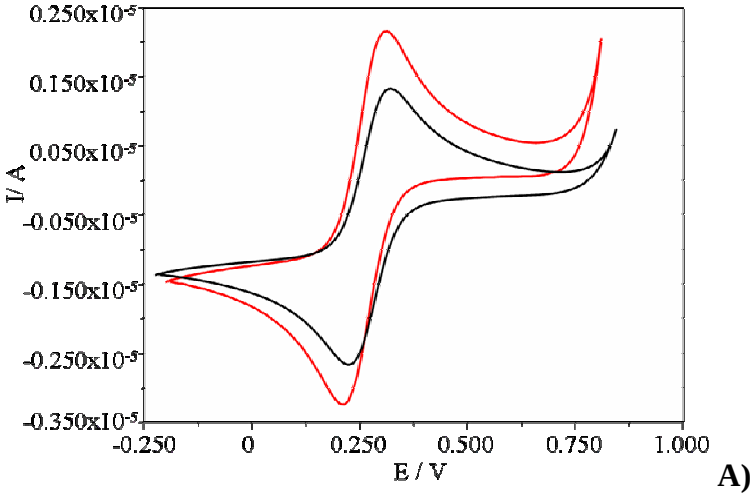

Figure 5.4: Mono-component SAM of **2**: **A)** CV plots of a SAM of **1**, 3 nights incubation in: 1mM solution in degassed ethanol solvent. ($K_3Fe(CN)_6$ 1mM, KCl 1M, 50mV/s); **B)** CV plots of a SAM of **1**, 1 night incubation in 1mM solution in ethanol solvent (red curve: $E_{Reduction}$= (-1.03±0.05)V; Width= 0.05V; 0.5 M KOH, 100 mV/s).

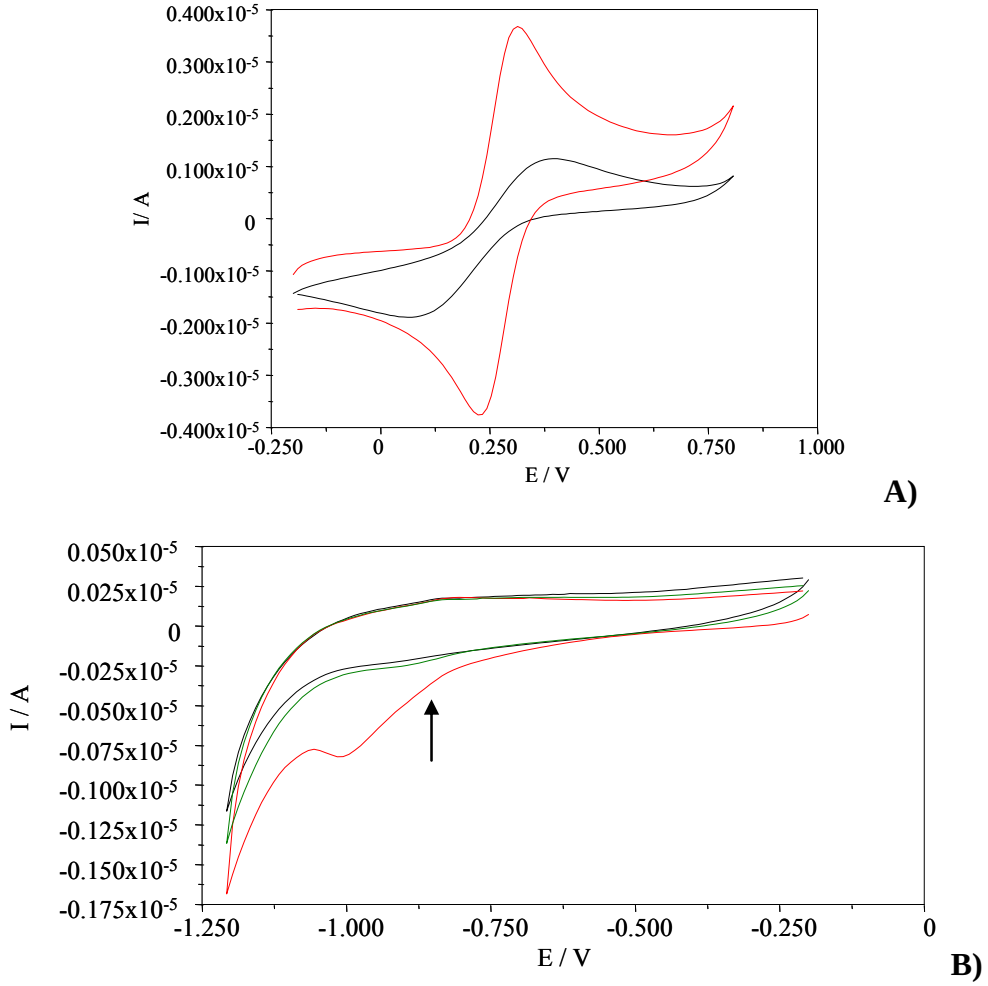

Figure 5.5: Mono-component SAM of **3**: **A)** CV plots of a SAM of **2**, 4 nights incubation in: 1mM solution in ethanol solvent containing 0.5 M of CH_3COOH. ($K_3Fe(CN)_6$ 1mM, KCl 1M, 50mV/s); **B)** CV plots of a SAM of **2**, 1 night incubation in 1mM solution in ethanol solvent (red curve: $E_{Reduction}$= (-1.00±0.06)V; Width= 0.01V; 0.5 M KOH, 100 mV/s).

We tried to improve the packing in those SAMs either by changing the solution solvent (dichlorometane, chloroform and ethanol), the temperature of incubation (from 40°C to 60°C, temperature higher than 70°C could induce the Au-S bond cleavage) or performing post annealing treatments (50°C- 60°C).[9, 36, 37] In none of the cases we could improve the molecular packing above the SAM therefore decreasing the defects concentration (for details see appendix to the chapter, table 5.1)

The packing problem does not arise from the presence of a disulfur on molecules **1** and **3**. In fact, it is well known in the literature that disulfide derivatives (R-S-S-R) bind the gold surface like the correspondent thiolated compound (R-S-H). However it is important to stress

the following point: as the assembly process is kinetically controlled, and given that disulfides are easily formed when intermolecular interactions are strong enough, the assembly process of a disulfide is slower than in the case of a free thiol. In fact, disulfides diffuse as dimers and as intermolecular interactions are quite strong they easily form aggregates, the binding kinetic constant decreases. We also found that the binding of the disulfide derivative of molecule **2** form SAM with the same lattice parameters as for the thiolated molecules. The as found molecular lattice is identical to the one formed by the undecanthiol and showed the characteristic distance between the nearest Au-S-R binding sites of 4.9 Å. This distance is an evidence of a cleavage in the S-S bond.

We concluded that the energetic unbalance between different intermolecular interactions prevents the formation of long range crystalline domains for molecules **1** and **3**. In fact, various interactions are involved in the SAM formation: i) covalent binding between Au and SH group favouring the formation of a commensurate ($\sqrt{3}\times\sqrt{3}$)R30° molecular lattice with a binding site distance of 0.49 nm; ii) van der Waals interactions among the alkyl chains that are optimized when the chains adopt an all-trans conformation with a lateral inter-chain distance of ~0.4 nm, the optimization of those interactions is also the reason why in alkylthiol monolayer, according to the binding distance dictated by the gold lattice (0.5nm), the alkyl chain have to tilt at 30° with respect to the surface normal; iii) hydrogen bonding between the amide units that is optimized when the N-O distance for the amino N-H···O=C hydrogen bond is 0.28 nm[38, 39]; (iv) and for molecule **1** the π-π interactions of the pyridine moiety which are maximized for a distance between aromatic rings of about 0.33 nm. Small variations in the optimal distances and angles for each specific interaction lead to a change in the total energy of the system. The unbalanced interactions in SAMs of **1** and **3** prevent the formation of an ordered assembly as revealed by the facility for the redox couple to permeate the SAM (Fig. 5.4 and 5.5). An interesting study reported by Allara and co-authors, confirmed this observation. They found that highly dipolar tail groups, as in the case of amide groups embedded in alkyl chain, might induce chain orientation disorder if an ordered array engendered a large unfavourable electrostatic interaction.[10] In particular they observed that a non linear behavior of the molecular assembly was induced by varying the number of the amide unit embedded in the alkyl chain. Ordered assembly were observe for SAMs containing 1 and 3 amide units, while disordered SAMs where formed by alkylthiols bearing two amide units. The destructive interference of the amide region with respect to the

hydrocarbon ordering process can be reduced by increasing the alkyl chain length (up to 15 methylene units for only one amide unit embedded in the alkyl chain).[40]

The high density of defects in the SAM, together with the high insulating barrier originated by the long chain of **1** and **3**, are responsible for the lack in good imaging resolution by STM (Fig. 1a). The STM is a local probe designed to image the surface electronic density. In the case of SAMs, the molecular resolution has mainly been explained by a main strong contribution to the tunneling arising from the electronic density located at the S-Au bond. However a contribution from the molecular backbone to the tunneling is not excluded. Therefore, when the top layer of a molecular substrate consists of possible disordered groups, then the STM imaging process of the SAM will be disturbed and the STM images will appear poorly resolved, regardless of the packing of the underlying ordered Au-S binding sites.

Furthermore, an organic thick layer acts as an insulator for the tunneling electrons. The tunneling barrier through alkyl chains is 0.8 eV[41] and it increases with the length of the alkyl backbone. It has been observed that for SAMs containing alkyl chain longer than 13 methylene units STM imaging does not provide a good molecular resolution. We estimated a total length for the molecular backbone of the pyridine-amide of 22 Å, therefore the increase in tunneling barrier is another explanation for the noisy pictures obtained on SAM of **1** and **3**.

5.3.2 Bi-component SAMs

We attempted to improve the order at the supramolecular level in SAMs containing molecule **1** (or **3)** by co-deposition with **2**. We prepared different SAMs by incubating the gold substrates in solutions containing different molar ratios of molecules **1** (or **3**) and **2**, namely: 1/9; 3/7; 1/1; 7/3; 9/1 (see experimental procedure at the end of this chapter for details).

STM images recorded on SAMs formed from 9/1 and 7/3 (**1**/**2**) ratio exhibited a complete and selective coverage of the SAM with **1** molecules. At 1/1 and 3/7 (**1**/**2**) molar ratios, small phase segregated domains of **2** were observed while the SAM was mainly covered by disordered domains of **1** (Fig. 5.6). Unfortunately, the noisy appearance of the mono-component domains formed by **1** (or **3**), does not allow us to accurately determine the relative coverage of **1** (or **3**) and **2** above the **1**/**2** (or **3/2**) mixed SAMs.

However, the extent of mono-component domains of **2** over the SAM is lower than what would be expected considering the molar ratio in solution (e.g. remembering that each molecule of **1** bears two sulphide units, at 3/7 **1/2** molar ratios we have a solution containing 46% of the pyridine amide sulphide and 54% of undecanthiol, but the surface is mainly covered by single domains of **1**). We infer that the phase segregated domains observed for 1/1 and 3/7 molar ratio (as well as the structures observed at 1/9 molar ratio) correspond to metastable assemblies (Scheme 5.2).

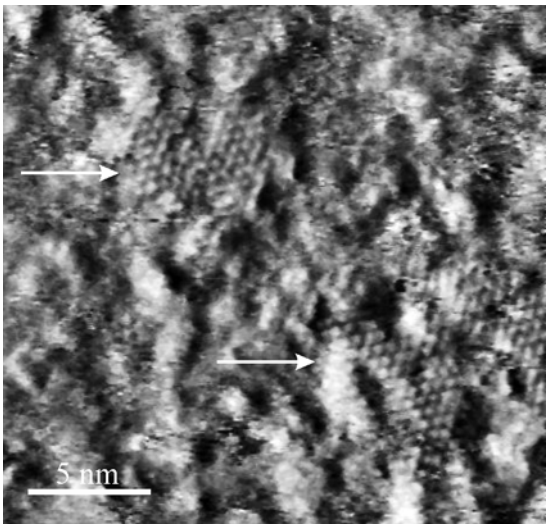

Figure 5.6: Mixed SAMs prepared by immersion in solutions containing 1/1 molar ratio of **1/2**. White arrows indicate phase segregated domains of undecanethiol. I_t= 2.8pA; V= 867mV.

These results are consistent with the definition that is given to SAMs, *i.e.* SAMs are kinetically trapped at local thermodynamic minima. The free energy of the minimum is a function of the relative coverage of the phase segregated domains and it is noteworthy that during the SAM formation the coverage ratio is mostly under kinetic control.[iii] We observed that films prepared by incubating the Au(111) substrate for one month in all the above-mentioned mixed solutions were fully and uniquely covered with **1**. Therefore, although the SAM of **1** is not densely packed, it is more thermodynamically stable than the mono-component SAM of **2**. Considering the case of an assembly process under complete thermodynamic control and, assuming a scenario characterized by a non-miscibility between

[iii] Kinetic effects determine the reaction pathway; as many local thermodynamic minima can exist, due to the possibility of metastable SAM to be formed (see session 5.2.1), kinetic factors might lead the system toward a minima rather than another even if the latter is thermodynamically more stable.

the two components, the SAMs formed show only one phase of the molecule generating the more energetically stable assembly. In view of the Bragg-Williams model for an ideal solution, and according to its application to bi-component SAMs, this case is reflected by two non-interacting molecules, therefore by a positive and high interaction parameter (scheme 5.2).

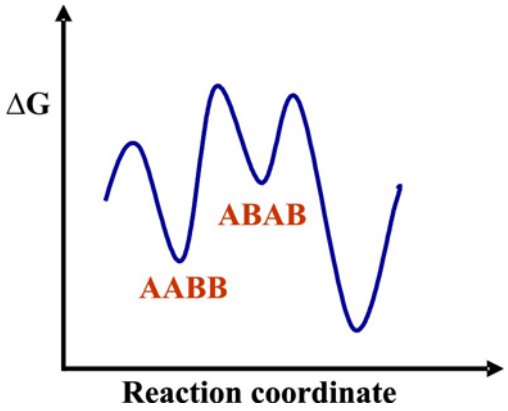

Scheme 5.2: The cartoon indicates metastable assemblies formed by incubating the substrate in a bi-component solution of A and B. It is assumed that the interaction parameter, is high and positive; therefore, AABB and ABAB represent metastable assembly composed of phase segregated mono-component domains of AA and BB and, mixed domains of AB, respectively. For a high and positive value of the interaction parameter the absolute minimum correspond to a mono-component SAM.

We attribute this higher stability of the pyridine SAMs with respect to the undecanthiol SAMs, to the presence of H-bonds between adjacent amides which reduces the exchange process with the molecules in solution. Under long incubation time thermodynamically more stable domains are more likely to grow at the expense of the less stable. This phenomenon is possible because of the intrinsic dynamic character of the assembly process. In fact, the continuous exchange of molecules between the surface and the solution allows for the self-annealing of defects, i.e. reduction of domain boundaries, coalescence of etch pits, conformational relaxation of the molecular backbone, but it also leads to the desorption of metastable domains in favour of the growth of more stable domains.

Besides van der Waals interactions between alkyl chains in the self-assembled monolayers, hydrogen bonding in domains of **1** might stabilize the assembly better, which explains the highest coverage of molecular domains of **1** (or **3**) with respect to **2**. The most ordered assembly in this case does not correspond to the most stable SAM.

Considering a van der Waals interchain interaction energy of 8.6kJ/mol per each CH_2[42], an energy value of 33.5kJ/mol per H-bond[42] and π-π interaction contribution of ~12kJ/mol[43], we can roughly estimate for the pyridine-amide mono-component domain a stabilization energy 54.1 kJ/mol greater than in the undecanthiol assembly. Such different energetics most likely drives the final composition of the SAM to be different than that of the deposition solution.[29, 43][iv]

Interestingly, the 1/9 (**1**/**2**) molar ratio SAMs display striped domains, which are peculiar to this range of molar ratios in solution. Their relative coverage within the SAM depends on the incubation time. After two days of immersion these SAMs exhibited striped domains, whose unit cell (Fig. 5.7) contains 2 molecules: bigger and brighter spots are located at the edges of the unit cell, while a dark spot is found at the unit cell centre. Similar domains are typically found in mono-component SAMs formed by alkanethiols exposing a head-group able to form hydrogen bonds, as in the cases of 1-mercaptoundecanoic acid[44-46], mercaptopropionic acid[47], and 1-mercapto-2-propanol[48]. In the latter example, the authors explained these structures in terms of rows of hydrogen bonded molecules alternated with rows of non-H-bonded molecules.

[iv] The van der Waals interaction energy of a methylene group with its neighbours within a SAM in a vacuum is derived from the heat of sublimation (ΔH_{sub}) of n-alkanes versus chain length (taken from NIST database: http://webbook.nist.gov). Plotting ΔH_{sub} of n-alkanes as a function of n-alkane chain length yields a slope whose value is the van der Waals interaction energy per methylene unit. An estimate for the stabilization due to individual van der Waals interactions of the methylene matrix is 8.6 kJ/mol per $-CH_2-$. While these values are referenced to gas phase, they do provide a reasonable estimate for the relative energetic values of this system. The interaction energies in a series of N-methylamides of the formula C_nH_{2n+1}-CONHCH3 (n=9, 11, 13, 15) were reported before.

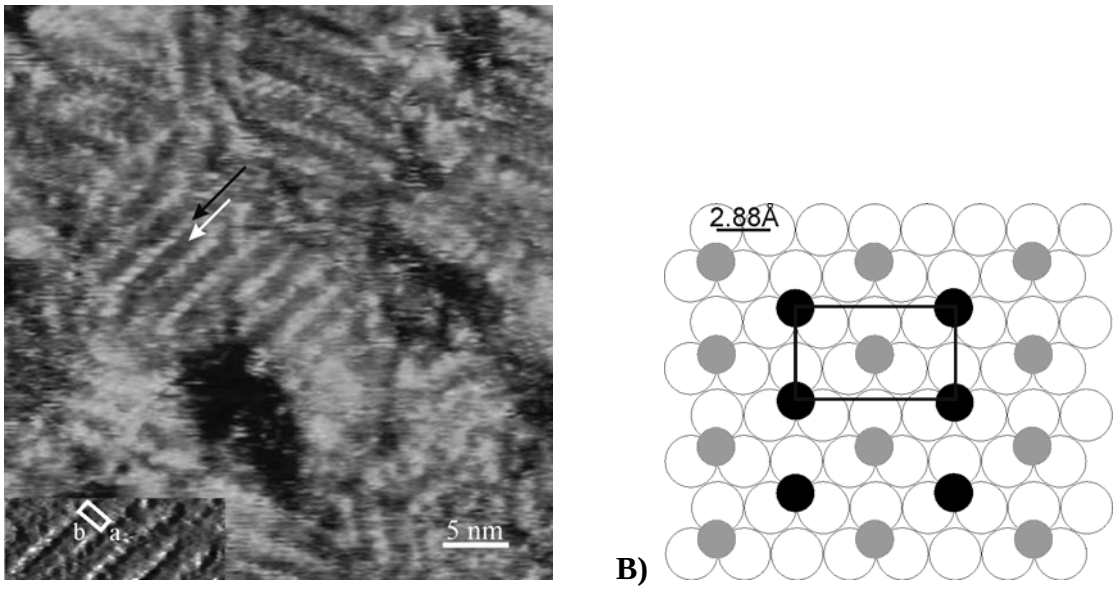

Figure 5.7: A) SAMs formed after two days of incubation in solutions containing 1/9, **1/2** molar ratio. Inset: unit cell parameters: a= (0.53±0.05) nm; b= (1.2±0.05) nm; α=84°±5°, Area= (0.63±0.1) nm^2 this lattice parameters possibly indicating a commensurate lattice with a unit cell equal to ($2\sqrt{3}\times\sqrt{3}$), where the gold lattice parameter is equal to 2.88 Å. The black arrow indicates a row of molecules **1**; the white arrow indicates a row of undecanethiol molecules. I_t= 10pA, V_t= 750mV. **B)** Schematic of a possible commensurate molecular lattice which would reflect the unit cell parameter found in **A)**: black circle indicates the pyridine-amide derivative (molecule **1**); grey circle indicate undecanethiol molecule.

Since it has never been possible to observe ordered mono-component SAMs of molecule **1**, it is possible to rule out that the bi-dimensional structures shown in Fig. 5.7 are formed by ordered linear arrays of **1** only. Furthermore, although it was possible to detect the darkest molecular row in the striped domains, its imaging resolution is very poor, indicating either that molecules in this row are not conducting as much as those aligned in the brightest row, and/or that the darkest row contains much shorter molecules. The previous considerations lead us to the conclusion that the darkest row is composed of an ordered alignment of **2**. This evidence was further supported by FT-IRRAS measurements providing evidence for the presence of both molecules on the Au(111) surface (Fig. 5.16).

After 5 days of incubation, the striped domains appeared as shown in Fig. 5.8. The unit cell parameters (Fig. 5.8-B) are similar to the c(4×2) lattice parameters found for alkanethiol SAMs, indicating that the Au-S covalent interaction promotes an assembly commensurate with the Au(111) lattice. The appearance of zig-zag molecular array (see black arrow, Fig.

5.8-B) is in accordance with the structure observed in mono-component SAMs formed by molecules having amide moieties placed within the molecular chain.[29, 49] From FTIR studies, Clegg and co-authors provided evidence for the existence of intermolecular H-bonds in SAMs containing amide units along the molecular chain.[33, 40] Both molecular patterns seen in Fig. 5.7 and Fig. 5.8 can be found in mixed SAMs formed from the 1/9 (**1**/**2**) solution, although the striped pattern showed in Fig. 4 was most commonly observed.

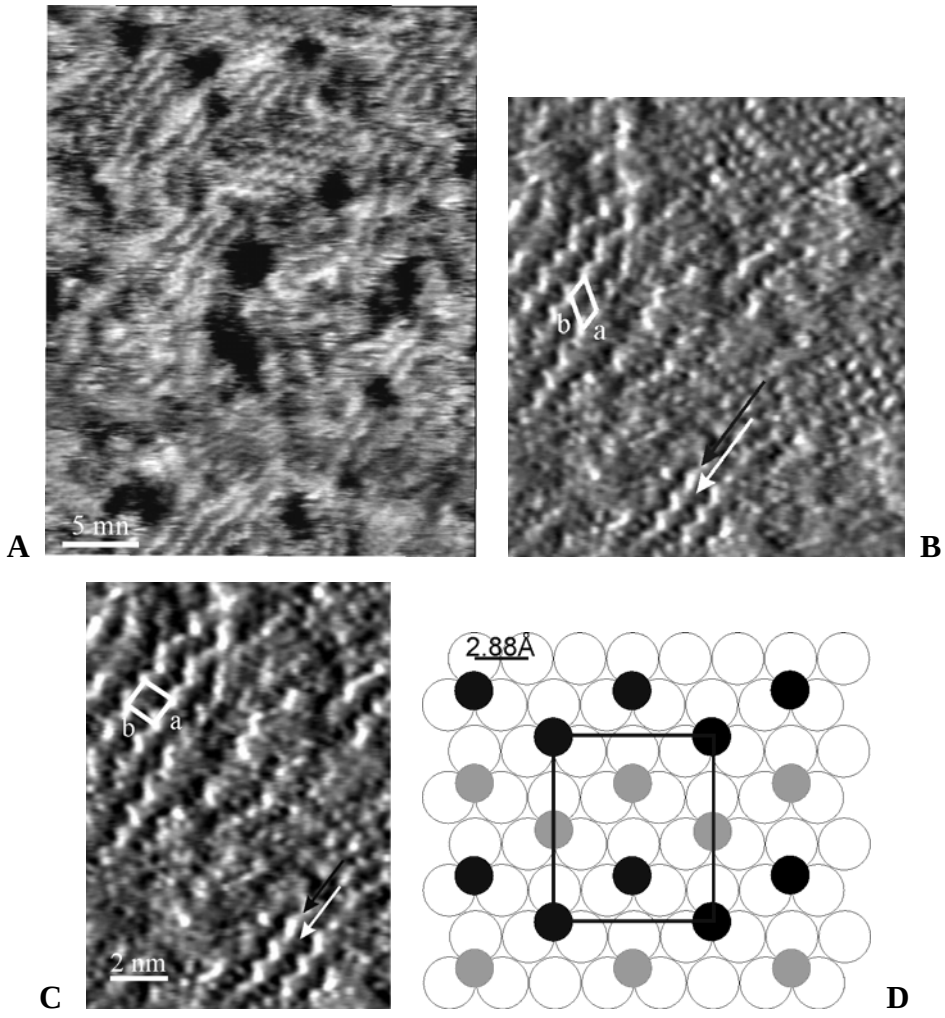

Figure 5.8: A) Height contrast image **B)** and **C)** current contrast image of SAMs formed after 5 days of incubation in solutions containing 1/9, **1/2** molar ratio. **B)** Oblique unit cell; **C)** Square unit cell parameters: a= (1.1±0.1) nm; b= (1.1±0.1) nm; α=92°±5°, Area= (1.1±0.2) nm^2. I_t= 2.17pA, V_t= 810mV. **D)** Schematic drawing of a possible commensurate molecular lattice which would reflect the unit cell parameter found in **C)**: black circle indicates the pyridine-amide derivative (molecule **1**); grey circle indicate undecanethiol molecule.

Fig. 5.8 depicts the proposed molecular packing in the striped domains of Fig. 5.8-A)-B). In this architecture the sulphur head-groups bind at a three-fold hollow site of Au(111), as typically reported in literature, although other binding S-Au binding site have been proposed.

The two molecular lattices seem not to differ in terms of binding sites although, according to the model presented in Fig. 5.7-B and Fig. 5.8-C, the pyridine-amide derivative align along two different directions of the Au (111) surface crystal lattice. Therefore, the difference between the two structures might arise from distinct interchain interactions stabilizing the molecular patterning. In fact, in the structure shown in Fig. 5.7-B the pyridine amide aligns exactly on a line, while in Fig. 5.8-C it features the characteristic zig-zag pattern.

The main difference between the two molecular packing is the arrangement of the first nearest neighbours of molecule **1**: in both structures there are 4 undecanthiol molecules as first nearest neighbour but their distribution around the pyridine derivative is different. Therefore, while keeping the same lattice binding sites, the hetero-molecular interactions vary and the zig-zag patterning seems to give more stable assembly than the linear patterning.

As the structure found in Fig. 5.8 is most commonly observed, we consider that the zig-zag patterning adopted by molecule **1** along a row might stabilize better the H-bond interactions than the linear patterning.

To our knowledge this is the first example of completely miscible bi-component domains chemisorbed on a metallic surface forming SAMs. The pyridine-amide rows (black arrow in Fig. 5.7-B are separated by thinner rows of undecanethiol (white arrow in Fig. 5.7-B), making it possible for the pyridine-amide unit to emerge vertically from the overall SAM. The undecanethiol row laterally stabilizes the **1** row through van der Waals interchain interactions. Alternating rows of apolar and polar components might stabilize the mixed monolayer decreasing the electrostatic interactions between adjacent H-bonded, polar rows.

Since the striped domains were observed only at a 1/9 (**1**/**2**) molar ratio, it is possible to conclude that the striped phase are most likely kinetically trapped rather than equilibrium structures.[29] In particular, the diffusion rate of the two molecules on the surface and the dynamic adsorption-desorption processes leading to the final assembly, are notably affected by the relative concentration of the two compounds in solution and by their molecular structure. The kinetic control above the formation of mixed crystalline domains is also shown by the observation of a high coverage of pyridine-amide on samples incubated in the

1/9 (**1**/**2**) solutions for over one month. However, our results demonstrate that it is possible to trap the system in a local thermodynamic minimum containing striped domains by achieving a kinetic control over the self-assembly process and, in particular, by varying the concentration of the two molecules in solution and the incubation time.

In order to ascertain the role played by the hydrogen bond over the formation of the striped domains we prepared mixed SAM from solution containing different molar ratio of undecanthiol and the methyl-amide terminated derivative of molecule **1** (molecule **3**). In particular, SAMs formed from solutions containing 1/9 (**3/2**) molar ratio, show similar striped features even if their relative coverage on the surface with respect to the undecanethiol domains is minor. We found both linear stripes and alternated striped domains of molecule **1**, shown in Fig. 5.7 and Fig 5.7., respectively. Furthermore, the hexagonal lattice formed by the mono-component SAM of **3** (Fig. 5.3) once more confirms that the striped pattern cannot be attributed neither to single component SAM of **2** or **3**. The 1/9 **1/2** and **3/2** mixed SAMs differ in the relative coverage of the striped domains. As previously stated, the contribution of all possible interchain interactions has to be considered for predicting and interpreting the final assembly. We attribute the different behaviour of the two amide derivative to the contribution of the π-π interactions between pyridine units to the stabilization of the mixed domain.

However, the evidence of the presence of striped domains also in mixed SAMs of **3** and **2** confirms the contribution engendered by the hydrogen bonds to the alignment of the amide derivatives along the stripes main axis. It is interesting to note the presence of both the linear and the alternated striped domains also for the mixed SAMs of **2** and **3**.

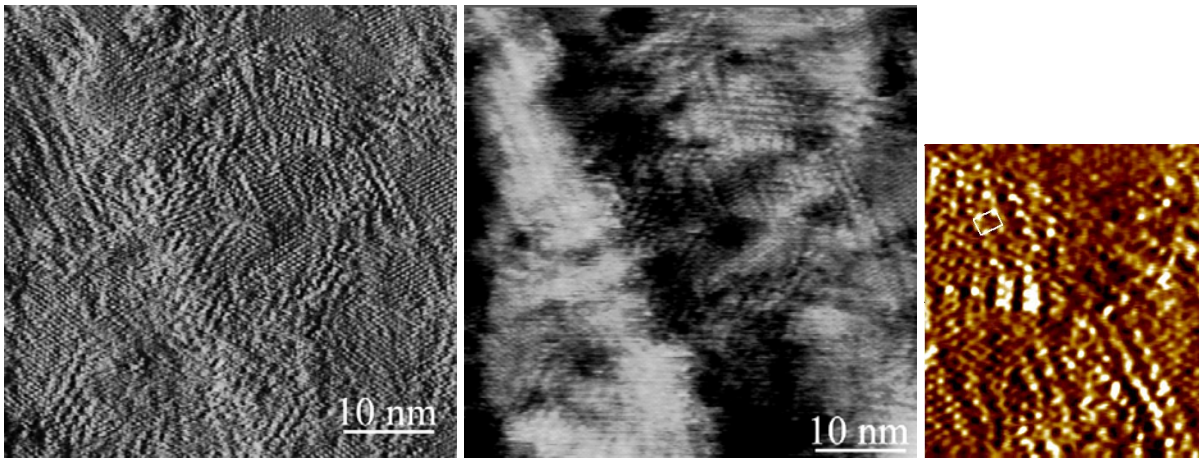

A) **B)** **C)**

Figure 5.9: Mixed SAM formed from 1/9 (**3/2**) molar ratio after 10 days of incubation: **A)** current contrast image; **B)** height contrast image; **C)** Unit cell parameters: a= (1.2±0.05) nm; b= (0.9±0.05) nm; α= 89°±5°; Area=(1.1±0.1)nm^2. (I_t= 3.0pA, V_t= 780mV)

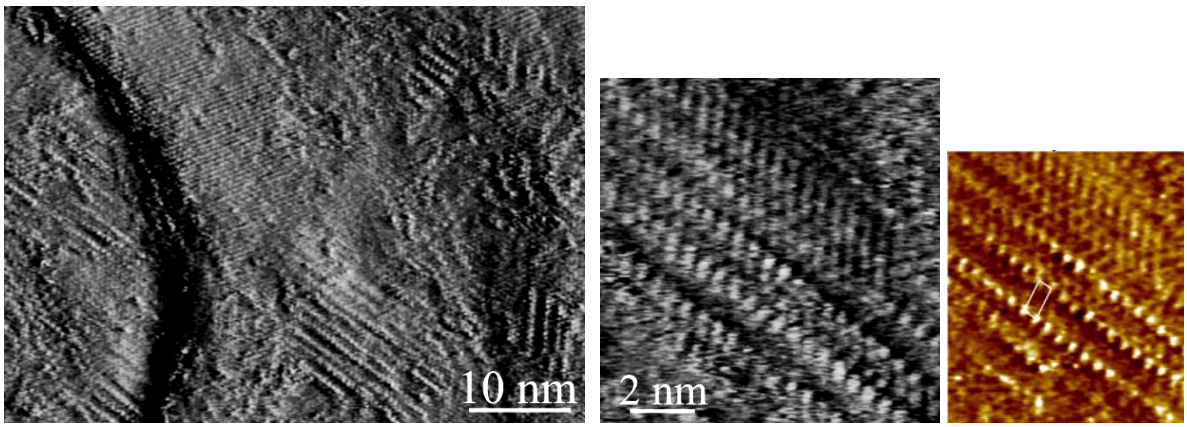

A) **B)** **C)**

Figure 5.10: A) Mixed SAM formed from 1/9 (**3/2**) molar ratio, after 5 days of incubation; **B)** zoom on A); **C)** Unit cell parameters: a= (1.3±0.05) nm; b= (0.57±0.05) nm; α= 101°±5°; Area= (0.72±0.1) nm^2. (I_t= 7.0pA, V_t= 810mV)

Previous studies have shown that in mono-component SAMs of alkyl-amide derivatives, molecules preferentially align along the short unit cell axis to optimize the formation of intermolecular hydrogen bonds. We observed that striped domains in both kind of sample (**2/3** and **1/2**) are only a few nm wide, perhaps because of their metastable nature, and their main growth direction lies on the main stripe axis, indicating that the major contribution to the total energy arises from the intermolecular interactions among molecules

aligned along the rows. The high directionality of the assembly and the detected nearest neighbour distance of ~4.8Å between molecules **1** in a row, indicate that the observed stabilization arises from the formation of H-bonds between the amide units. In view of the confinement of molecules **1** along the rows, the pyridine functional groups are exposed outside the SAM, thereby making it possible to address most easily such a functional group (Fig. 5.11). Moreover, in this position the pyridine groups do not experience the steric constrains present in the densely packed underlayer, and thereby they might be used as specific site for the coordination of Zn porphyrins.

A)

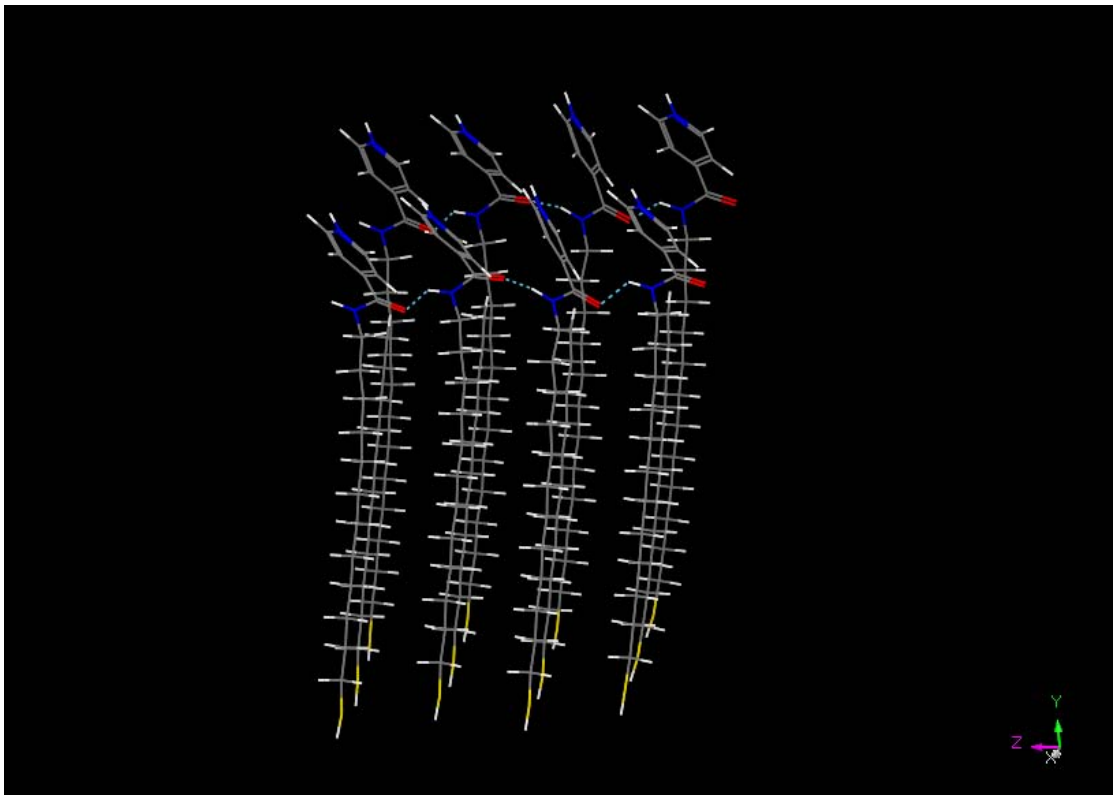

B)

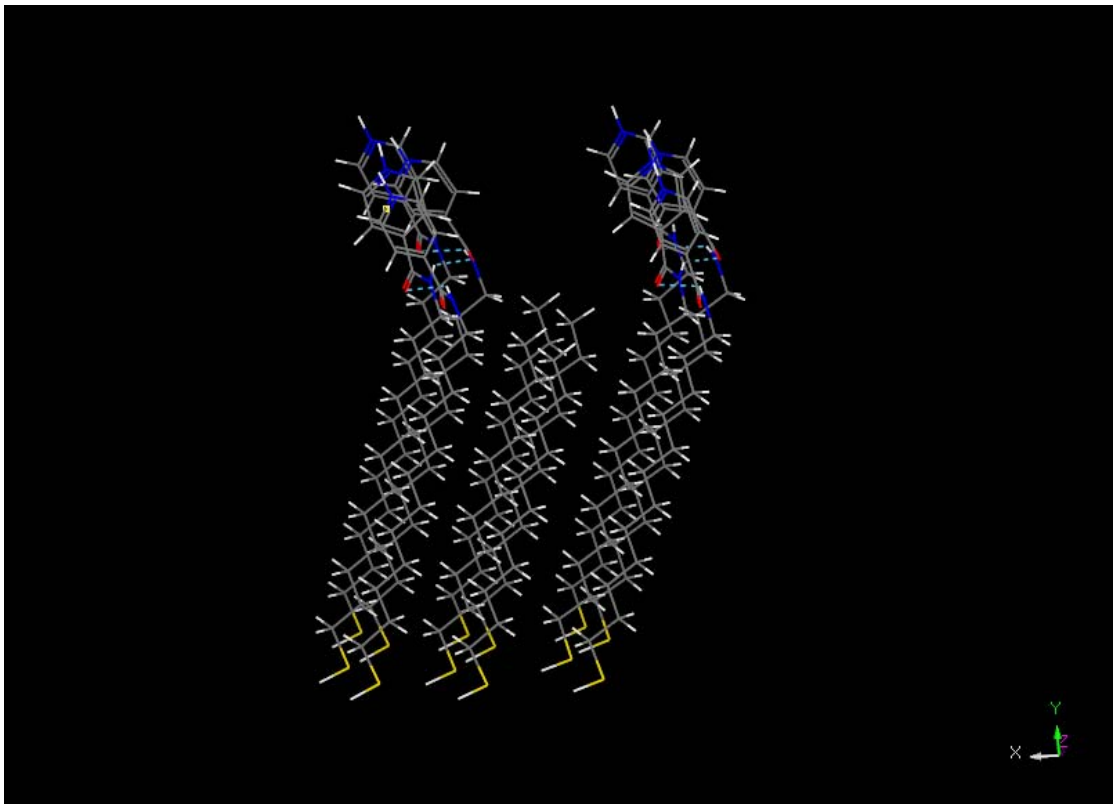

Figure 5.11: A and **B**: side view of the possible arrangement of molecules **1** and **2** in a mixed, striped domain. The pictures show that the alternated pattern of molecule **1** along a row in a striped domain allows the formation of intermolecular H-bond along the row. The model represents only an attempt made to ascertain the presence of H-bond along an alternated pattern, however the energy minimization should not be considered as arising from a rigorous calculation.[38][v]

5.3.3 Striped domains and c(4×2) superstructure

In this paragraph we address the difference between the c(4×2) pattern typically found in alkanethiol SAMs and the alternated striped pattern found in the **1/2** mixed domains. While the structures shown in Fig. 5.7 are quite peculiar for the mixed SAMs, the alternated patterning might induce to think to about a c(4×2) structure rather than a 1:1 mixed domain. In addition to the (√3×√3)R30° base lattice formed by the adsorbate overlayer, several

[v] The amide group adopts a similar hydrogen-bonded arrangement in almost all unstrained systems. The preferred N-H····O bond angle is zero degrees. The torsional barrier associated with a distortion from linearity is modest (>0.1-0.2 kcal/mol). The N-O bond distances bond tends to fall in a narrow range around 2.8Å.

superlattice conformations have been observed in alkanethiol SAMs. These are attributed to different orientations of the alkyl chains of the adsorbate molecules within the monolayer. The typical superlattice commonly found in alkanethiol SAMs corresponds to c(4×2) structure which consists of a rectangular unit cell defined by the alkyl chains in the corner sites twisting and extending out of the film, causing them to appear topographically higher typically leading to a brighter contrast in the STM images (Fig. 5.12-C). These superlattice structures contribute to the formation of structurally different domains in alkanethiol SAMs; however, the predominating packing structures remain the (√3×√3)R30° lattice and upon sample annealing the c(4×2) tends to extent over the SAM. [50-53]

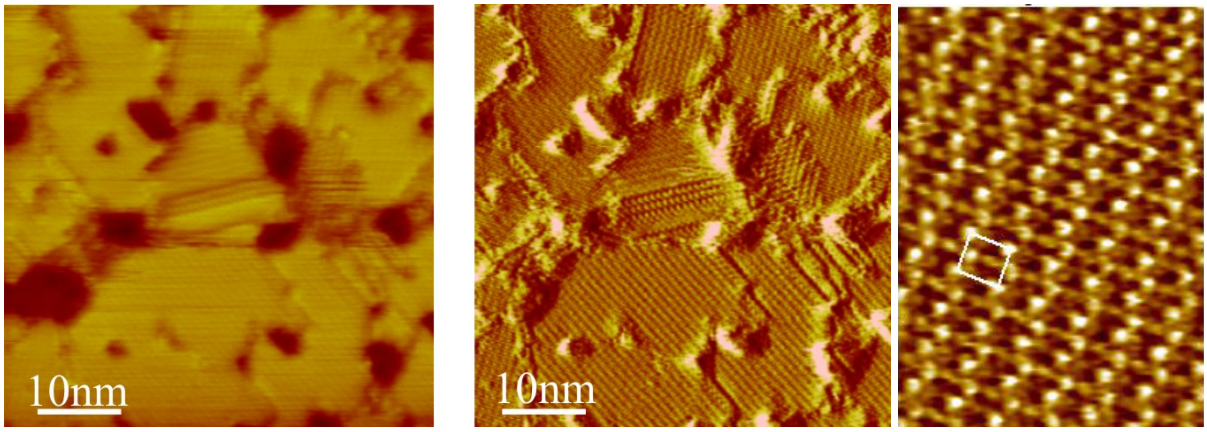

A) **B)** **C)**

Figure 5.12: Undecanthiol SAM: **A)** current image; **B)** height image; **C)** c(4×2) superlattice. Unit cell parameters: a= (1.1±0.01) nm; b= (0.97±0.01) nm; α= 93°±5°; Area= (1.05±0.02) nm^2. (I_t= 12.0pA, V_t= 770mV)

Looking carefully at the striped structures of the mixed SAM reported in this chapter we found that they are characterized by an apparent height that is higher than for the c(4×2) lattice. Pictures in Fig. 5.12, 5.13 and 5.14 compare the apparent height between subsequent rows in the different domains: (0.87±0.3)Å for the c(4×2) lattice, (1.9±0.3)Å for the linear stripes and (1.7±0.3)Å for the alternated stripes. Molecule **1** is 7 Å longer than molecule **2** and consistently, we have found that for the **1/2** mixed domain the brightest rows are higher than for the case of the c(4×2). It is worth to point out that the difference in apparent height accounts for the convolution between electronic and topographic features that contribute to

the imaging process; therefore we do not expect to find that apparent height would correspond with the difference in the chain length.

This result is consistent with H-bonded SAMs previously reported in the literature. Lewis and co-author showed that the single component SAMs of the amide-containing alkanethiol molecules adopt the same (√3×√3)R30° lattice as alkanethiol monolayers. However, the appearance of those domains in STM images is markedly different and a herringbone featured superlattice appears. Those superlattice structures are more linear than in *n*-alkanethiol monolayers owing to the presence of aligned intermolecular hydrogen bonds. It is not surprising to find the same molecular lattice for the c(4×2) superlattice and the alternated striped domains. In fact, although H-bonds induce the molecular alignment along a row, van der Waals interactions are stabilizing the lateral packing. Since our system contains long alkyl chains in both molecules (**1/2** or **3/2**), the latter interactions are identical in both molecular lattices. Therefore we conclude that, although the c(4×2) and the striped domain show the same Au-lattice/molecule registry, the striped structure previously described for mixed SAMs of **1/2** (or **3/2**) is not a superlattice of the undecanthiol monolayer.

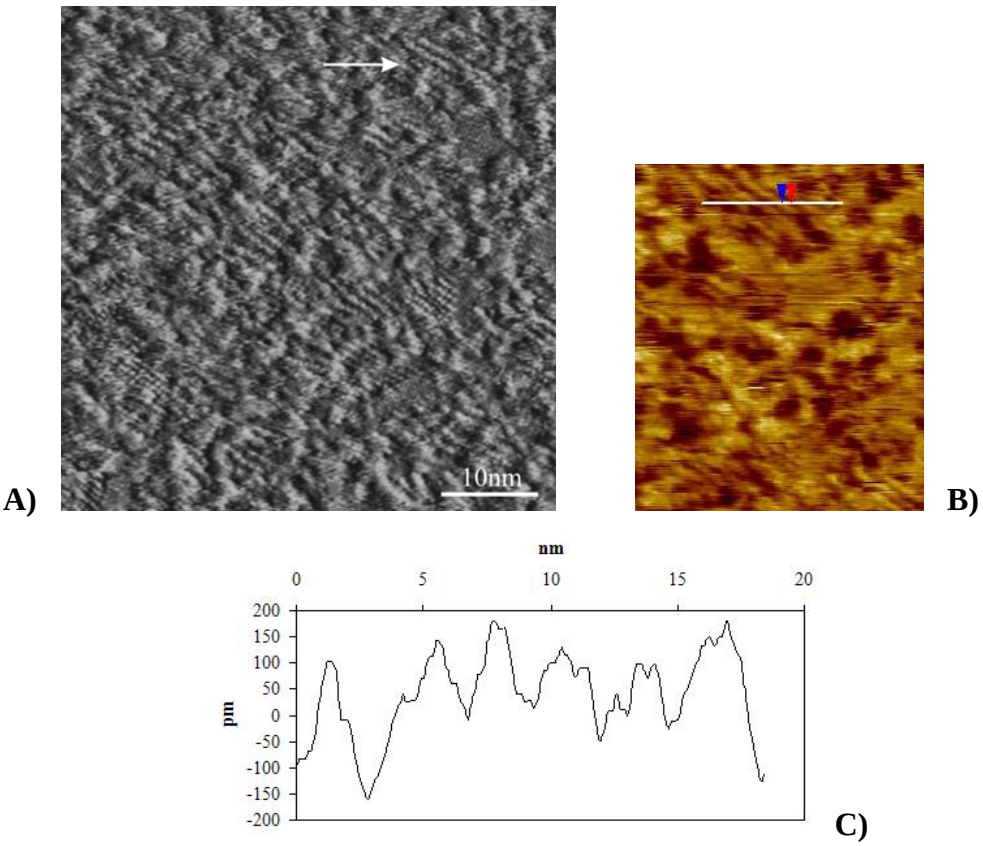

Figure 5.13: STM images of a SAM formed from a 1/9 (**1/2**) solution: **A)** Large scale current image; the white arrows indicate the striped domain taken for the line profiling; **B)** height

contrast image of the striped domain indicated by the white arrow in figure a); **C)** line profile showing the apparent height difference between two consecutive rows in an alternated striped pattern. Apparent Height difference: (0.17±0.03)nm.

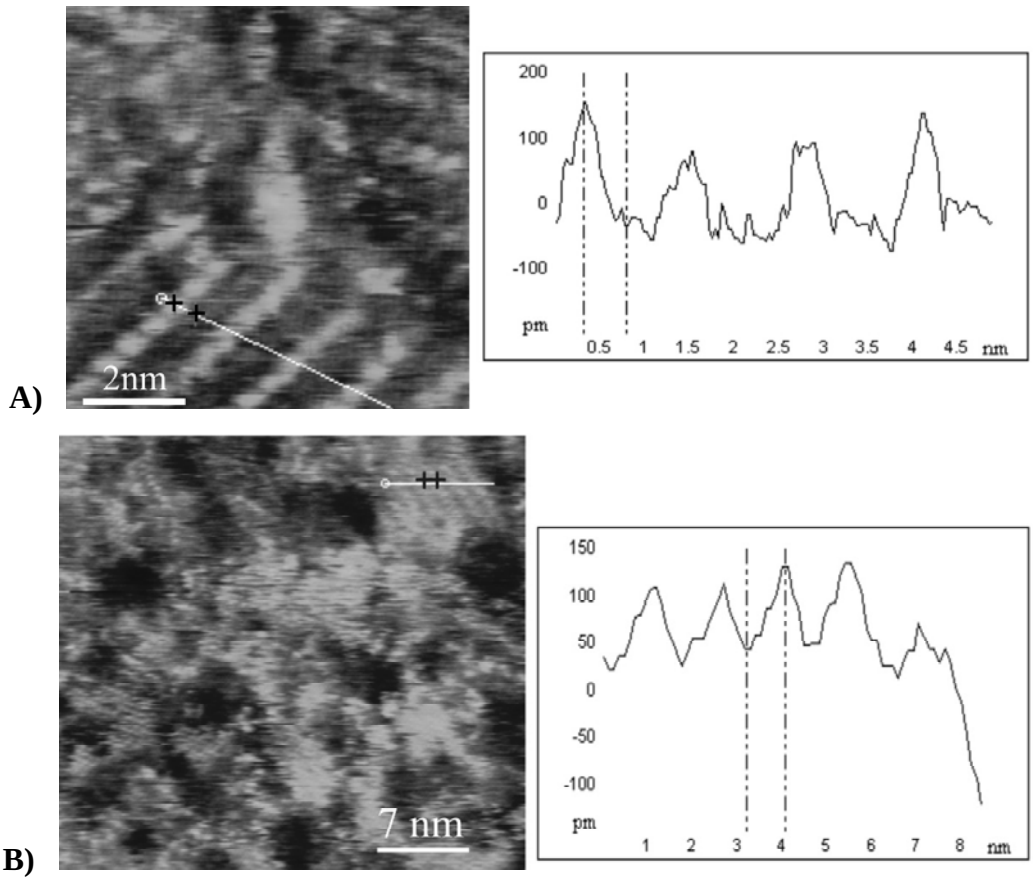

Figure 5.14: A) and **B)** STM images of a SAM formed from a 1/9 (**1/2**) solution using the same STM tip and similar tunnelling conditions in A) as in B). The line profile in A) shows an apparent- height difference between two consecutive rows of (0.19±0.03)nm. (I_t=12pA; V_t=810mV). **B)** A c(4x2) undecanthiol superstructure is shown in the right-top side of the image; the line profile indicate an apparent-height difference between consecutive molecular rows of (0.087±0.02)nm.[17] (I_t=10pA; V_t=810mV)

5.3.4 FTIR characterization

FT-IRRAS and PM-IRRAS spectroscopy of organic assembly on reflective substrates can provide information about alkyl chain orientation and order. Those factors can be deduced from the frequency (wavenumber), width, and relative intensity of the methylene

stretching bands. In FT-IRRAS peak intensities and band position are proportional to the transition dipole components perpendicular to the substrates plane as dictated by the surface selection rule. We could not derive quantitative information about chain orientation for the amide containing SAMs because of uncertainty about the conformation of the alkyl chain bearing the pyridine-amide unit. We found that in mixed SAMs of **1/2** and **3/2** the FWHM (Full Width at Half Maximum) is lower compared to the pure SAM of **1**, **2** or **3** (see Table 5.2 in the Appendix to Chapter 5).

Typical methylene stretching peaks of a closed-packed *n*-alkanethiol SAM on gold are found at 2918 cm^{-1} ($CH_{2(as)}$) and 2850cm^{-1} ($CH_{2(sym)}$). Such bands are red shifted up to 6-8 cm^{-1} compared to disordered films. In disordered SAM the methylene stretching are broad, weak and blue shifted. Contemporary a full width at half maximum of 12cm^{-1} for $CH_{2(as)}$ and 8 cm-1 for $CH_{2(sym)}$ correspond to a well ordered, all trans chains with a low dipersion of conformational states.[54-57][vi]

In fact, both a disorder packing and/or a gradual loss of linearity between peak intensity and C-$H_{(str)}$ dipole orientation, cause a weakness in peak intensity.[vii] However, the blue shifts and broadening are consistent only with disorder (see Table 5.2 in the Appendix to Chapter 5). Such blue shift of the methylene stretching frequencies and band broadening is easily recognized in the mono-component spectra of **1** and **3**, confirming the presence of a disordered SAM. Furthermore, in those SAMs it is possible to distinguish the amide II (Fig. 5.15 and Fig. 5.16) peak at around 1553cm^{-1} and 1551cm^{-1}, respectively.[58-61] In mixed SAMs of **1/2** and **3/2** the amide II band is weak. Differently from to mono-component SAMs of **2**, in mixed SAM of **1/2** (and in SAMs of **3/2**), we found a more structured fingerprint in the region between 1700cm^{-1} and 800cm^{-1}, confirming that both molecules are present in the **1/2** SAM (and in SAMs of **3/2**).[62]

[vi] It is well known that the stretching mode of the methylene units is very sensitive to the phase state in which they are measured. The oscillator strength of the C-H stretching decreases by a factor 2-3 from crystalline to melted states. In crystalline bulk the band wavenumber of the $CH_{2(sym)}$ stretching is positioned at 2850cm^{-1} while the $CH_{2(asym)}$ is found at 2920cm^{-1}. In the liquid-like state $CH_{2(sym)}$ and $CH_{2(asym)}$ stretching modes are shifted toward higher wavenumbers of about 2-5cm^{-1} and 2-3cm^{-1}, respectively.

[vii] The lack of linearity of the peak intensity and the CH dipole orientation, found in particular for very short alkyl chains, has been attributed to an optoelectronic interaction between methylene dipoles and the metal electrons at polarizable interface.

Consistently with previous studies of amide containing SAMs, we found the N-$H_{(str)}$ (amide A) at ~3300cm^{-1} and the C=$O_{(str)}$ (amide I) at ~ 1640cm^{-1} either absent or very weak and broad in the SAM spectra of the mono-component SAMs of **1** and **2** and in the mixed SAM of **1/2** and **3/2**. This evidence indicates that the amide groups is oriented with C=O and N-H bonds near parallel to the substrate plane. In fact according to surface selection rules, these weak intensities can be attributed to a vibrational transition dipole moment associated to the C=O and N=H bonds oriented nearly parallel to the gold substrate.[viii] Unfortunately, the noisy spectra found in the region between 1200 and 1700cm^{-1}, makes it difficult the attribution of the amide II peak (N-$H_{(ipb)}$, usually found at 1560cm^{-1}) . In fact, a high intensity of this peak together with the weakness or absence of amide A and I peaks, would further support the fact that the amide II dipole is probably oriented perpendicularly to the substrate, and therefore that the H-bond direction is parallel to the gold substrates as modelled in Fig. 5.11.[63, 64] For a low absorbing film at low wavenumber region between 1420-1720cm^{-1}, water absorption renders the attribution of the vibrational modes to the respective peaks difficult. Furthermore, at wavenumber lower than 1350cm^{-1} absorption bands of the mica substrate appear.

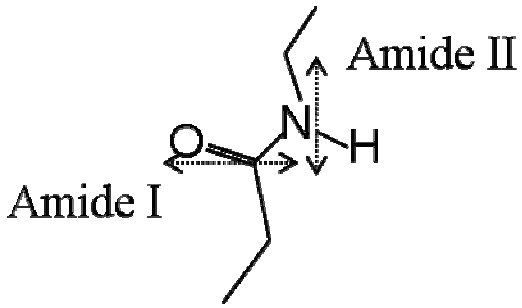

Figure 5.15: Schematic representation of the dipole moment orientation of the amide I and amide II with respect to the alkyl chain axis.[40]

[viii] The high frequency of the amide II peak is consistent with a high degree of hydrogen bonding, as the oscillator frequency follows the degree of constraint placed by an associated carbonyl on the N-H(bend) vibration.

Amide III occurs as a broad peak at ~ 1250 cm^{-1}, supporting a trans conformation as expected for a secondary amide group. The primary components of amide III are C-N(str) and N-H(ipb), both of which contain large vectors parallel to the long molecular axis. The extinction coefficient of amide III is low compared to that of amide II, accounting for decreased intensity of amide III compared to amide II.

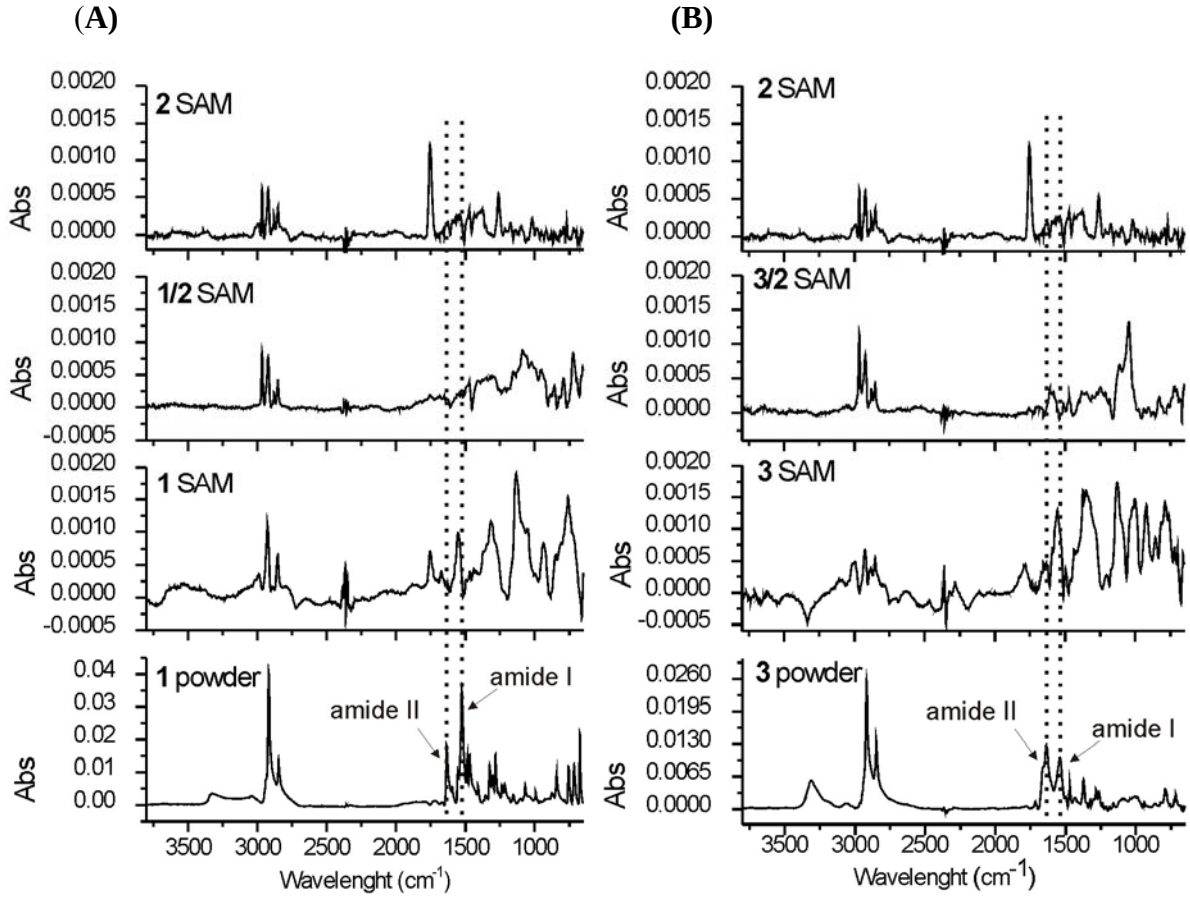

Figure 5.16: FT-IRRAS spectra of the different monolayers under study. **A)** Spectra of 1 and mixed SAM of **1/2**. **B)** Spectra of **2** and mixed SAM of **2/3**. (Interference from the ethanol used as solution solvent is present at 1754cm^{-1} especially distinguishable in the spectra of SAM of 1. (600 scans; resolution 8cm^{-1})

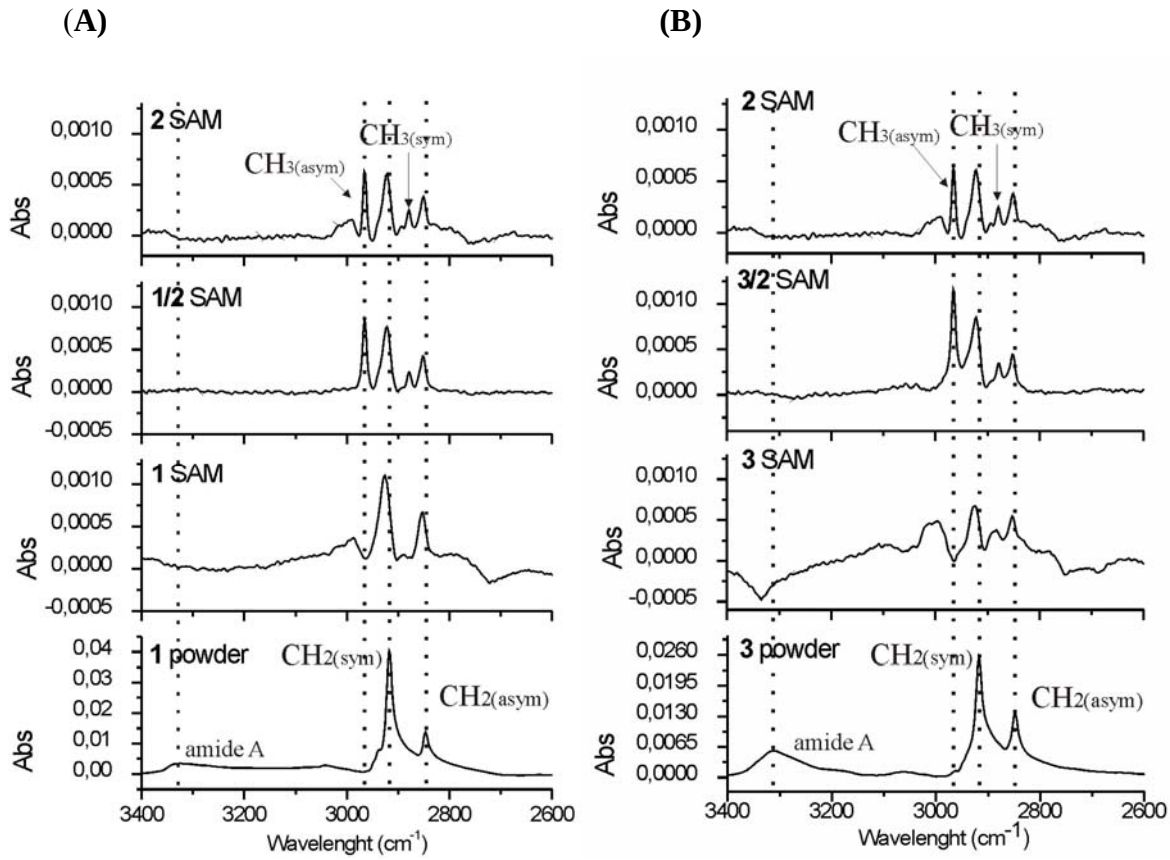

Figure 5.17: FT-IRRAS spectra in the stretching adsorption region. **A)** Spectra of 1 and mixed SAM of **1/2**. **B)** Spectra of **2** and mixed SAM of **2/3**. (600 scans; resolution 8cm^{-1})

In conclusion FTIRRAS studies show that both molecules are bound in the mixed SAM of **1/2** and **3/2**. Furthermore, a more densely packed monolayer is formed in the mixed SAM with respect to the mono-component SAM. The absence or the weakness of a broad band associated to the amide A indicates the presence of H-bonds inside the mixed SAM.

5.4 Conclusions

We have studied SAMs of amide containing alkanethiol molecules in which the formation and stability of mixed and pure films is strongly influenced by the hydrogen bond interactions. In mixed SAMs of **1/2** (or **3/2**), spontaneous phase separation occurs at high concentration of **1** (or **3**). The stability gained by the hydrogen bonding amide groups in these molecules affects the relative surface coverage within the SAM favouring a higher concentration of the amide containing molecules on the surface compared to the ratio in

solution. The hydrogen-bonding network within the mixed SAM of **1/2** (or **3/2**) contributes to the formation of linear superlattice structures. Both molecules **1** and **3** can form mixed domains leading to the conclusion that the H-bonding is somehow leading the formation of the striped domains in mixed SAMs of **1/2** and **3/2**. However, a highest density of mixed-striped domains is found in mixed SAMs of **1/2** probably because of a further stabilization of the mixed domain due to the π-π interactions between the pyridine amides units.

In summary, by exploiting the supramolecular approach in chemisorbed bi-component SAMs on Au(111) we were able to achieve a sub-nanometer control over the patterning of a surface, thereby forming multi-component crystalline domains on SAMs. This represents the first, yet fundamental, step towards the controlled spatial confinement of individual molecules or functional groups on a surface. This supramolecular multi-component array allows for the potential recognition of the target functional group and therefore may lead to the detection of single molecule properties.

5.5 Experimental procedure

The mixed SAMs were prepared by immersion of Au(111) substrates into a 2mM solution of thiolated derivatives in degassed ethanol/chloroform solutions at room temperature for 48 h. After immersion, the samples were carefully rinsed with pure chloroform and blown dry with a gentle flow of argon. For a total concentration of 2mM, the relative ratio of the two compounds in solution is indicated in the text, e.g.: a 1/9 (**1/2**) solution contain 0.2mM of disulfide **1**, and 1.8mM of undecathiol.

Appendix to chapter 5

Table 5.1: the table summarizes the results obtained performing the CV experiments described in section 5.3.1.

	Pyridine-amide	**Methyl-amide**	**Undecanthiol**
1 NIGHT INCUBATION			
Solution : 1mM in ethanol	Binding: weak. High density of defects	Binding: weak or no binding at all. High density of defects	Binding: good Low density of defects
Solution : 0.5 or 1mM in ethanol + *2.5 M CH_3COOH*	Binding: weak. High density of defects	Binding: weak. High density of defects	
Solution : 0.5 or 1mM in ethanol + *0.1 M CH_3COOH*	Binding: good	Binding: good	
Solution : 0.5 or 1mM in ethanol + *0.05 M CH_3COOH*		Binding: good	
1 NIGHT INCUBATION AND HEATING (40-50°)			
Solution : 0.5 or 1mM in ethanol	Binding: weak	No binding	
Solution : 0.5 or 1mM in ethanol + *2.5 M and 1. M of CH_3COOH*	Binding: weak High density of defects	Binding: good High density of defects	
Solution : 0.5 or 1mM in ethanol + *0.05 M CH_3COOH*	Binding: good Presence of defects but not high	High density of defects	

(All solutions were prepared in ethanol solvent where drops of CH_2Cl_2 (30-50µL) where added to help the dissolutions of the disulfide derivative.)

	Pyridine-amide	**Methyl-amide**	**Undecanthiol**
3 NIGTHS INCUBATION AND HEATING (40-50°)			
Solution : 0.5 or 1mM in ethanol + 2.5 M CH_3COOH	High density of defects	High density of defects	
Solution : 0.5 or 1mM in ethanol + 0.5 M CH_3COOH		High density of defects	
4 NIGTHS INCUBATION			
Solution : 0.5 or 1mM in ethanol with heating at 40-50°	High density of defects	High density of defects	
Solution : 0.5 or 1mM in ethanol + 0.05 M CH_3COOH with heating at 40-50°	High density of defects	High density of defects	
Solution : 0.5 or 1mM in ethanol + 0.05 M CH_3COOH NO heating	Low density of defects	Low density of defects	
INCUBATION IN $CHCl_3$ 1 NIGHT			
Solution : 1mM in $CHCl_3$ + HEATING	No binding High density of defects	No binding High density of defects	Binding: good Low density of defects
Solution : 1mM in CHC_3l + 0.05 M CH_3COOH	No binding High density of defects		
Solution : 1mM in $CHCl_3$ + 0.05 M CH_3COOH+ HEATING	No binding High density of defects	No binding High density of defects	Binding: good Low density of defects

Table 5.2 Spectral assignment of methylene and methyl vibration modes

(H= peak height; W= full-width half maximum)

	Vibration Modes			
	$CH_{2(sym)}$	**$CH_{2(asym)}$**	**$CH_{3(sym)}$**	**$CH_{3(asym)}$**
Powder of 1	2846cm^{-1} H= 0.0120 W= 10cm^{-1}	2917cm^{-1} H= 0.0387 W= 11cm^{-1}		
Powder of 2	2848cm-1 H= 0.00040 W= 7cm^{-1}	2924cm^{-1} H= 0.00100 W= 7cm^{-1}	2880cm^{-1} H= 0.00023 W= 17cm^{-1}	2965cm^{-1} H= 0.00085 W= 7cm^{-1}
Powder of 3	2848cm^{-1} H= 0.0139 W= 10cm^{-1}	2917cm^{-1} H= 0.0257 W= 3cm^{-1}	Weak and broad	Weak and broad
SAM of 1	2855cm^{-1} H= 0.0075 W= 14cm^{-1}	2927cm^{-1} H= 0.0086 W= 14cm^{-1}		
SAM of 2	2851cm^{-1} H= 0.00051 W= 15cm^{-1}	2922cm^{-1} H= 0.0079 W= 14cm^{-1}	2881cm^{-1} H=0.00040 W= 17cm^{-1}	2965cm^{-1} H= 0.00087 W= 5cm^{-1}
SAM of 3	2854cm^{-1} H=0.00069 W= 16cm^{-1}	2922cm^{-1} H=0.00068 W= 14cm^{-1}	2893cm^{-1} H=0.00029 W= 15cm^{-1}	2995cm^{-1} H=0.00031 W= 16cm^{-1}
SAM of 1/2 *(1/9 molar ratio)*	2851cm^{-1} H=0.00049 W= 12cm^{-1}	2921cm^{-1} H=0.00097 W= 12cm^{-1}	2881cm^{-1} H=0.00033 W= 15cm^{-1}	2965cm^{-1} H=0.00099 W= 5cm^{-1}
SAM of 3/2 *(1/9 molar ratio)*	2850cm^{-1} H=0.00062 W= 8.6cm^{-1}	2923cm^{-1} H=0.00132 W= 9.1cm^{-1}	2881cm^{-1} H=0.00067 W= 20cm^{-1}	2965cm^{-1} H=0.00160 W= 16cm^{-1}

References

[1] J. Huskens, M. A. Deij, D. N. Reinhoudt, *Angew. Chem. Int. Edit.* **2002**, *41*, 4467.

[2] V. Balzani, A. Credi, F. M. Raymo, J. F. Stoddart, *Angewandte Chemie-International Edition* **2000**, *39*, 3349.

[3] S. S. Jang, Y. H. Jang, Y. H. Kim, W. A. Goddard, A. H. Flood, B. W. Laursen, H. R. Tseng, J. F. Stoddart, J. O. Jeppesen, J. W. Choi, D. W. Steuerman, E. DeIonno, J. R. Heath, *Journal of the American Chemical Society* **2005**, *127*, 1563.

[4] A. A. Dameron, J. W. Ciszek, J. M. Tour, P. S. Weiss, *Journal of Physical Chemistry B* **2004**, *108*, 16761.

[5] B. Lussem, L. Muller-Meskamp, S. Karthauser, R. Waser, M. Homberger, U. Simon, *Langmuir* **2006**, *22*, 3021.

[6] D. Hobara, S. Imabayashi, T. Kakiuchi, *Nano Letters* **2002**, *2*, 1021.

[7] D. Hobara, T. Kakiuchi, *Electrochemistry Communications* **2001**, *3*, 154.

[8] R. C. Chambers, C. E. Inman, J. E. Hutchison, *Langmuir* **2005**, *21*, 4615.

[9] R. K. Smith, P. A. Lewis, P. S. Weiss, *Progress in Surface Science* **2004**, *75*, 1.

[10] C. D. Bain, G. M. Whitesides, *J. Am. Chem. Soc.* **1988**, *110*, 6560.

[11] L. Y. Li, S. F. Chen, S. Y. Jiang, *Langmuir* **2003**, *19*, 3266.

[12] J. M. Lehn, *Science* **2002**, *295*, 2400.

[13] Y. N. Xia, G. M. Whitesides, *Annual Review of Materials Science* **1998**, *28*, 153.

[14] X. M. Zhao, Y. N. Xia, G. M. Whitesides, *Journal of Materials Chemistry* **1997**, *7*, 1069.

[15] A. Kumar, H. A. Biebuyk, G. M. Whitesides, *Langmuir* **1994**, *10*, 1498.

[16] S. Imabayashi, D. Hobara, T. Kakiuchi, W. Knoll, *Langmuir* **1997**, *13*, 4502.

[17] D. Hobara, T. Sasaki, S.-i. Imabayashi, T. Kakiuchi, *Langmuir* **1999**, *15*, 5073.

[18] J. K. Schoer, F. P. Zamborini, R. M. Crooks, *J. Phys. Chem.* **1996**, *100*, 11086.

[19] R. D. Piner, J. Zhu, F. Xu, S. H. Hong, C. A. Mirkin, *Science* **1999**, *283*, 661.

[20] S. Xu, S. Miller, P. E. Laibinis, G. Y. Liu, *Langmuir* **1999**, *15*, 7244.

[21] N. A. Amro, S. Xu, G. Y. Liu, *Langmuir* **2000**, *16*, 3006.

[22] L. S. Jung, C. T. Campbell, *Journal of Physical Chemistry B* **2000**, *104*, 11168.

[23] John P. Folkers, Paul E. Laibinis, George M. Whitesides, J. Deutch, *J. Phys. Chem.* **1994**, *98*, 563.

[24] P. E. Laibinis, R. G. Nuzzo, G. M. Whitesides, *J. Phys. Chem.* **1992**, *96*, 5097.

[25] P. H. Phong, Y. Ooi, D. Hobara, N. Nishi, M. Yamamoto, T. Kakiuchi, *Langmuir* **2005**, *21*, 10581.

[26] S. J. Stranick, S. V. Atre, A. N. Parikh, M. C. Wood, D. L. Allara, N. Winograd, P. L. Weiss, *Nanotechnology* **1996**, *7*, 438.

[27] P. E. Laibinis, J. J. Hickman, M. S. Wrighton, G. M. Whitesides, *Sciences* **1989**, *245*, 845.

[28] T. Kakiuchi, M. Iida, N. Gon, D. Hobara, S. Imabayashi, K. Niki, *Langmuir* **2001**, *17*, 1599.

[29] R. K. Smith, S. M. Reed, P. A. Lewis, J. D. Monnell, R. S. Clegg, K. F. Kelly, L. A. Bumm, J. E. Hutchison, P. S. Weiss, *J. Phys. Chem. B* **2001**, *105*, 1119.

[30] L. A. Bumm, J. J. Arnold, L. F. Charles, T. D. Dunbar, D. L. Allara, P. S. Weiss, *Journal of the American Chemical Society* **1999**, *121*, 8017.

[31] S. F. Chen, L. Y. Li, C. L. Boozer, S. Y. Jiang, *Langmuir* **2000**, *16*, 9287.

[32] S. Sek, B. Palys, R. Bilewicz, *J. Phys. Chem. B* **2002**, *106*, 5907.

[33] R. S. Clegg, S. M. Reed, J. E. Hutchison, *J. Am. Chem. Soc.* **1998**, *120*, 2486.

[34] M. J. Esplandiu, H. Hagenstrom, D. M. Kolb, *Langmuir* **2001**, *17*, 828.

[35] H. Munakata, D. Oyamatsu, S. Kuwabata, *Langmuir* **2004**, *20*, 10123.

[36] F. Schreiber, *Progress in Surface Science* **2000**, *65*, 151.

[37] J. C. Love, L. A. Estroff, J. K. Kriebel, R. G. Nuzzo, G. M. Whitesides, *Chem. Rev.* **2005**, *105* 1103.

[38] Suk-Wah Tam-Chang, Hans A. Biebuyck, George M. Whitesides, Nooh Jeon, R. G. Nuzzo, *Langmuir* **1995**, *11*, 4371.

[39] S. Slavomir, A. Misicka, R. Bilewicz, *J. Phys. Chem. B* **2000**, *104*, 5399.

[40] R. S. Clegg, S. M. Reed, R. K. Smith, B. L. Barron, J. A. Rear, J. E. Hutchison, *Langmuir* **1999**, *15*, 8876.

[41] A. Salomon, T. Boecking, O. Seitz, T. Markus, F. Amy, C. Chan, W. Zhao, D. Cahen, A. Kahn, *Advanced Materials* **2007**, *19*, 445.

[42] M. Davies, H. A. Jones, *Transaction Faraday Society* **1959**, 1329.

[43] C. A. Hunther, J. K. M. Sanders, *J. Am. Chem. Soc.* **1990**, *112*, 5525.

[44] C. B. Gorman, Y. F. He, R. L. Carroll, *Langmuir* **2001**, *17*, 5324.

[45] O. Azzaroni, M. E. Vela, H. Martin, A. H. Creus, G. Andreasen, R. C. Salvarezza, *Langmuir* **2001**, *17*, 6647.

[46] M. L. Carot, V. A. Macagno, P. Paredes-Olivera, E. M. Patrito, *J. Phys. Chem. C* **2007**, *111*, 4294.

[47] M. J. Giz, B. Duong, N. J. Tao, *J. Electroanal. Chem.* **1999**, *465*, 72.

[48] C. K. Rhee, Y. N. Kim, *Appl. Surf. Sci.* **2004**, *228*, 313.

[49] P. A. Lewis, R. K. Smith, K. F. Kelly, L. A. Bumm, S. M. Reed, R. S. Clegg, J. D. Gunderson, J. E. Hutchison, P. S. Weiss, *J. Phys. Chem. B* **2001**, *105*, 10630.

[50] G. E. Poirier, M. J. Tarlov, *Langmuir* **1994**, *10*, 2853.

[51] A. Riposan, G. Y. Liu, *J. Phys. Chem. B* **2006**, *110*, 23926.

[52] E. Delamarche, B. Michel, Ch. Gerber, D. Anselmetti, H.-J. Guentherodt, H. R. H. Wolf, *Langmuir* **1994**, *10*, 2869.

[53] L. Muller-Meskamp, B. Lussem, S. Karthauser, R. Waser, *J. Phys. Chem. B* **2005**, *109*, 11424.

[54] Y. Cho, A. Ivanisevic, *Journal of Physical Chemistry B* **2005**, *109*, 6225.

[55] R. G. Nuzzo, L. H. Dubois, D. L. Allara, *J. Am. Chem. Soc.* **1990**, *112*, 558.

[56] X. Z. Du, W. Miao, Y. Q. Liang, *Journal of Physical Chemistry B* **2005**, *109*, 7428.

[57] I. Wenzl, C. M. Yam, D. Barriet, T. R. Lee, *Langmuir* **2003**, *19*, 10217.

[58] R. S. Clegg, J. E. Hutchison, *J. Am. Chem. Soc.* **1999**, *121*, 5319.

[59] M. Bieri, T. Burgi, *Journal of Physical Chemistry B* **2005**, *109*, 22476.

[60] Y. S. Chi, I. S. Choi, *Langmuir* **2005**, *21*, 11765.

[61] R. S. H. Clegg, J. E., *Langmuir* **1996**, *12*.

[62] W. Azzam, A. Bashir, A. Terfort, T. Strunskus, C. Woll, *Langmuir* **2006**, *22*, 3647.

[63] R. C. Sabapathy, S. Bhattacharyya, M. C. Leavy, W. E. Cleland, C. L. Hussey, *Langmuir* **1998**, *14*, 124.

[64] R. C. Sabapathy, R. M. Crooks, *Langmuir* **2000**, *16*, 7783.

CHAPTER 6

ADSORPTION OF MOLECULAR GRIDS ON HOPG SUBSTRATE

In this chapter the self-assembly properties at surfaces of different molecular ligands and their metal ion complexes, which exist as [2x2] grids, is presented. All the molecules described in this chapter were synthesized by Artur Stefankiewicz, PhD student in the laboratory of Professor Jean-Marie Lehn, in ISIS (Strasbourg).

6.1 STM at the solid liquid interface

STM performed at the solid-liquid interface technique may be used to investigate the molecular self-assembly properties on ultra-flat surfaces, primarily on HOPG substrates.[1-3] In this technique, a drop of a solution containing the target molecules is placed on the flat substrate (drop-casting adsorption method). Then the STM probe is slowly brought towards the substrate until it is immersed in the drop solution. The advantage of this technique is its versatility compared to studies performed in ultra high vacuum (UHV). In these, molecules are typically processed on surfaces by means of the organic molecular beam epitaxy (OMBE) technique, thus only molecules that can be sublimed without thermal decomposition can be studied. Furthermore, the UHV conditions are far from the ambient conditions where a device is supposed to operate.

6.2 Grid-type metal ion Architectures

Supramolecular complexes are ideal candidate building-blocks for the fabrication of molecule-based integrated circuit chips. In fact, supramolecular chemistry enables the self-

assembly of molecular bricks at the nanometer scale matching the requirements for the development of molecular electronics. Furthermore supramolecular complexes are extremely versatile, as they can be tailored to give intrinsic physico-chemical properties, such as switching properties ideal for the integration in an ON/OFF circuit.

In the last few years, new developments in supramolecular coordination chemistry have enabled the synthesis of a variety of transition-metal complexes of grid-type architecture.
Grid-like metal ion arrays are formed by a set of metal ions held in a regular network of organic ligands. The grid's design principles are based on the supramolecular assembly concept and the rules of coordination chemistry. A rich library of metal-supramolecular complexes has been synthesized: metal helicates, rotaxanes, catenanes and cages (see chapter 1).
Grid like coordination complexes containing *n*x*n* and *n*x*m* metal ion centers, with $n,m \leq 4$, have been already synthesized by using tetrahedral as well as octahedral coordinating metal ions (Fig. 6.1). For strong binding of the metal ion, the ligand has to contain the right number of coordination sites in order to complete the coordination sphere of the metal ion. The most common binding units are based on bipyridine or terpyridine chelating ligands.[4, 5]

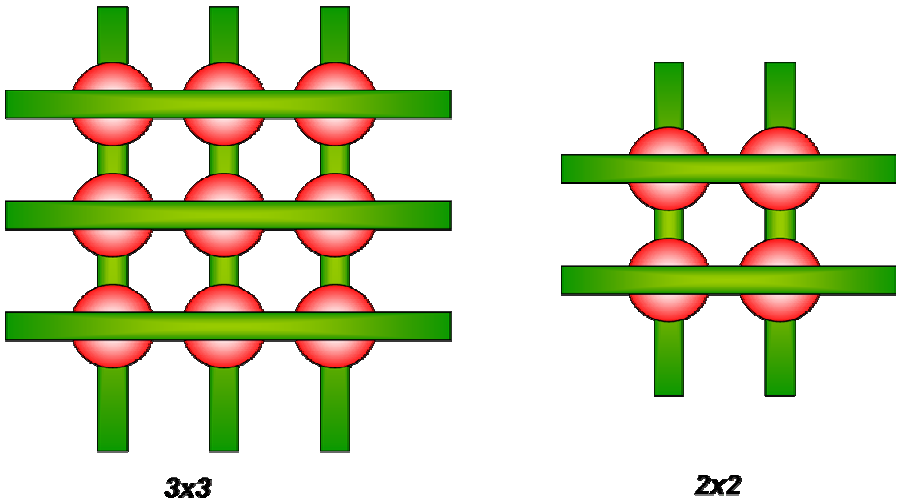

Figure 6.1: Schematic drawing illustrating a *3*x*3* and a *2*x*2* the crossed wire-like grid formed by molecular components. In green are represented the ligands and in red the metal ions.

The molecular grid structures resemble a multiple wiring network where the information can be stored at each ligand crossing point where a metal ion is located. The combination of the metal and ligand properties confers unique optical, magnetic and electrochemical properties to the final molecular grid.[6-10] These feature render the grid-

molecule a future candidate to be implemented in information data storage and processing devices.[11, 12]

To this end, it is also fundamental to gain as much insight as possible on the assembly properties of these molecules at solid substrates. In fact together with the molecular design required to achieve the switching functionality, a further careful design has to be performed in order to make those molecules addressable once they are on solid substrate. In particular functional, groups have to be added to the grid-type molecule to favour the assembly on the solid substrate. In fact, it has been observed that the physisorption of molecular grids is not thermodynamically favoured, as the high charge on the grid decreases its the for the apolar HOPG substrate.[13] STM studies of densely packed monolayers formed on HOPG substrate by a [2x2] Co_4^{II} grid based on a poly-pyridine ligand (4,6-bis(2",2'-bipyrid-6'-yl)-2-phenylpyrimidine)[14] have been already reported.[15]

In their work, Schubert and co-authors described a highly stable monolayer formed by a cobalt(II) [*2*x*2*] complex on HOPG. The deposition method employed in the work was drop casting from dilute acetone solutions. The assembly process of molecules on HOPG substrate can be viewed as a two-dimensional crystallization where the substrate has the role of a template for the crystalline domain growth. Interestingly, the authors found that the orientation of the grids relative to the surface plane can be controlled by varying particular functional groups of the ligand. In particular substituting the ligand with R_1, R_2= H and R_3= CH_3 favoured an edge-on orientation of the grids with respect to the substrate, whereas choosing the following unit R_2, R_3= H and R_1= CH_3 resulted in flat lying grid.[15, 16]

Several supramolecular ion assemblies of different structural complexity and incorporating different transition metal ions were deposited on HOPG and investigated by STM and current imaging tunneling spectroscopy (CITS). This last technique allowed the spatial localization of the metal ions in the adsorbed molecular complex, and such work opened perspective toward the bottom up growth of "ion dots" on solid substrate.[17]

Similarly, [*2*x*2*] Co^{II} complexes formed by bis(terpyridine)-derived ligands and substituted with an additional para-pyridyl or n-propyl-thia unit reduce the 2D assembly favouring a weak adsorption and therefore a high mobility of the molecules on the substrate. Recently a Mn^{II} grid was investigated on Au(111) substrate.[18]

Monolayers of hydroxyl-terminated grids have been organized at the air water interface using the Langmuir Blodget (LB) technique.[19, 20] Multilayers of the metal grid-like complex have been prepared through the layer-by-layer technique.

In this chapter, a new ligand containing pyridylhydrazones units forming [2x2] grid-like complexes has been synthesized and characterized at the solid-liquid interface by Scanning Tunnelling Microscopy.

6.3 Results and discussion

The grid-complexes formed by the bis-hydrazone lidand (L) have been thoroughly characterized in the past.[8, 21-25] This ligand forms tetranuclear [2x2] grid-type transition metal complexes with Co^{II}, Fe^{II}, Zn^{II}, Mn^{II} metal ion (Fig. 6.1). Per each bis-hydrazone ligand two tridentate coordination sites are present allowing the octahedral coordination of the metal ions in the grid.

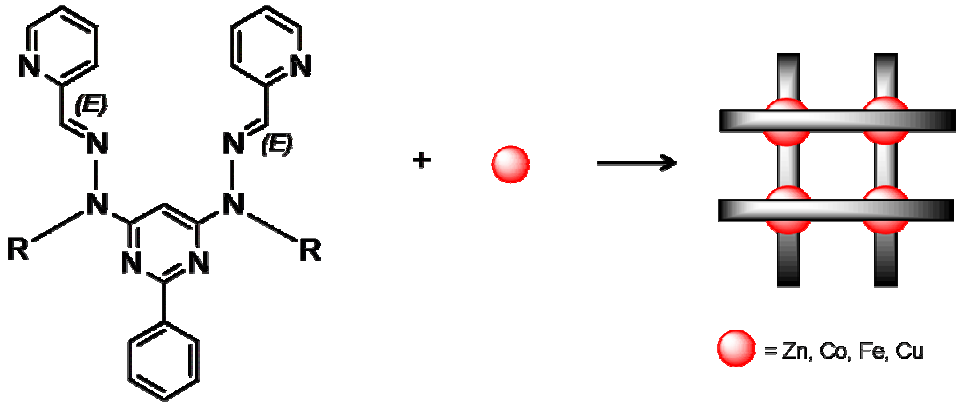

Figure 6.1: Molecular structure of the pyridylhydrazone unit used to synthesize the ligands studied in this work.

Interestingly, for R=H the $[Co_4^{II}L_4]^{8+}$ complex showed reversible optical properties that can be triggered by pH variation in solution. By modulating the multiple reversible protonation/deprotonation of the complex remarkably changes the UV-vis spectrum can be observed. An intense color variation, from yellow at low pH to violet above neutral pH, accompanies the optical switching process. Furthermore, for R=H, the protonation/deprotonation process of the $[Co_4^{II}L_4]^{8+}$ complex determine a variation of the oxidation state of the Co metal ion. The complete deprotonation of the NH groups in the grid

leads to for the atmospheric oxidation of the Co^{II} to Co^{III}, resulting in a variation of the magnetic properties of the grid from paramagnetic (Co^{II}) to diamagnetic (Co^{III}).

X-ray analysis of the crystal formed by the grid complex of L showed that the distance between the pyridine rings of two parallel ligands is ~7Å. An important role in the stabilization of the grid complexes is played by the phenyl substituents that are ortogonally twisted with respect to the pyrimidine rings and are sandwiched between the two ligands at a distance of 3.5Å. This configuration of the phenyl group in the grid complex introduces favorable π-π interactions.

It is well known that alkanes form densely packed 2D-assemblies on HOPG, thanks to their high affinity for this substrate. Furthermore, alkyl chains tend to assemble commensurately with the HOPG surface. Such a template effect, due to the epitaxial growth of the alkane domains on HOPG, might induce the ordered assembly also of molecules poorly interacting with the HOPG substrate.[26] This can be done by functionalizing the molecule with long alkyl chains. This strategy has been followed in the work presented in this chapter. Thus, in order to improve the affinity for the HOPG substrate, we added long alkyl chain to the end sites of the ligand (***L1*** and ***L2*** in Fig. 6.2). Furthermore, to characterize possible effects on the molecular packing on HOPG, due to a different functionalization added on the hydrazone unit, we also studied a methyl-hydrazone derivative (***L2***).[27]

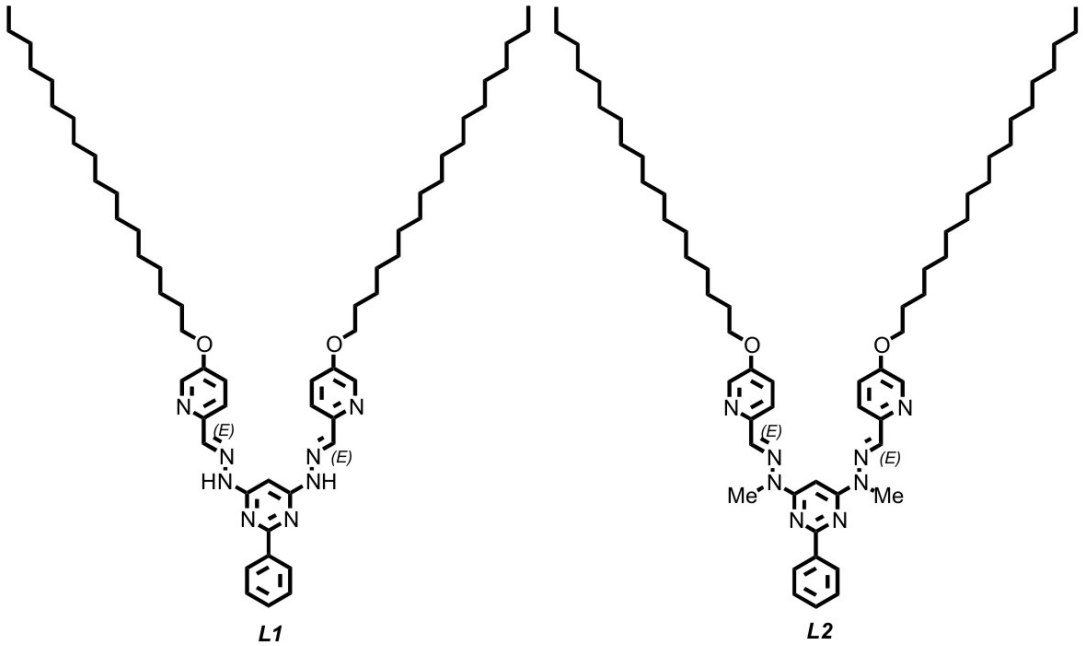

Figure 6.2: Molecular structures of the free ligands used to build the molecular grid.

6.3.1 Self-Assembly of the free ligand on HOPG

Fig. 6.3 shows the STM image of a L1 monolayer at the solution-graphite interface. It displays the typical lamellar packing found for alkanes adsorbed on HOPG. The good interactions between the alkyl chains and the HOPG as well as the interdigitation between the chains which optimizes van der Waals interactions, are responsible for the molecular packing observed. Grain boundaries are not sharp but rather curved domain boundaries are observed; i.e. in passing from a growth orientation to another the lamella smoothly rearrange along the domain borders with a very low curvature radius. This phenomenon has been attributed to the high mobility of the ligand ***L1***, particularly observed in the first steps of the domains growth where the system behave has 2D liquid phase (Fig. 6.3-A). In view of the high mobility spatially extended and stable domains are usually obtained after 12h from the drop deposition (Fig. 6.3-B).

The high resolution STM images clearly show that the alkyl chains orient perpendicularly to the lamella main axis. The brightest lamella feature is represented by the aromatic core of the ligand which contributes more to the surface density of states than the alkyl chains (appearing darker in the STM images).

Two structures have been proposed to describe the observed molecular patterning as illustrated in Fig. 6.3-C and Fig. 6.3-D. The first packing consists of interdigitated alkyl chains and the conjugated group is placed edge-on on the HOPG (Fig. 6.3-C).[28-30] In the second model the chain are still interdigitated but the aromatic moiety is now flat lying on the substrate (Fig. 6.3-D). Even if both models fit with the measured lattice parameters (Fig. 6.4-E) the molecular packing shown in Fig. 6.3-D is more likely to occur. In fact, such molecular packing may be further stabilized by intermolecular hydrogen bonding as illustrated in Fig. 6.4-C.[31] Furthermore, the face-on arrangement is stabilized by the π-π interactions between the aromatic rings of the adsorbate and the graphite surface.

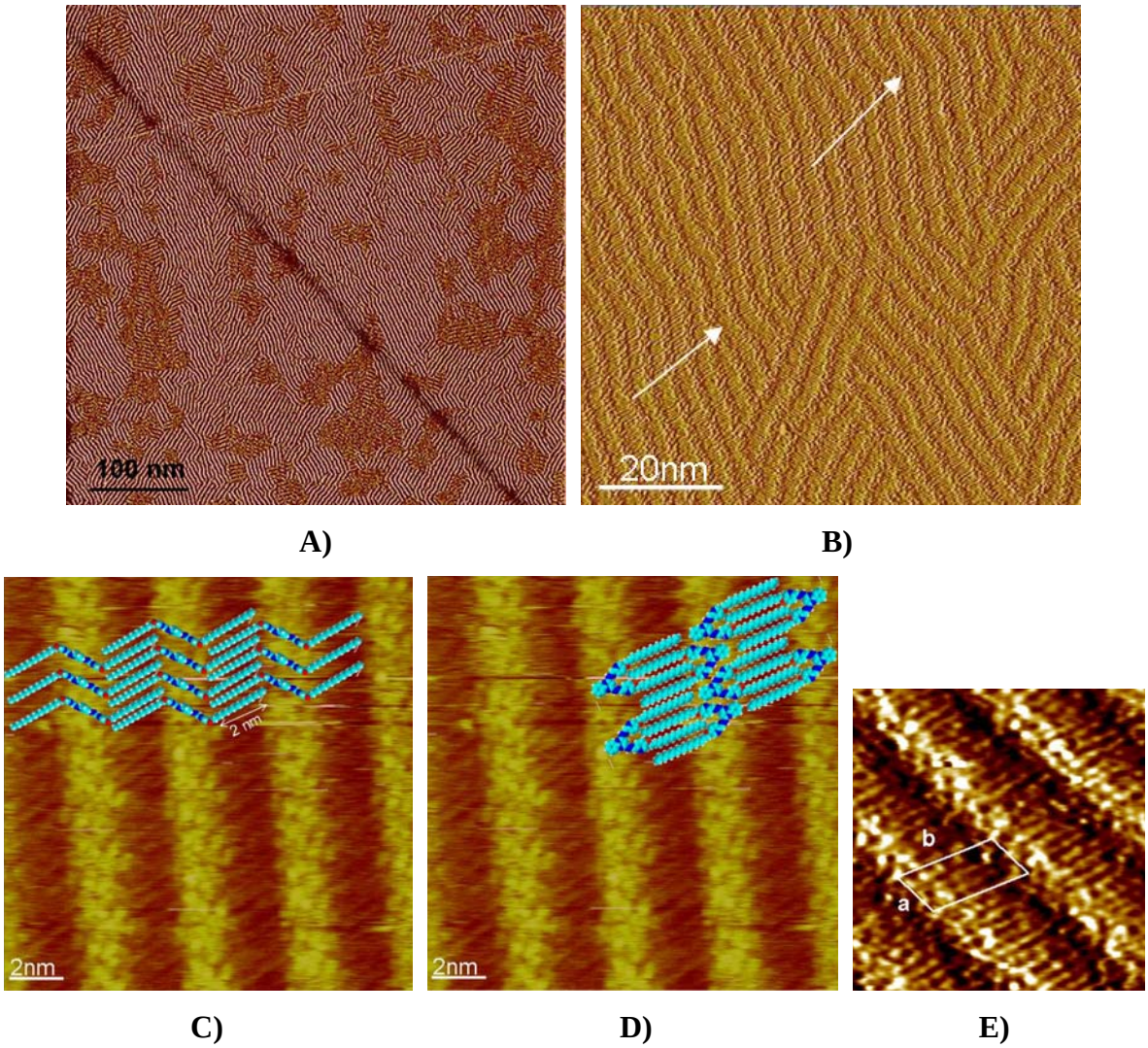

Figure 6.3: A)-D) STM images (constant current mode) [22]of the 2D assembly formed by the ligand ***L1*** on HOPG. **A)** the picture has been registered at the initial adsorption steps; the absence of narrow domain boundaries indicates the high mobility of the molecules at this stage of the assembly. **B)** White arrows indicate the smooth domain boundaries described in the chapter. Average Tunneling, Current: I_t=65pA, Bias Voltage V_t=850mV. **C)** and **D)** STM height contrast images: the two possible molecular packings of ***L1*** on HOPG are schematized. **E)** Unit cell parameters: a= (2.08±0.05) nm; b= (4.24±0.05) nm; α=66°±10°; Area= (8.1±0.1) nm^2

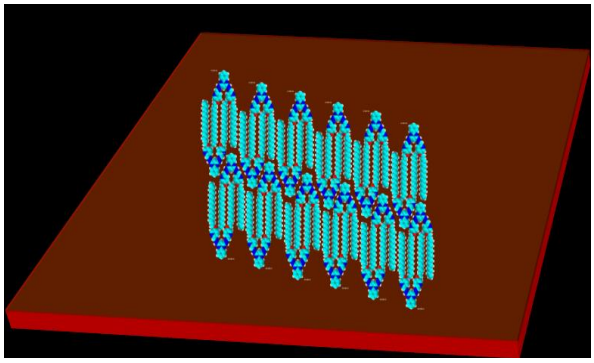

(A)

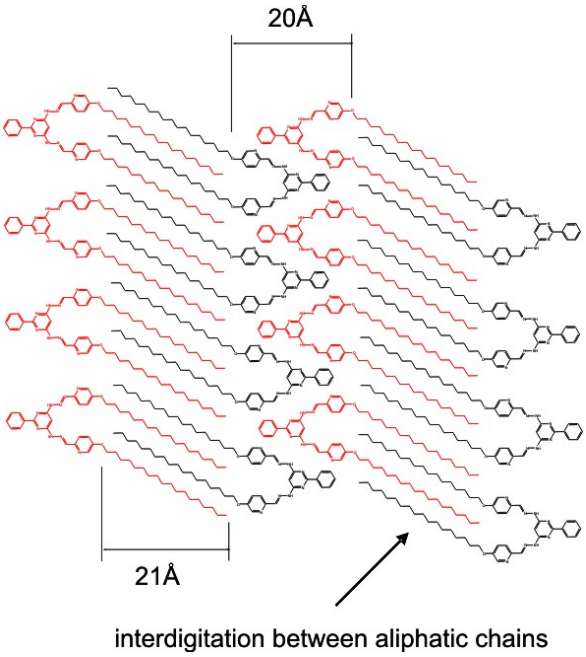

(B)

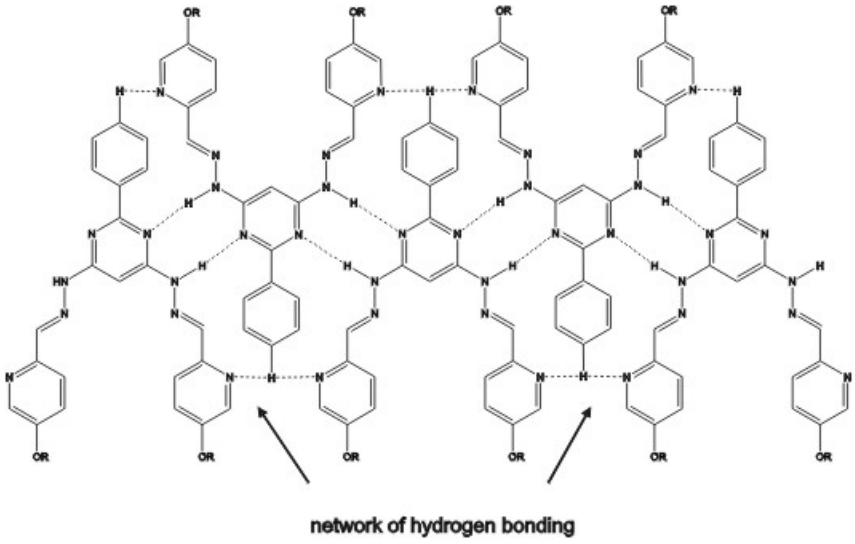

(C)

Figure 6.4: A) and **B)** Molecular sketch depicting the face-on packing of ligand ***L1***on HOPG. **C)** scheme of the H-bond networks formed between the hydrazone and the pyridine units of ligand ***L1***.

Ligand ***L2*** has a peculiar behaviour with respect to the one observed for ***L1*** assembled on HOPG. Domain boundaries are sharper and the molecular diffusion is less important than observed for the ligand ***L1***. The major difference is the presence of the methyl groups as substituents on the hydrazone function, which makes it more difficult for ***L2*** to form as many

intermolecular hydrogen bonds as in the case of ***L1***. In fact, it cannot form NH···N bonds, but only CH···N, which are presumably weaker. The lack of the H-bonds which strongly stabilize the lamella structure of ***L1***, promotes the formation of on other stable molecular packing. This is the reason why polymorphism is observed for the ligand ***L2***. Two polymorph 2D crystals have been observed for ***L2*** (Fig. 6.5): a honeycomb-like structure and a lamellar-like structure (Fig. 6.6 and Fig. 6.7 respectively). The two polymorph structures can be described as formed by the ***L2*** ligand displaced with the aromatic unit oriented face-on the HOPG substrate while the alkyl chains are interdigitated.

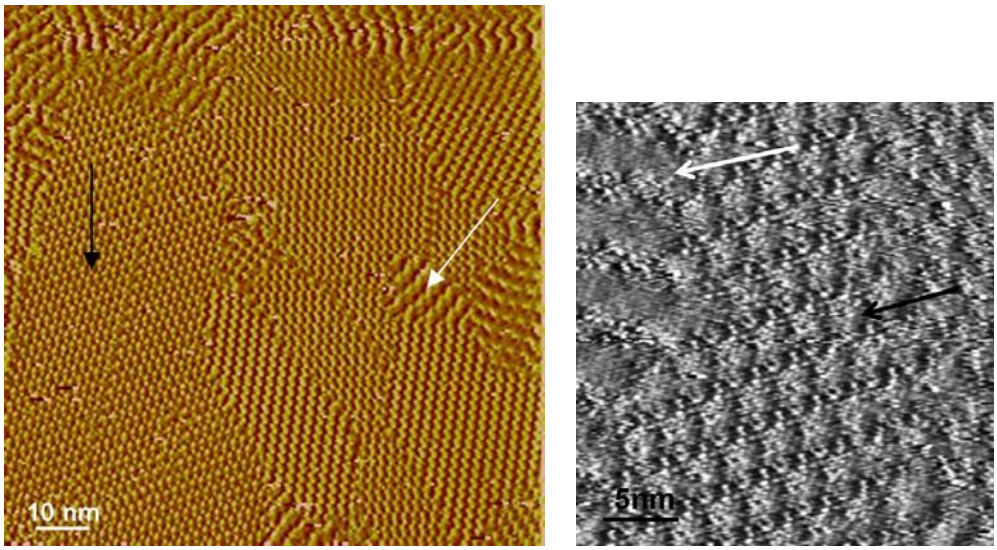

A) **B)**

Figure 6.5: STM current image of the ligand ***L2*** adsorbed on HOPG substrate. **A)** The black arrow indicates the honeycomb assembly; the white arrow indicates the lamellar structure. Average Tunneling Current: I_t=25pA, Bias Voltage V_t=400mV; **B)** Average Tunneling Current: I_t=45pA, Bias Voltage V_t=620mV.

The lamellar phase found for ***L2*** has a wave feature that is not present in the lamellar domains of ***L1*** (Fig. 6.6). The presence of the methyl group as functional substituent on the hydrazone unit introduces a steric hindrance between the adjacent aromatic units in the lamella. To reduce this sterical hindrance two adjacent ligands slide in opposite directions perpendicularly to the lamellar main axes, giving rise to the second polymorph structure, the honeycomb, (Fig. 6.7) and conferring to the lamella this wave-like feature.

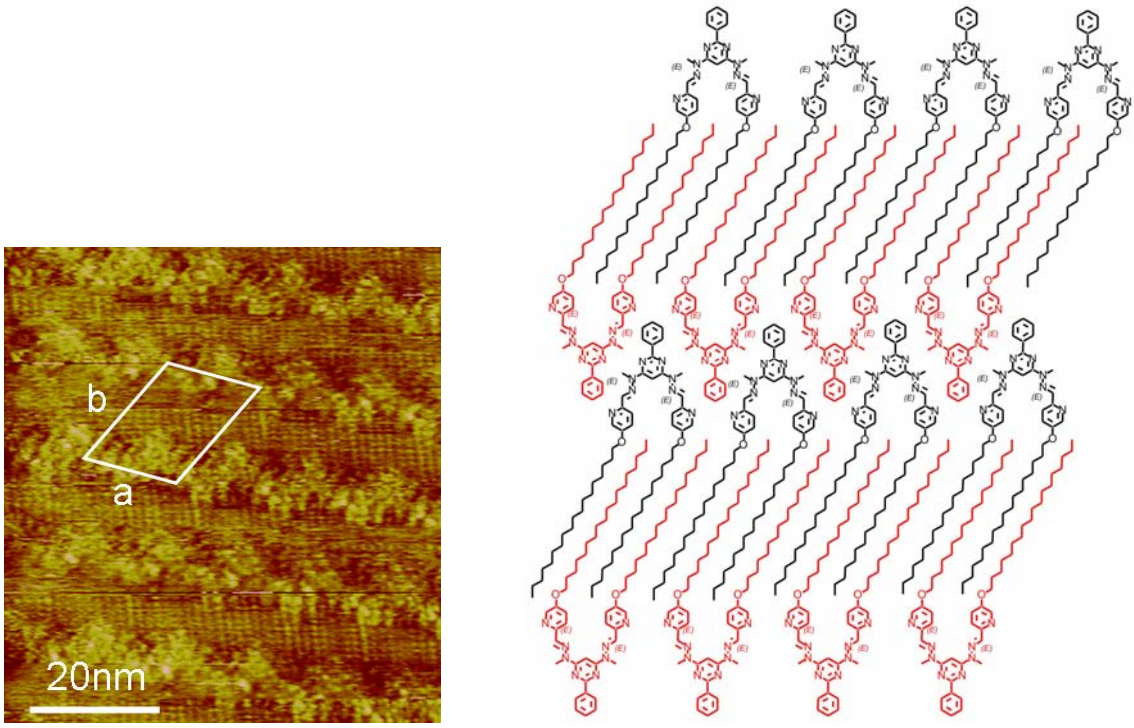

Figure 6.6: A) STM height contrast image of the lamella-like domain formed by ligand ***L2***. Unit Cell parameters: a= (4.99±0.05) nm; b= (3.63±0.05) nm; α= 70°±10°; Area= (16.2±0.1) nm^2. **B)** Proposed molecular packing of ***L2*** in the lamellar-like structure.

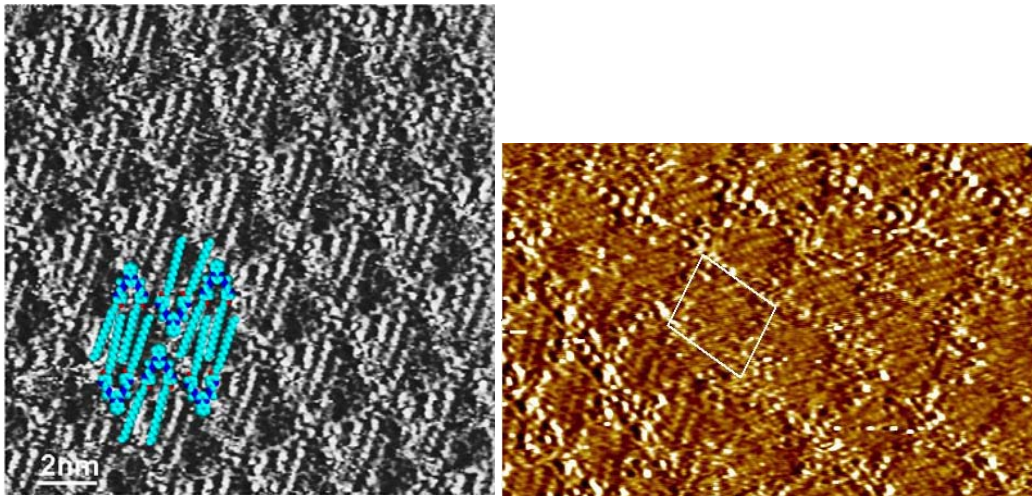

A) **B)**

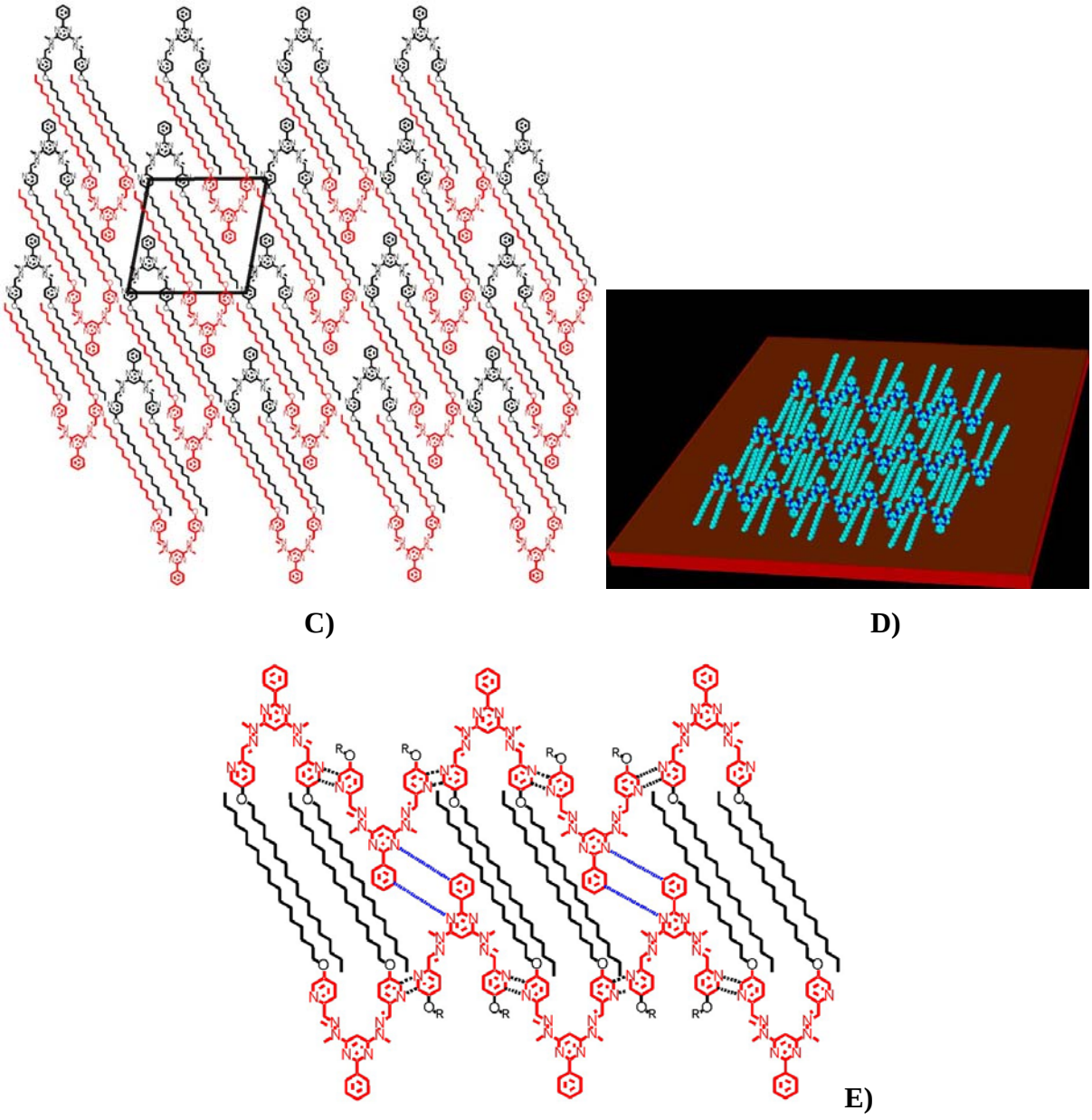

Figure 6.7: A) and **B)** STM current contrast image of the honeycomb-like domain formed by ligand ***L2***. Unit Cell parameters: a= (2.85±0.05) nm; b= (3.23±0.05) nm; α=80°±10°; Area= (9.1±0.1) nm^2. **C)** and **D)** proposed molecular packing of ***L2*** in the honeycomb structure. **E)** H-bonding network existing in the honeycomb-like packing of ***L2***.

Figure 6.7-E show that also the honeycomb-like patterning can be stabilized by intramolecular H-bonding. Blue lines in Fig. 6.7-E, indicate additional H-bonds which might be formed for an even more dense honeycomb-like structure of ***L2***; however a more dense packing that would also imply a loss in the optimal interdigitation of the alkyl chains. Furthermore, it is worthy at notice that the degree of extension of those H-bonds over the

structure is less important with respect to the H-bond network presents in the lamellar-like patterning. The reduced H-bond stabilization found for the honeycomb structure is the reason why the density of this phase decreases over long equilibration time, with respect to the lamellar phase.

6.3.2 Self-assembly of molecular Co-grid of *L1* on HOPG

Different grid metal ion complexes of the two ligands have been tested for the adsorption on the HOPG substrate. Coordination complexes formed by ***L1*** and ***L2*** with Fe, Zn and Co have been tested. Unfortunately, the adsorption of those complexes on HOPG is still unfavoured and the alkyl chains seem to not play a key role in helping the grid to adsorb on the surface. However, the adsorption of the Co-grid complex of the ligand ***L1*** (Fig. 6.8) was occasionally observed.

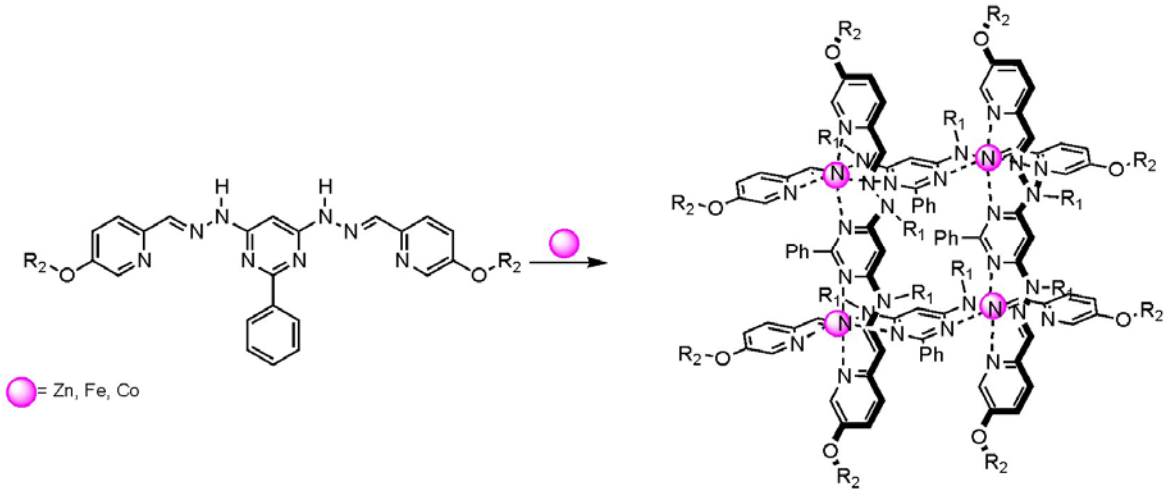

Figure 6.8: Molecular structure of the Co-grid complex formed by the pyridylhydrazone ligand ***L1*** (R_1=H***;*** R_2=$C_{18}H_{35}$).

Substantial differences could be observed between the bi-dimensional molecular packing obtained with the pure ligand ***L1*** and the complex respectively. The molecular packing observed in Fig. 6.10 is not comparable with the 2D-assembly formed by the free ligand ***L1*** on HOPG, and this structure has been therefore attributed to a bi-dimensional assembly of the relative Co-grid complex. We found the following unit cell parameters: a=1.27 nm; b= 5.11 nm; α=70°.This parameters nicely fit with the grid dimensions calculated in the model (Fig. 6.9).

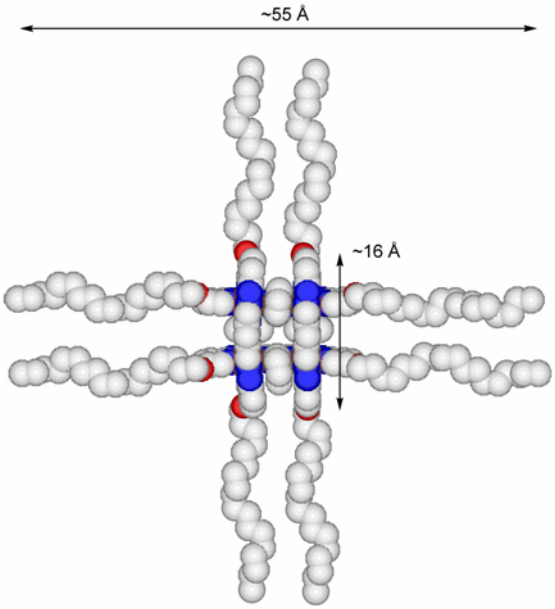

Figure 6.9: Model of structure of the molecular Co-grid formed by the ligand ***L1***.

However, we could not exactly define the molecular arrangement in the 2D-crystal. According to the observed image contrast, we would exclude a face-on packing where the grid is positioned flat lying on the HOPG substrate. In fact, with this configuration we would expect to see four bright spots placed at a distance of ~12Å per each molecule adsorbed on the substrate, each spot relating to the high electronic density located near the metal ion center. In the case of the pure ligand interdigitation between alkyl chains, flat lying on the HOPG substrate, could be clearly observed, whereas the orthogonal coordination of the metal ion in the complex does not allow the face-on π bonding of the aromatic rings on the graphite surface.

Probably the grid is displaced almost edge-on on the HOPG, although it is not easy to determine the tilt angle of the molecular plane with respect to the surface plane. As well, it is worth saying that in this configuration it is quite likely that some of the alkyl chains are pointing out from the surface, which makes the interpretation more difficult. Fluctuating alkyl chains have been observed to appear in STM images as bright spots, and this might explain the many spots appearing in the STM of the Co-grid of ***L1***. Additionally, the grid exists with its eight tetrafluoroborate counteranios which should reside on the surface in between adjacent grids. Finally, it is difficult to give a correct interpretation of the molecular packing of the Co-grid of ***L1***. However, a similar 2D grid assembly on HOPG was observed

in the work of M. Möller and co-authors and they also conclude that the molecular grid plane lies perpendicular to the surface rather than assuming a face-on configuration.[15, 32]

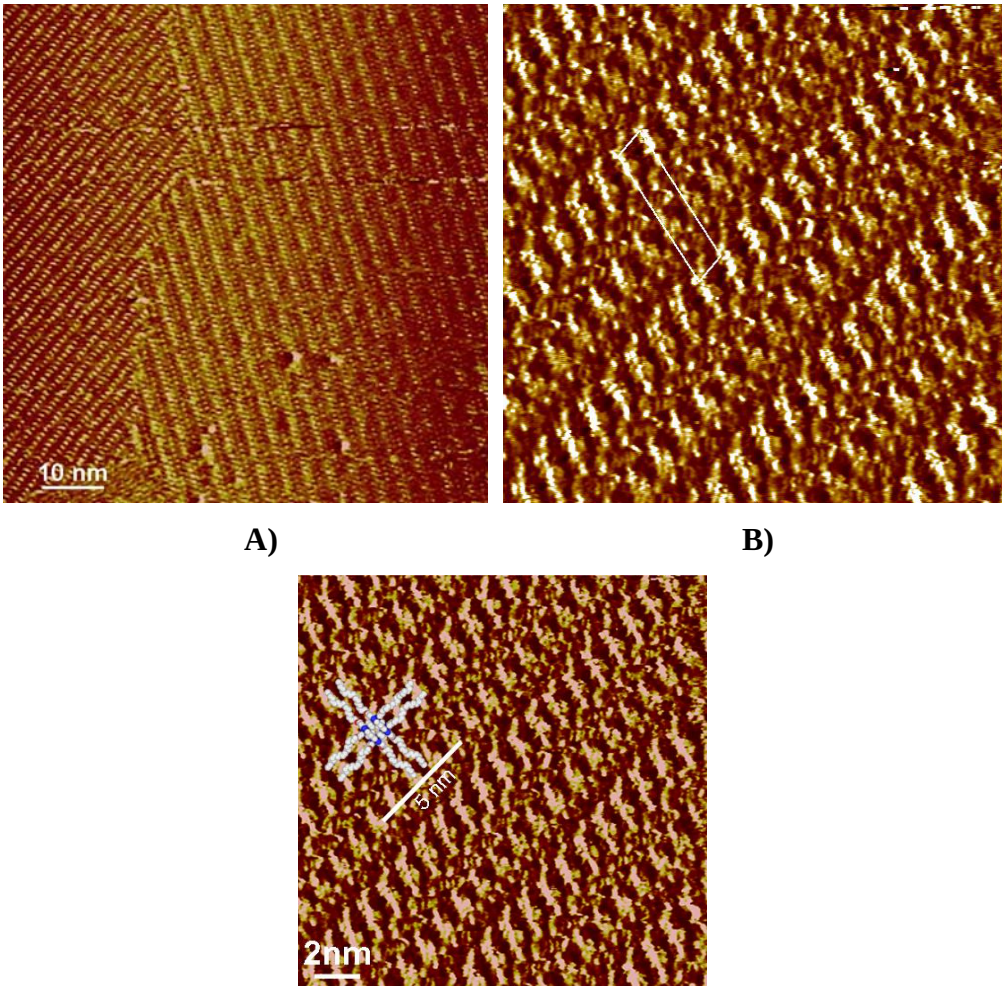

Figure 6.10: A)-C) STM current images of the molecular Co-grid formed by the ligand ***L1*** adsorbed on HOPG substrate: Average Tunneling Current, I_t=35pA, Bias Voltage, V_t=583.3mV. **B)** Unit cell parameters: a=1.27 nm; b= 5.11 nm; α=70°. The unit cell has been corrected for the thermal drift through SPIP software. **C)** The picture illustrates the scaled dimension of the Co-grid molecular structure with respect to the lattice dimension of the grid crystalline domain. The molecular lattice clearly does not fit with a face-on arrangement of the grid on the HOPG surface.

The poor reproducibility of the assembly did not help in gaining deeper insight. In fact, due to the poor affinity of the grid for the HOPG substrate, the assembly process at surface

requires peculiar solute-solute interactions to favour molecular physisorption. This means that the solution should be prepared at quasi-crystallization concentrations. In particular, one should make sure that the first crystal nucleation would happen on the HOPG substrate rather than at the bottom of the flask. Furthermore, this first nucleus should grow in two dimensions exploiting the template action of the HOPG, rather than expanding in a tri-dimensional crystal. The importance of this point was already stressed in the work of S. Schubert and co-authors. They observed that the use of a solution free of grid aggregates promoted the 2D assembly of the Co-grid formed by the 4,6-bis(2',2"-bipyridyl-6-yl)pyrimidine ligands. All these observations can be understood if we take into consideration the different interactions leading to the formation of a 2D molecular assembly on solid substrate: i) the molecule-substrate; ii) molecule-molecule; iii) molecule-solvent; iv) solvent-substrate. This last contribution can be neglected as the solvent employed, phenyloctane, is well known to not form a stable assembly on HOPG. The first contribution, the grid-HOPG interaction, seems to be not favoured. A reasonable explanation arises from the polar character of the grid which prevents the "spontaneous physisorption" on HOPG[i]. Since we are working under supersaturated conditions (often in presence of precipitates) the solvation should not strongly interfere with the self-association between molecules and with the molecule-substrate interactions. As the point iv) and iii) are not important under by the experimental conditions employed and, as it is clear that there is not a good affinity between the HOPG and the grid, then the fundamental factor that will lead the process toward a bi-dimensional assembly must be molecule-molecule interactions. In view of the above, strong lateral interactions are needed to favour the 2D assembly. Possibly the 2D interactions should be stronger that the molecule-molecule interactions holding the third dimension in a 3D crystal. Of course, if the repulsion between the grid assembly and the HOPG is too strong, then it will not be possible to observe any ordered molecular packing on the substrate anyway. However, since we could observe the grid packing (Fig. 6.10) we do not comply with this last condition but rather we are playing with the delicate equilibrium involved in the crystallization processes from solution. This involves to a narrow regime of the solution parameters (concentration, high solubility solvent concentration, high boiling solvent concentration and temperature) that can promote the grid assembly, and therefore it makes difficult to reproduce the experiment.

[i] It is worth saying that also strong molecule-substrate interactions might hinder the formation of a crystalline assembly. In fact the assembly is a dynamic process that requires diffusion of molecules in solution and on the substrate. Strong interactions molecular limit the molecular diffusion on the surface. However, this is not a case seen in this work.

The 2D assembly of the Co-grid formed by ***L1*** was obtained by drop-casting of a solution prepared as follows. We attempted to start from a supersaturated solution of the Co-grid of ***L1*** in phenyloctane containing the Co-grid precipitate at the bottom of the flask. The mixture was heated at 70° for 15 minutes, but we could not achieve precipitate dissolution. A few drops of acetonitrile were slowly added to the solution, while heating at 70°, until the complete dissolution of the precipitate was reached. This step is quite important, as in fact the amount of acetonitrile to be added should not exceed too much the quantity needed to dissolve the grid at 70°. The ideal conditions for the crystallization are described by a system that is soluble at high temperature but that starts to crystallize at room temperature. To remove the excess of acetonitrile it is possible to leave the sample at 70° above the heating plate to evaporate the excess acetonitrile. Then, the solution was removed from the heating plate and quickly a drop of it was placed on the HOPG in the STM apparatus. As can be seen, this procedure it is difficult to reproduce as the crystallization conditions exist in a narrow regime of the overall parameters: concentration of the grid, volume of the high solubility solvent, volume of the high boiling solvent and finally the temperature.

Thus alteration of various conditions may enable a better design of the grid for its assembly on HOPG. In particular, the system can be improved by designing molecular grids that either have greater affinity for the HOPG and/or that favour the bi-dimensional interactions. In the last case it is important to add specific interactions that would encourage the lateral assembly in a 2D molecular crystal.[33]

This last concept is not new. In many previous reports it has been observed that good assemblies on HOPG are obtained by using molecules which can pack on the substrate through the formation of 2D intermolecular interactions, e.g. 2D hydrogen bonding.[31]

The arrangement of special functional units with nanometer dimensions into defined molecular architectures like grid complexes on surfaces is one of the major goals in supramolecular chemistry and material science. The ability to control and manipulate such arrangements could provide approaches to locally addressable, inorganic storage devices for molecular electronics.

References

[1] S. De Feyter, F. C. De Schryver, *J. Phys. Chem. B* **2005**, *109*, 4290.

[2] A. C. Grimsdale, K. Mullen, *Angewandte Chemie-International Edition* **2005**, *44*, 5592.

[3] D. M. Cyr, B. Venkataraman, G. W. Flynn, *Chem. Mater.* **1996**, *8*, 1600.

[4] J. McMurtrie, I. Dance, *Crystengcomm* **2005**, *7*, 216.

[5] J. McMurtrie, I. Dance, *Crystengcomm* **2005**, *7*, 230.

[6] M. Ruben, E. Breuning, M. Barboiu, J. P. Gisselbrecht, J. M. Lehn, *Chemistry-a European Journal* **2003**, *9*, 291.

[7] M. Ruben, E. Breuning, J. M. Lehn, V. Ksenofontov, F. Renz, P. Gutlich, G. B. M. Vaughan, *Chemistry-a European Journal* **2003**, *9*, 4422.

[8] L. H. Uppadine, J. P. Gisselbrecht, J. M. Lehn, *Chemical Communications* **2004**, 718.

[9] L. H. Uppadine, J. P. Gisselbrecht, N. Kyritsakas, K. Nattinen, K. Rissanen, J. M. Lehn, *Chemistry-a European Journal* **2005**, *11*, 2549.

[10] M. Ruben, U. Ziener, J. M. Lehn, V. Ksenofontov, P. Gutlich, G. B. M. Vaughan, *Chemistry-a European Journal* **2004**, *11*, 94.

[11] N. Lin, S. Stepanow, F. Vidal, K. Kern, M. S. Alam, S. Stromsdorfer, V. Dremov, P. Muller, A. Landa, M. Ruben, *Dalton Transactions* **2006**, 2794.

[12] M. S. Alam, S. Stromsdorfer, V. Dremov, P. Muller, J. Kortus, M. Ruben, J. M. Lehn, *Angewandte Chemie-International Edition* **2005**, *44*, 7896.

[13] M. Ruben, J. Rojo, F. J. Romero-Salguero, L. H. Uppadine, J. M. Lehn, *Angewandte Chemie-International Edition* **2004**, *43*, 3644.

[14] M. L. Scudder, H. A. Goodwin, I. G. Dance, *New Journal of Chemistry* **1999**, *23*, 695.

[15] A. Semenov, J. P. Spatz, J. M. Lehn, C. H. Weidl, U. S. Schubert, M. Moller, *Applied Surface Science* **1999**, *145*, 456.

[16] A. Semenov, J. P. Spatz, M. Moller, J. M. Lehn, B. Sell, D. Schubert, C. H. Weidl, U. S. Schubert, *Angewandte Chemie-International Edition* **1999**, *38*, 2547.

[17] M. Ruben, J. M. Lehn, P. Muller, *Chemical Society Reviews* **2006**, *35*, 1056.

[18] L. Weeks, L. K. Thompson, J. G. Shapter, K. J. Pope, Z. Xu, *Journal of Microscopy-Oxford* **2003**, *212*, 102.

[19] I. Weissbuch, P. N. W. Baxter, I. Kuzmenko, H. Cohen, S. Cohen, K. Kjaer, P. B. Howes, J. Als-Nielsen, J. M. Lehn, L. Leiserowitz, M. Lahav, *Chemistry-a European Journal* **2000**, *6*, 725.

[20] T. Salditt, Q. An, A. Plench, C. Eschbaumer, U. S. Schubert, *Chem. Commun.* **1998**, *24*, 2731.

[21] L. H. Uppadine, J. M. Lehn, *Angewandte Chemie-International Edition* **2004**, *43*, 240.

[22] M. Ruben, J. M. Lehn, G. Vaughanc, *Chemical Communications* **2003**, 1338.

[23] M. Barboiu, M. Ruben, G. Blasen, N. Kyritsakas, E. Chacko, M. Dutta, O. Radekovich, K. Lenton, D. J. R. Brook, J. M. Lehn, *European Journal of Inorganic Chemistry* **2006**, 784.

[24] X. Y. Cao, J. Harrowfield, J. Nitschke, J. Ramirez, A. M. Stadler, N. Kyritsakas-Gruber, A. Madalan, K. Rissanen, L. Russo, G. Vaughan, J. M. Lehn, *European Journal of Inorganic Chemistry* **2007**, 2944.

[25] A. M. Stadler, N. Kyritsakas, R. Graff, J. M. Lehn, *Chemistry-a European Journal* **2006**, *12*, 4503.

[26] D. M. Cyr, B. Venkataraman, G. W. Flynn, A. Black, G. Whitesides, *J. Phys. Chem.* **1996**, *100*, 13747.

[27] J. Ramirez, A. M. Stadler, N. Kyritsakas, J. M. Lehn, *Chemical Communications* **2007**, 237.

[28] M. T. Raisanen, F. Mogele, S. Feodorow, B. Rieger, U. Ziener, M. Leskela, T. Repo, *European Journal of Inorganic Chemistry* **2007**, 4028.

[29] B. A. Hermann, L. J. Scherer, C. E. Housecroft, E. C. Constable, *Advanced Functional Materials* **2006**, *16*, 221.

[30] P. R. Andres, R. Lunkwitz, G. R. Pabst, K. Bohn, D. Wouters, S. Schmatloch, U. S. Schubert, *European Journal of Organic Chemistry* **2003**, 3769.

[31] A. Mourran, U. Ziener, M. Moller, M. Suarez, J. M. Lehn, *Langmuir* **2006**, *22*, 7579.

[32] A. Mourran, U. Ziener, M. Moller, E. Breuning, M. Ohkita, J. M. Lehn, *European Journal of Inorganic Chemistry* **2005**, 2641.

[33] U. Ziener, J. M. Lehn, A. Mourran, M. Moller, *Chemistry-a European Journal* **2002**, *8*, 951.

Conclusions and perspectives

This thesis has been focused on the design of new functional molecules for potential application in electronic devices based on Self-Assembled Monolayers on gold surfaces.

These molecular systems have been processed from solution on surfaces bearing in mind their ultimate use as switches or motors operating at solid substrate. To this purpose, three model systems have been selected and thoroughly studied.

The first system consists of a fully conjugated azobenzene derivative functionalized with a thiol group which determines its covalent binding on gold substrates. We showed that the isomerization of a densely packed monolayer is possible if a cooperative process is achieved at the solid substrate. In particular, the rigidity of our system and the aromatic interchain interactions favoured the isomerization process by limiting the possible conformational relaxation that would bring to a disordered isomerised Self-Assembled Monolayer (SAM). This finding is important as it demonstrate that isomerization does not occur only in weakly dense monolayers, where the reduced sterical hindrance is supposed to favour the process. Therefore, improvement towards the design of molecular switching that can undergo cooperative operations can represent a new possible route for achieving high yield of switching at solid substrate thus, possibly increasing the density of data storage.

In the second part of this work, by using the supramolecular approach, we propose an alternative strategy for the achievement of spatially confined functional molecules. As a proof of concept, we studied a model system where the balance between intramolecular hydrogen bonds and intra- and inter-molecular van der Waals interactions lead to the formation of linear ordered arrays of hydrogen bonded molecules. However, these ordered striped arrays strongly depend from kinetic factors. Therefore, further efforts should be devoted to the design of multi-components SAMs where the hetero-molecular interactions are thermodynamically more favored that the homo-molecular interactions. We infer that the stabilization of hetero-molecular interactions between the different SAM's components,

might lead to the formation of 2D multi-component crystals. We propose such multi-component crystals as ideal systems for isolating switching molecules at surfaces. Such an approach would offer a better addressability of the individual switching molecules bound at solid substrate. This represents an interesting alternative to the guest/host SAMs system presently used to isolate functional molecules at defect sites of a hosting monolayer.

Studies on the self-assemblies properties of molecular grid-like architectures on HOPG substrate have been also showed. Still, the affinity for the HOPG substrate of those studied grids is very poor, therefore a further improvement in their design is required. As an alternative to the addition of functional groups to improve the molecule-substrate affinity, we also propose the addition of specific peripheral moieties that would promote the lateral assembly in a 2D molecular crystal, by strong intermolecular interactions between adjacent ad-molecules.

Overall, the arrangement of functional molecular units into defined molecular architectures at solid substrate is one of the major goals into supramolecular chemistry and material science. The ability to control and manipulate such arrangements would provide new insight in the understanding of the required fundamental properties of ideal molecular systems for data storage devices.

List of publications

"STM investigation of alkylated thio-triphenylene monolayers at the solid-liquid interface: structure and dynamics"
M. Palma, G. Pace, O. Roussel, Y. Geerts, P. Samorì, *Austr. J. Chem.* **2006**, *59*, 376-380.

"Cooperative Light Induced Molecular Movements of Highly Ordered Azobenzene SAMs"
G. Pace, V. Ferri, C. Grave, M. Elbing, M. Zharnikov, M. Mayor, M.A. Rampi, P. Samorì, *Proc. Natl. Acad. Sci. USA.*, **2007**, *104*, 9937-9942.

"Light-powered Electrical Switch Based on Cargo Lifter Azobenzene SAMs"
Violetta Ferri, Mark Elbing, Giuseppina Pace, Michael D. Dickey, Michael Zharnikov, Paolo Samorì, Marcel Mayor, Maria Anita Rampi, *subtmitted.*

"Single Component Self-Assembled Monolayers of Aromatic Azo-biphenyl: Structure and Light Induced Molecular Movements"
Mark Elbing, Alfred Blaszczyk, Violetta Ferri, Christian Grave, Giuseppina Pace, Andrei Shaporenko, Carsten von Hänsich, Marcel Mayor, Paolo Samorì, Maria Anita Rampi, Michael Zharnikov, *submitted*.

"Sub-nanometer resolved patterning of bi-component Self-Assembled Monolayerson Au(111): mastering the supramolecular approach"
Giuseppina Pace, Anne Petitjean, Marie-Noëlle Lalloz-Vogel, Jack Harrowfield, Jean Marie Lehn, Paolo Samorì, *in press on Angewandte Chemie*, **2008**.